AIX-MARSEILLE UNIVERSITÉ
UNIVERSITÁ DEGLI STUDI DI GENOVA
ETABLISSEMENT EN COTUTELLE

SCUOLA DI SCIENZE MATEMATICHE, FISICHE E NATURALI - PHYSIQUE ET SCIENCES DE LA MATIÈRE

Thesis presented to obtain the degree of
DOTTORE DI RICERCA and DOCTEUR

Alba DOMI

SHOWER RECONSTRUCTION AND STERILE NEUTRINO ANALYSIS WITH KM3NeT/ORCA AND ANTARES

Defense on 16/12/2019 in front of the jury :

Francesco VISSANI	Gran Sasso Science Institute	Rapporteur
Christine MARQUET	Centre d'Etudes Nucleéaires de Bordeaux	Rapporteur
Heide COSTANTINI	CPPM, Marseille	Examinateur
Fabrizio TAVECCHIO	Osservatorio Astronomico di Brera	Examinateur
Marco PALLAVICINI	Dipartimento di Fisica, Genova	Examinateur
Paschal COYLE	CPPM, Marseille	Directeur de thèse
Marco ANGHINOLFI	INFN, Genova	Co-Directeur de thèse
Mauro TAIUTI	Dipartimento di Fisica, Genova	Co-Directeur de thèse

Numéro national de thèse/suffixe local : 2019AIXM0001/001ED62

Contents

Introduction

Neutrino physics is quite a new field of particle physics, since the idea of a neutrino was firstly introduced by W. Pauli in 1930 to try to explain how beta decays could conserve energy, momentum and spin. Since then, a big effort has been done by theoretical and experimental physicists to better understand the neutrino nature and its implications, not only in the more fundamental physics of the Standard Model (SM), but also in astrophysics and cosmology. This led, in the recent past, to two Nobel Prizes which were given to Neutrino Physics. In 2002 Ray Davis and Matoshi Koshiba got the Nobel Prize in Physics "for pioneering contributions to astrophysics, in particular for the detection of cosmic neutrinos" while in 2015 Arthur McDonald and Takaaki Kajita got the Nobel Prize "for the discovery of neutrino oscillations, which shows that neutrinos have mass".
While the standard three-flavor framework of neutrino oscillations is by now well established, there are a number of oscillation experiments whose results cannot be explained in this framework and need to invoke more exotic explanations. One attempt to solve this tension is to assume the existence of a light sterile neutrino with mass around 1 eV^2.
The data collected to date present an incomplete, perhaps even contradictory picture, where 2-3 σ agreement in favor of and in contradiction to the existence of sterile neutrinos is present. The need thus arises to provide a more precise and complete test of the sterile neutrino hypothesis, which will unambiguously confirm or refute the interpretation of past experimental results.
The work of my thesis is focused on the search of sterile neutrinos with deep water neutrino telescopes, using both the real data from ANTARES and the expected performances of the larger KM3NeT/ORCA detector. The aim of the thesis was not only to make such analysis but also to better understand the operation of a neutrino telescope. In particular, for KM3NeT/ORCA, I developed a shower reconstruction algorithm to fully exploit the capability of this detector. In addition, I also developed an online analysis tool to monitor the data coming from KM3NeT (ORCA and ARCA) which is already

running with the first detection units.
The thesis is thought to describe my work in a causal way, in the sense that it starts by introducing the problem I have been focusing on (i.e. the observed neutrino oscillation anomalies), then, starting from the flux used in the analysis (i.e. the atmospheric neutrino flux) we will follow the neutrinos journey up to the telecopes, where we will review how neutrinos are detected (i.e. Cherenkov emission of photons) and the related problems of this kind of detection. Once the Cherenkov photons produced by the original neutrinos have hit PMTs, I will describe in more detail the KM3NeT data acquisition system, **here I will have the opportunity to describe my work on online data**. Once the triggered data are saved to disk, reconstruction algorithms are applied to them, hence **here I will describe the shower reconstruction algorithm I developed for KM3NeT/ORCA**. Once reconstructions are applied to the data, we can know the detector response and use it in out analyses. In particular we can perform the sterile neutrino analysis with both ORCA and ANTARES, and this is what I will finally describe. To be more precise: Chapter 1 is a general introduction on sterile neutrinos anomalies which aims to give a global view on this argument. Chapter 2 explains in more detail neutrinos oscillations from a more theoretical point of view and puts the basis on neutrino properties useful for the final sterile neutrino analysis. Chapter 3 introduces the detection method of deep water neutrino telescopes in a more general way. Chapter 4 enters in the details of the KM3NeT data acquisition system with a particular importance on the online monitoring tool I wrote. Chapter 5 describes the shower reconstruction algorithm that I developed during the PhD. And finally, Chapter 6 shows the results of the sterile neutrino analysis with KM3NeT/ORCA and ANTARES.

Chapter 1

Standard and Sterile Neutrinos

This chapter aims to give a general overview on sterile neutrinos by citing the proofs in favour of and against the possible existence of light sterile neutrinos.

1.1 Number of Neutrinos

It is well known from the Z boson width measure made at LEP [1] that there are only three light (with mass $\leq M_Z/2$) active neutrino flavors, as shown in fig. 1.1. This implies that if additional neutrinos are considered, they should not couple with the Z boson. This is the reason why they are called sterile: they do not take part in the weak interactions.
From a theoretical point of view, there are no bounds on the number of sterile neutrinos that can be added in our models. However, from an experimental point of view, the total number of neutrinos (including also possible sterile states) leaves detectable imprints on cosmological observations that can hence be used to constrain neutrinos properties. On the other hand, different experiments on Earth can be performed, such as reactor experiments, short/long baseline neutrino experiments, Cherenkov detection of neutrinos coming from the Sun or from the atmosphere, with which sterile neutrinos properties can be constrained by looking at their oscillations.
In particular, cosmology is sensitive to the following neutrino properties [3]: their density, related to the number of neutrino species, and their masses. At first order, cosmology is also sensitive to the total neutrino mass, but it is blind to the mixing angles and CP violation phase which instead can be constrained with terrestrial experiments. This makes cosmological constraints complementary to measurements from terrestrial neutrino experiments and it is a great example of the interconnection between nuclear physics, particle physics, astrophysics and cosmology.

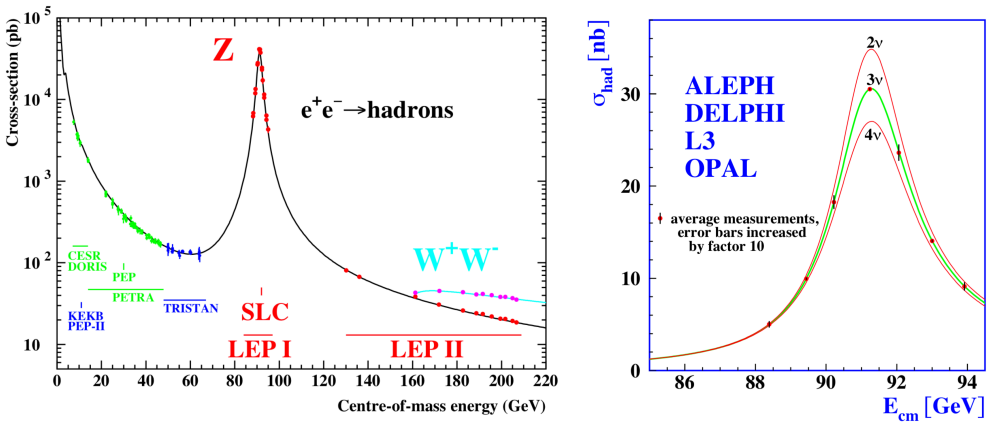

Figure 1.1: Z boson width measurement made at LEP [1]. The figure on the right shows the possible widths obtainable with a different number of neutrinos, and we can see that the case with 3 neutrinos perfectly fits the data.

1.1.1 Bounds from Cosmology

The contribution of all the relativistic species to the energy density of radiation ρ_R in the early Universe can be written in terms of the effective number of relativistic species N_{eff}, defined through [3]:

$$\rho_R = \rho_\gamma \left[1 + \frac{7}{8} \left(\frac{4}{11} \right)^{4/3} N_{eff} \right] \tag{1.1}$$

where ρ_γ is the energy density of photons, whose value today is known from measurements of the CMB temperature. This equation holds if neutrino decoupling is complete and as long as all neutrinos are relativistic [3]. The contribution of the three active neutrinos is $N_{eff} = 3.046$ [4] and it is larger than 3 because of the non-instantaneous decoupling of the neutrinos from the electron-photon fluid and of the entropy transfer at the electron decoupling [5].

It has been shown by accelerator data (Fig. 1.1) that the number of active neutrinos (i.e. coupling with the Z boson) is three. On the other side, there is mounting evidence from reactor and short-baseline neutrino oscillation experiments suggesting the existence of one or two sterile neutrinos [6] with mass splittings relative to the active flavours of about $\Delta m^2 \sim 1$ eV^2 and fairly large mixing parameters (see next section for a review and global in-

terpretation).
In the early Universe, active neutrinos are coupled by weak interactions. As the Universe expands, particle densities go down and temperatures fall. Weak interactions become ineffective to keep neutrinos in good thermal contact with the e.m. plasma: at this point there is the **neutrino decoupling**, which happened at $T \sim 1$ MeV, or $t \sim 1$ sec after the Big Bang [3]. Taking into account the anomalies observed in reactors and short-baseline experiments and assuming the presence of sterile neutrinos, flavour oscillations would bring these sterile states into thermal equilibrium prior to neutrino decoupling at T $\sim$ 1 MeV, thereby increasing the relativistic energy density [6]:

$$\rho_R = \frac{\pi^2}{15} T_\gamma^4 \left[1 + \frac{7}{8} \left(\frac{4}{11} \right)^{4/3} (3.046 + \Delta N_{eff}) \right] \tag{1.2}$$

here T_γ is the cosmic microwave background (CMB) temperature and N_{eff} $\equiv(3.046 + \Delta N_{eff})$ is the effective number of relativistic neutrino degrees of freedom. The presence of a non-zero ΔN_{eff} due to sterile neutrinos would modify the cosmic expansion rate and affect the big-bang nucleosynthesis (BBN) of light elements, the CMB anisotropies, and the formation of large-scale structures (LSS). Additionally, these eV-mass sterile neutrinos would later play the role of a non-negligible hot-dark matter component [5].
Hence, in cosmology, the value of N_{eff} can be constrained by different observations. For example, at the BBN (Big Bang Nucleosynthesis) epoch, from the comparison of theoretical predictions and experimental data on the primordial abundances of light elements, which also depend on the baryon-to-photon ratio $\eta_b = n_b/n_\gamma$ (or baryon density). To be more precise, at the BBN epoch, before neutrino decoupling, neutrons and protons are in mutual thermal equilibrium through charged-current weak interactions [7]:

$$n + e^+ \leftrightarrow p + \bar{\nu}_e \tag{1.3}$$

$$p + e^- \leftrightarrow n + \nu_e \tag{1.4}$$

$$n \leftrightarrow p + e^- + \bar{\nu}_e \tag{1.5}$$

this equilibrium is maintained so long as the timescale for the weak interactions is short compared with the timescale of the cosmic expansion. And it explicitly depends on:

1. the number of electron neutrinos,
2. the weak interaction cross section $\langle\sigma\rangle$, which is proportional to
   - T^2 (temperature),

- the reciprocal of the neutron half-life for free decay, $1/\tau_{1/2}$, which measures the intrinsic strength of the interaction.

As T decreases, there comes a point at where the weak interaction rate falls rather suddenly below the expansion rate (neutrino decoupling) and the ratio n/p is frozen (apart from free decay and some residual weak interactions). At the neutron freeze-out, the ratio n/p is [7]:

$$\frac{n}{p} = e^{(-\frac{(m_n - m_p)c^2}{kT_d})} = 0.20 = 1:5 \tag{1.6}$$

The precise value of the decoupling temperature T_d depends on the two physical constants N_{eff} and $\tau_{1/2}$ in a way that a lager value of N_{eff} leads to higher T_d, hence, to higher n/p values which implies higher primordial abundance of ^{4}He, since essentially all of the available neutrons are incorporated into ^{4}He nuclei [7]. Hence, **by measuring the abundances of primordial ^{4}He, N_{eff} can be constrained**.
However, we should be aware, when interpreting the BBN allowed range for N_{eff}, that the main problem when deriving the primordial abundances from observations in astrophysical sources is the existence of systematics not accounted for, in particular for ^{4}He.
Independent bounds on the radiation content of the Universe at a later epoch can be extracted from the analysis of the power spectrum of CMB anisotropies.

Effect of N_{eff} on the Cosmic Microwave Background

The effective number of relativistic species N_{eff} controls the expansion rate H in the early Universe and the time of the matter-radiation equality. In principle, the model for which $N_{eff} = 3.046$ could be incorrect, or missing some physical ingredients. Hence neutrinos could have a different density. This could be explained with a different neutrino-to-photon temperature ratio, or from non-thermal distorsions, or with a very large neutrino-antineutrino asymmetry in the early Universe and finally by assuming the presence of sterile neutrinos [3]. This influences the CMB spectrum in several ways. For example, as shown in Fig. 1.2, if N_{eff} is increased there is an increase of the first peak of the CMB, due to the fact that matter-radiation equality is delayed and the expansion rate H at CMB decoupling is higher, and a shift at higher multipoles of the angular scale of the acoustic peaks is present.
If neutrinos were massless, their impact would entirely be described by the value of N_{eff}. However, this is not true when neutrino masses are taken into account. In that case, N_{eff} refers to the radiation density at early times,

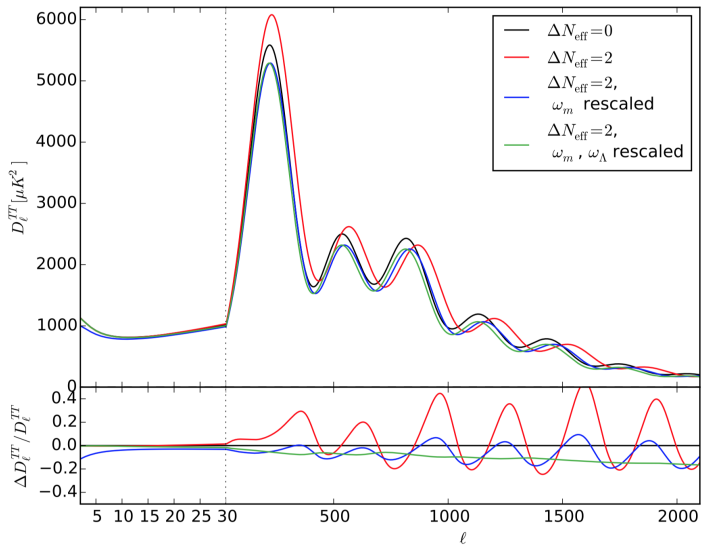

Figure 1.2: Effect of N_{eff} on the CMB temperature spectrum. Figure taken from [5].

before the non-relativistic transition of neutrinos. Nevertheless, as long as neutrino masses are not too large, it is useful to analyse cosmological models with free N_{eff} and M_ν set in first approximation to its minimal value (0.06 eV) [3], or with N_{eff} and M_ν both taken into account as free parameters, with an arbitrary mass splitting. This appears to be a fairly good approximation, even if performing an individual analysis for each model is the best way to proceed. This approximation is not valid anymore when individual neutrino masses can be large (of the order of one or several electron-volts), for example if we assume light massive sterile neutrinos (LSν) with an effective mass m_s^{eff} which can be produced through some thermal (TH) process or in some non-thermal scenario (DW).
Hence it is crucial to measure N_{eff} in order to check whether we correctly understand neutrino cosmology. However, if a value of N_{eff} larger than three was measured in CMB or LSS (Large Scale Structure) data, we still would not know if this comes from physics in the neutrino sector, or from other relativistic relics [3]. Therefore we need also other cosmological probes, such as the study of BBN, leptogenesis and baryogenesis, etc., or from laboratory experiments. For instance, a joint analysis of BBN with neutrino oscillation data has shown that in order to be compatible with measurements of primordial element abundances, the leptonic asymmetry cannot enhance the neutrino density above $N_{eff} \simeq 3.1$ [3]. Hence there is the need to have more and parallel observations to cosmologically constrain N_{eff}. For exam-

ple, for a minimal 7-parameter model (ΛCDM + N_{eff}), the CMB data alone give $N = 3.36^{+0.68}_{-0.64}$ (95%; Planck+WMAP+highL, where highL are higher-resolution experiments such as ACT, SPT that measure higher CMB multiple values [3]), well compatible with the standard prediction $N_{eff} = 3.046$. The previous discussion on the effect of N_{eff} on the CMB, shows that there is a correlation between measured values of N_{eff} and the Hubble constant H_0. However, H_0 can be measured in different ways, such as:

1. indirectly inferred by CMB, this method needs to assume a minimal model to constrain H_0,

2. direct measurements with cepheids and supernovae (HST), as known as "distance ladder", this method does not need to make any assumption on the cosmological model but it is affected from observational errors,

3. time delay between multiple images of a gravitational lensed quasars [8], this method is more recent and can give a 1% error on the measured value of H_0.

Apparently, method 2 and 3 are in agreement and they disagree with method 1 of about 4.4σ [9]. This is shown Fig. 1.3, where HST and the gravitational lensing method favour higher values of the expansion rate.
Hence, when Planck data is combined with HST data, one gets more than 2σ evidence for enhanced radiation $N = 3.62^{+0.50}_{-0.48}$, (95%; Planck+WP+highL + HST). Instead, with BAO (Baryon Acoustic Oscillations), the evidence disappears, $N = 3.30^{+0.54}_{-0.51}$ (95%; Planck+WP+highL+BAO) [3]. Since models with a free N_{eff} relax the tension between the different data sets, it makes sense to combine CMB data with BAO and HST at the same time, which gives $N = 3.52^{+0.48}_{-0.45}$ (95%; Planck+WP+highL+BAO+HST), slightly more than 2σ evidence for enhanced radiation.
Finally, several joint analyses of cosmological and SBL (Short BaseLine) neutrino oscillation data have been performed in the past. In particular, if constraints not only on N_{eff} but specifically on some light sterile neutrino (LSν) parameters from cosmology want to be derived, ΛCDM has to be extended with LSν. The constraints are obtained from the (Planck+WP+highL) datasets alone or adding the results of the analysis of SBL neutrino oscillations data as a prior for the LSν mass. Fig. 1.4 shows the constraints in the $m_s^{eff} - N_{eff}$ plane (being m_s^{eff} the effective sterile mass) obtained from the analysis of the CMB data mentioned above, both without short baseline prior (black) or with a SBL prior for the mass of a sterile neutrino in a DW scenario (red), i.e. non-thermally produced, or a TH (blue) scenario, i.e. a LSν thermally produced [5].

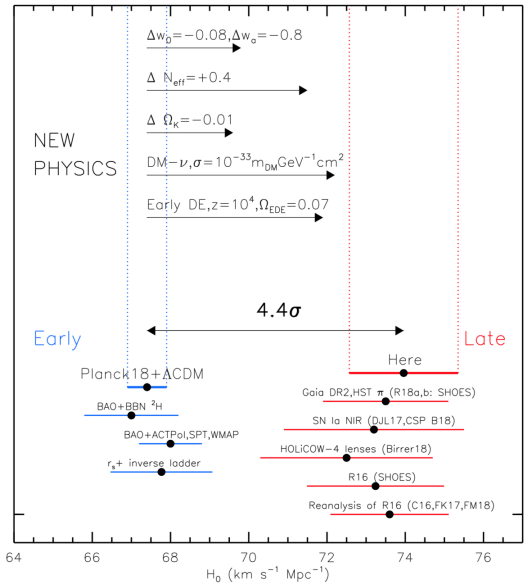

Figure 1.3: The 4.4σ difference between direct measurements of H_0 (in red) and the value predicted from Planck+ΛCDM. Direct measurements include the distance ladder method and the time delay of multiple images of gravitational lensed quasars (H0LiCOW in the figure). Figure taken from [9].

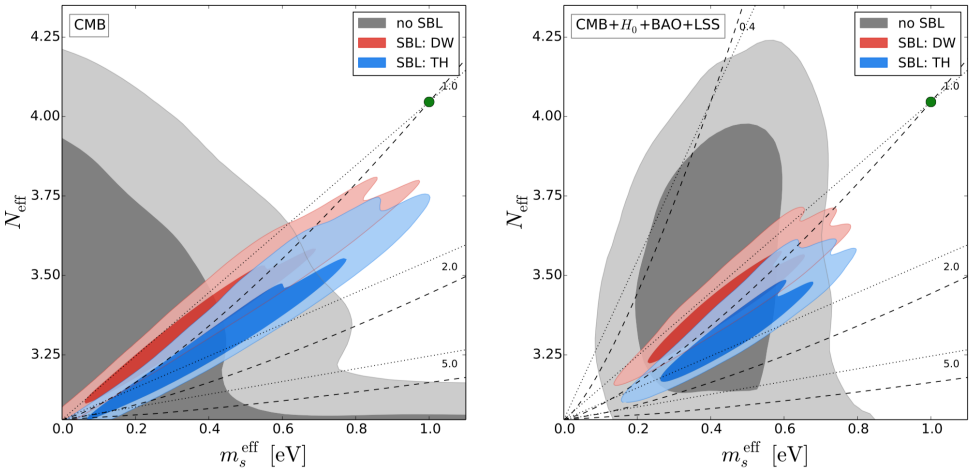

Figure 1.4: Constraints at 68% and 95% CL in the $m_s^{eff} - N_{eff}$ plane from the CMB data alone (left panel) and from a combination of CMB+H0+BAO+LSS data (right panel). The green point indicates a fully thermalized LSν with $m_s = 1$eV. Dotted (dashed) lines indicate constant masses, for values written in the figures, for the DW (TH) model. From [5].

1.1.2 Open Problems and Conclusion

The conclusion is that if HST+H0LiCOW data are robust, then one should consider seriously the possibility that N_{eff} exceeds the standard value, since this is one of the simplest ways to relax the conflict between the different data sets. However, this excess could also be caused by other effects, such as leptonic asymmetry, non-standard neutrino phase space distribution, or any type of relativistic relics. Therefore, even if N_{eff} were confirmed to exceed the standard value by future observations, **this does not mean that it is due to the presence of a light sterile neutrino**, **i.e. the value of N_{eff} is necessary but not sufficient to confirm the existence of light sterile neutrinos**.
If instead we assume that HST results are biased by systematics and should not be included, then the evidence for $N_{eff} > 3.046$ becomes very weak.
Despite the fact that the presence of a light sterile neutrino (LSν) can explain some of the tensions between the current cosmological observations at high- and low-redshift, it seems that a full reconciliation is rather complicated. The reason is that, if we assume a LSν with the mixing parameters determined by SBL oscillations, it should have been fully thermalized with the active neutrinos [5]; this means that we have 4 neutrino states fully thermalized, that give:

$$N_{eff} = 3.046 + 1 = 4.046 \tag{1.7}$$

which is in disagreement with all the possible values discussed above (even the more optimistic ones). Therefore, if we want to accommodate the SBL LSν with the other observations, we need to consider a not fully thermalized scenario. But to date we do not have a valid explanation to the fact that the LSν is not fully thermalized. Unless a new mechanism that explains the low thermalization of the LSν is found, **the current status of the global analyses shows that the SBL neutrino seems to be excluded by Cosmology**.
Moreover, the cosmological constraint can be evaded by suppressing active-sterile oscillations in the early Universe with non standard effects, such as non standard interactions (NSI) of neutrinos. Hence, as a conclusion, the cosmological information on sterile neutrinos is not as robust as the information obtained in laboratory experiments. The quest for the existence of sterile neutrinos must be then pursued with laboratory experiments and a positive result will require a modification of the cosmological model.
The next section presents a review of the terrestrial anomalies to give a parallel and complementary view regarding the presence of light sterile neutrinos.

1.2 Neutrino Oscillation Anomalies

Neutrino oscillation anomalies can be divided into three main categories:

- short baseline anomalies, i.e. observed in different SBL experiments,
- anomaly, observed once a Gallium radioactive source was used to test two solar neutrino detectors,
- reactor anomaly.

These three categories will be here reviewed.

1.2.1 Short-baseline neutrino oscillation anomalies

There are **three different indications of neutrino oscillations in short-baseline experiments**, referred as "anomalies", because up to now they can not be explained by standard assumptions. One way to explain these anomalies is to assume the existence of a sterile neutrino state with Δm^2 beyond the two in standard 3ν mixing.
The first evidence in favour of oscillations beyond the three-flavour framework came from the LSND experiment [10], which obtained $> 3\sigma$ evidence for $\bar{\nu}_\mu \to \bar{\nu}_e$ oscillations with $\Delta m^2 > 0.2$ eV^2.
The MiniBooNE experiment was designed to test LSND and it has reported oscillation results in both neutrino mode and antineutrino mode. Whereas the results obtained in neutrino mode disfavour most of the parameter space preferred by LSND, the MiniBooNE antineutrino data are consistent with the LSND signal. Moreover, MiniBooNE reports an excess of events at low energy, outside the energy range where LSND-like oscillations are expected.
On the other hand, there are a number of experiments that do not support this body of evidence for sterile neutrinos. The KARMEN experiment [12], which is very similar to LSND, observed no such evidence. However, a joint analysis of the two experiments [13] shows that their data sets are compatible with oscillations occurring either in a band from 0.2 to 1 eV^2 or in a region around 7 eV^2. Also, a number of ν_μ disappearance searches, including MINOS/MINOS+ [16] search for disappearance of active neutrinos in neutral current events, produced negative results.

LSND and MiniBooNE

The Liquid Scintillator Neutrino Detector (LSND) experiment [10] was performed at the Los Alamos Neutron Science Center (LANSCE) from 1993 to 1998, and it was designed to search for $\bar{\nu}_\mu \to \bar{\nu}_e$ oscillations.

A proton beam of about 1 mA and energy 798 MeV hitting a target produced a large number of pions. Since most of the π^- were absorbed by the nuclei of the target, and only a small fraction decayed into μ^-, which in turn were largely captured, the neutrinos were mainly produced by $\pi^+ \to \mu^+ + \nu_\mu$ and $\mu^+ \to e^+ + \nu_e + \bar{\nu}_\mu$ decays, most of which ($> 95\%$) decayed at rest (DAR) [27]. Hence, the resulting DAR neutrino fluxes are well understood since almost all detectable neutrinos arise from π^+ or μ^+. The production of kaons or heavier mesons is negligible at these proton energies [31].
The $\bar{\nu}_e$ flux produced in these two decays was estimated to be only $\sim 8 \times 10^{-4}$ times as large as the $\bar{\nu}_\mu$ flux in the $20 < E_\nu < 52.8$ MeV energy range, so that the observation of a $\bar{\nu}_e$ event rate significantly above the calculated background would be evidence for $\bar{\nu}_\mu \to \bar{\nu}_e$ oscillations. The LSND detector consisted of a tank of 167 tons of liquid scintillator placed at a distance of 30 m from the target, the signal was taken by photomultiplier tubes.
The $\bar{\nu}_e$ events have been detected through the inverse beta decay (IBD) process

$$\bar{\nu}_e + p \to n + e^+ \tag{1.8}$$

That allows a two-fold signature of a positron with a 52.8 MeV endpoint and a correlated 2.2 MeV γ from neutron capture on a free proton. Neglecting the small recoil energy of the neutron, the neutrino energy E is inferred from the measured electron kinetic energy $T_e = E_e - m_e$ [27] through the energy-conservation relation

$$E = T_e + m_e + m_n - m_p \simeq T_e + 1.8 MeV \tag{1.9}$$

where m_p and m_n are the proton and neutron masses.
The LSND data cover the energy range $20 \leq T_e \leq 60$ MeV. The energy resolution at the endpoint was $\sim 7\%$ and the angular resolution was $\sim 12°$.
The backgrounds to be taken into account are mainly two. The first background is from the decay of μ^- DAR in the beam stop into $\bar{\nu}_e$. The $\bar{\nu}_e$ scatter in the detector via $\bar{\nu}_e p \to e^+ n$ and produces positrons. This background is highly suppressed because once the π^- are produces, they decay in flight (DIF) into μ^- which decay at rest (DAR) before being captured [31]. The second background is from π^- DIF in the beam stop followed by $\bar{\nu}_\mu p \to \mu^+ n$ scattering in the detector. This background mimics the signal if the μ^+ has a sufficiently low energy [31].
The LSND analysis shows a significant excess of $\bar{\nu}_e$-like events over the background ($\sim 3.8\sigma$). One way to explain this excess is by assuming a new sterile neutrino state with $\Delta m^2_{SBL} \geq 0.1$ eV^2.
The MiniBooNE experiment [11] tested the LSND anomaly. MiniBooNE is operating since 2002 at Fermilab, where neutrinos are produced by hitting

the 8 GeV protons from the Fermilab booster into a beryllium target and producing a beam of pions. A focusing horn focalizes the pions with the needed sign towards the detector, placed at a distance of 541 m from the target. The detector consists of a tank filled with 818 tons of pure mineral oil (CH_2) viewed by 1520 phototubes [27].
MiniBooNE searches for $\nu_\mu \to \nu_e$ oscillations by measuring the rate of $\nu_e C \to e^- X$ (known as charged current quasi-elastic events or CCQE) and testing whether the measured rate is consistent with the estimated background rate [31].
Initially the MiniBooNE experiment operated in "neutrino mode" with a focused beam of π^+ that decayed in an almost pure beam or ν_μ's. Their first analysis [11] considered events with E $>$ 475 MeV, because this threshold reduced the backgrounds with little impact on the fit's sensitivity to oscillations. They did not abserve any excess over background, resulting in a 98% exclusion of the sterile neutrino hypothesis as the explanation of the LSND anomaly. However, they observed an excess of ν_e-like events below 475 MeV which was lately re-confirmed in both neutrino and antineutrino modes [27]; at the same time, the data above 475 MeV continued to show little or no excess.
Since most of the energy range below 475 MeV corresponds to different L/E values than the ones probed by LSND, the MiniBooNE low-energy excess ihas to be considered as a different effect than the LSND anomaly. For this reason it is known as the "MiniBooNE low-energy anomaly". One possible explanation for this anomaly is that the low-energy excess is due to photons, that cannot be distinguished from ν_e-like events in the MiniBooNE detector. In fact, photons are produced by the neutral current (NC) interactions of ν_μ, which produce π^0 that decay into two photons, of which only one is visible. This possibility is going to be investigated by the MicroBooNE experiment at Fermilab [17], with a large Liquid Argon Time Projection Chamber in which electrons and photons can be distinguished [27].
Finally, MiniBooNE performed also a search for ν_μ and $\bar{\nu}_\mu$ disappearance in 2009 [18]. So far, no evidence for ν_μ or $\bar{\nu}_\mu$ disappearance due to short-baseline oscillations has been found. Limits have been placed on simple two neutrino mixing in the Δm^2 region of interest for sterile neutrino models [31].

1.2.2 The Gallium neutrino anomaly

The Gallium neutrino anomaly, term coined in [19], consists in the disappearance of ν_e measured by putting a Gallium radioactive source in the GALLEX [20] and SAGE [21] experiments. The idea of putting the radioactive source came along to test the working of the GALLEX and SAGE solar neutrino

detectors. Artificial, and intense, ^{51}Cr and ^{37}Ar radioactive sources, producing ν_e's through the electron capture processes $e^- + ^{51}Cr \rightarrow ^{51}V + \nu_e$ and $e^- + ^{37}Ar \rightarrow ^{37}Cl + \nu_e$ have been placed near the center of each detector. The ν_e's have been detected with the same reaction that was used for the detection of solar electron neutrinos:

$$\nu_e + ^{71}Ga \rightarrow ^{71}Ge + e^- \tag{1.10}$$

which has the low neutrino energy threshold of 0.233 MeV. Figure 1.5 (a)

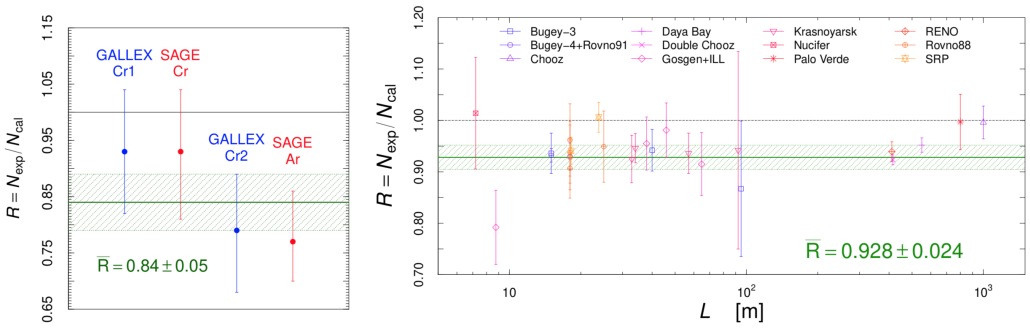

(a) (b)

Figure 1.5: The Gallium neutrino (a) and reactor antineutrino (b) anomalies. Taken from [27].

shows the ratios R of the number of experimentally measured (N_{exp}) and calculated (N_{cal}) electron neutrino events in the two ^{51}Cr GALLEX and ^{51}Cr and ^{37}Ar SAGE experiments. The average ratio shown in the figure is R = 0.84 ± 0.05 which, has been evaluated in [19] as a 2.9σ deficit, known as the Gallium anomaly [19]. This anomaly can be explained by neutrino oscillations generated by a $\Delta m^2_{SBL} \geq 1$ eV^2. However, the ratios have been calculated by using the best fit values of measured cross sections, that contain large uncertainties. Hence, at least part of the deficit of measured events with respect to the prediction could be explained by this fact, but this is not sufficient to get rid of the anomaly.

1.2.3 The Reactor Antineutrino Anomaly

The reactor antineutrino anomaly, discovered in 2011, was a consequence of the new calculation of Mueller et al [22] of $\bar{\nu}_e$ fluxes produced in a reactor by the decay of the fissionable nuclides ^{235}U, ^{238}U, ^{239}Pu, and ^{241}Pu [23]. The new calculation predicted fluxes about 5% larger than the previous calculation [27]. As a consequence, the new expected detection rates turned out

to be larger than what observed in different short-baseline reactor neutrino experiments, generating the "reactor antineutrino anomaly".
Figure 1.5 (b) shows the ratios R of the measured (N_{exp}) and calculated (N_{cal}) number of electron antineutrino events in different reactor experiments at the respective distance L from the reactor [27]. Due to the new larger calculated rates, the ratio R was found to be < 1, in particular $R = 0.928 \pm 0.024$, indicates a 3.0σ deficit that is known as the reactor antineutrino anomaly. Taking into account L/E in reactor neutrinos, the deficit can be explained by neutrino oscillations generated by a $\Delta m^2_{SBL} \geq 0.5$ eV^2.
The uncertainties of the Huber-Muller fluxes, have a big impact in the statistical significance of the anomaly. Moreover, the discovery of an excess in the spectrum of detected events around 5 MeV (often called the "5 MeV bump") in the RENO, Double Chooz and Daya Bay experiments has put in question the accuracy of the new fluxes [27]. In this sense, it is possible that the uncertainties of the Huber-Muller fluxes are larger than the nominal ones, but their values are unknown. Therefore, the strategy of the new reactor experiments, like NEOS [24] and DANSS [25], has been to compare the spectrum of $\bar{\nu}_e$-induced events measured at different distances searching for the differences due to oscillations.
The NEOS experiment consisted in a 1 ton detector made of Gd-loaded liquid scintillator located at a distance of 24 m from the 2.8GW$_{th}$ reactor of the Hanbit Nuclear Power Complex in Yeonggwang, Korea. The spectrum of $\bar{\nu}_e$-induced events was normalized to the prediction obtained from the Daya Bay spectrum so that the information on neutrino oscillations is independent from the theoretical flux calculation [27]. The NEOS collaboration found an anomaly explained by two almost equivalent best fits at ($\Delta m^2_{41} \geq 1.7$ eV^2, $\sin^2 2\theta_{ee} \simeq 0.05$) and ($\Delta m^2_{41} \geq 1.3$ eV^2,$\sin^2 2\theta_{ee} \simeq 0.04$).
In the DANSS experiment a highly segmented plastic scintillator detector of 1 m^3 is installed on a movable platform which allows to change its distance from the source, which is the reactor of the Kalinin Nuclear Power Plant in Russia. Also in this case an anomaly, compatible with $\sin^2 2\theta_{ee} \simeq 0.05$ and $\Delta m^2_{41} \geq 1.4$ eV^2 has been found.
The fact that the NEOS and DANSS best fit regions coincide at $\sin^2\theta_{ee} \simeq 0.04 - 0.05$ and $\Delta m^2_{41} \geq 1.3 - 1.4$ eV^2 is a strong indication in favour of active-sterile neutrino oscillations that confirms the older reactor antineutrino anomaly and, at the same time, it is more robust, since it is not based on the theoretical flux calculations [27]..
Finally, the latest information on the reactor $\bar{\nu}_e$ fluxes and oscillations come from the measurement of the event rate evolution by changing the reactor fuel composition during burnup in the Daya Bay and RENO experiments [27]. The event rate evolution alone disfavours the presence of a sterile neutrino

as explanation of the reactor antineutrino anomaly, but the combination of the Daya Bay and RENO evolution data with the absolute rates of the other experiments in Fig. 1.6 (b) leave open the possibilities for sterile neutrinos, or a flux miscalculation, or a combination of both.

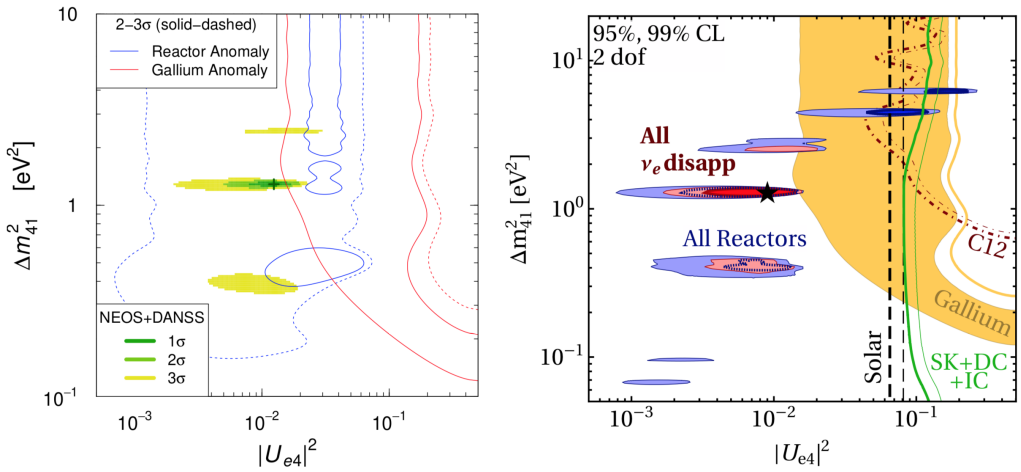

Figure 1.6: Results of SBL experiments. From [27]

1.3 Global Fits

The term "global fits" in only indicative, because there is no established consensus on the exact set of data to be used to combine the different experiments results. As a consequence, global analyses made by different groups present some variations. Moreover, the method of data analysis of old experiments (as LSND and old reactor experiments) is not perfectly clear, because the only available information is that in the published articles, which is not complete [27]. With this in mind, the results of the global fits cannot be considered as very accurate, but have to be taken as indicative of the true solution.

1.3.1 ν_e and $\bar{\nu}_e$ disappearance

The interesting results on SBL $\bar{\nu}_e$ disappearance are reproduced in Fig. 1.6. The shadowed regions in Fig. 1.6 (a) have been obtained from the combined fit of the NEOS/Daya Bay and DANSS spectral ratio data (NEOS+DANSS) [27]. Apparently, the data can better constrain the active-sterile mixing

parameters in the region around $\Delta m^2_{41} \geq 1.3$ eV^2 and $|U_{34}|^2 \simeq 0.01$ and this constitutes a model-independent indication in favor of SBL $\bar{\nu}_e$ disappearance due to active-sterile oscillations that is much more robust than those of the original reactor and Gallium anomalies, which suffer from the dependence on the calculated reactor fluxes and the assumed Gallium detector efficiencies [27]. Fig. 1.6 (a) shows that there is a tension between the model-independent NEOS+DANSS allowed regions and those indicated by the reactor and Gallium anomalies. This is a strong indication in favour of a partial impact of wrong flux predictions, which have to be corrected. Finally, it is also possible that the GALLEX and SAGE detector efficiencies may have been overestimated.
The blue shadowed regions in Fig. 1.6 (b) have been obtained from a global fit of the reactor neutrino data including NEOS/Daya Bay and DANSS. The red shadowed regions include the Gallium, solar, and ν_e ^{12}C constraints, that are also shown separately. The figure shows also the atmospheric neutrino constraint obtained from the Super-Kamiokande (SK), Deep Core (DC) and IceCube (IC) data, that is comparable to the solar neutrino constraint [27]. **The overall conclusion obtained from SBL $\bar{\nu}_e$ disappearance data is that there is a strong indication in favour of oscillations into sterile neutrinos at the 3σ level, which is independent of the theoretical reactor flux calculations.** This represents an important improvement with respect to the original reactor antineutrino anomaly that was based on the theoretical flux calculations. However, the model-independent indication depends on the NEOS/Daya Bay and DANSS spectral ratios that has to be confirmed by new experiments.

1.3.2 $\nu_\mu \to \nu_e$ and $\bar{\nu}_\mu \to \bar{\nu}_e$ appearance

Fig. 1.7 shows the results from the relevant SBL $\overset{(-)}{\nu}_\mu \to \overset{(-)}{\nu}_e$ appearance experiments. Of all the experiments only LSND and MiniBooNE found indications in favour of sterile neutrino mixing. The other experiments deny this hypothesis and provide exclusion curves that constitute upper limits on $\sin^2 2\theta_{e\mu}$ and Δm^2_{41}. The difference between Figs. 1.7 (a) and (b) is that in Fig. 1.7 (a) all the MiniBooNE data are used, whereas Fig. 1.7 (b) the low-energy MiniBooNE data are omitted. As already mentioned, most of the MiniBooNE low-energy excess lies out of the L/E range of LSND and it is probably not due to oscillations. The comparison of Figs. 1.7 (a) and 1.7 (b) shows that without the low-energy data the 3σ MiniBooNE constraint changes from a closed contour to an exclusion curve. As a consequence there is a larger combined allowed region without the low-energy MiniBooNE data (Fig. 1.7 b)

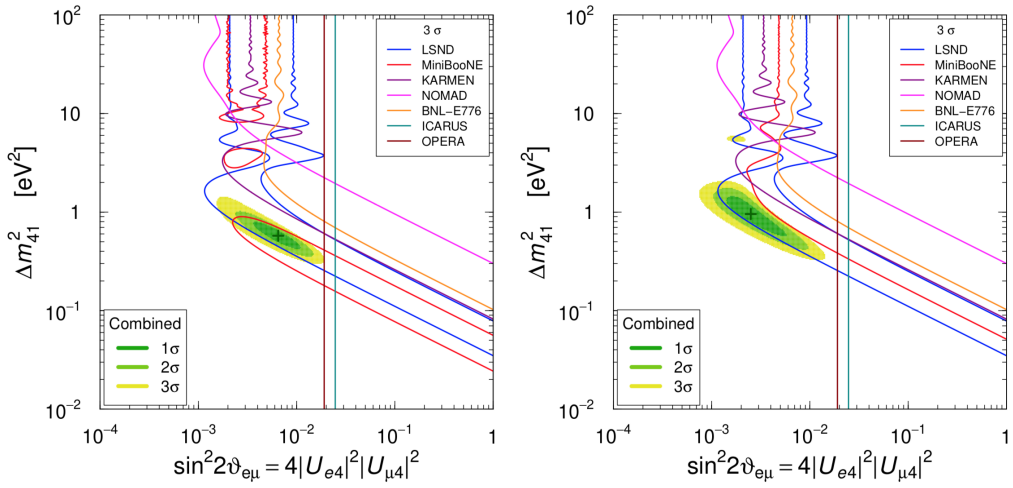

Figure 1.7: Global fit of SBL $\nu_\nu \to \nu_e$ and $\bar{\nu}_\mu \to \bar{\nu}_e$ appearance with (a) MiniBoone data and without it (b). From [27].

than that with low-energy MiniBooNE data (Fig. 1.7 a) and smaller values of $\sin^2 2\theta_{e\mu}$ are allowed ans since the disappearance data constrain severely $\sin^2 2\theta_{e\mu}$, this fact is quite important in the global fit appearance and disappearance data.

1.3.3 ν_μ and $\bar{\nu}_\mu$ disappearance

If we assume that SBL anomalies are due to active-sterile oscillations, then they must show up also in $\bar{\nu}_\mu$ disappearance. In this case it is worth to cite the contribution of the Ice Cube analyses [14], [15] because they show that also neutrino telescopes can give an important contribution in this topic. Actually, in both the analyses, **no evidence for a mixing into a sterile neutrino has been observed** and the upper limits they put are some of the best to date. In this sense, the analysis performed by MINOS/MINOS+ [16], **confirming the non mixing into a sterile state**, represents the most stringent constraint available to date in the active-sterile parameter space.
Figure 1.8 (a) shows a summary of the exclusion curves found in different $\bar{\nu}_\mu$ disappearance experiments. One can see that the recent MINOS/MINOS+ [16] limits are the strongest for $\Delta m^2_{41} \sim 1$ eV^2 and determine the overall combined limit on $|U_{\mu 4}|^2$ in that region.
This very strong bound causes the **strong appearance-disappearance tension**.

In particular, in Ref. [28] it is shown that, with the assumption of a sterile neutrino, the consistency between ν_e appearance data, mainly driven by LSND (MiniBooNE plays a subleading role), and the bounds on ν_μ disappearance, mostly driven by MINOS+ and IceCube [15], has a p-value less than 2.6×10^{-6}, which brings to the conclusion that an explanation of the LSND anomaly in terms of sterile neutrino oscillations in the 3+1 scenario is excluded at the 4.7σ level [28]. As stated in [28], this estimation is robust with respect to variations in the analysis and used data, and, in particular, it does not depend neither on the theoretically predicted reactor neutrino fluxes, nor on constraints from any single experiment. In fact, even if all reactor data are removed in the evaluation, the p-value remains at 3.8×10^{-5}. As a conclusion, the appearance-disappearance tension, and in particular the analysis in [28], rules out the sterile neutrino hypothesis as an explanation of the LSND and MiniBooNE anomalies, but it remains a viable option for the reactor and gallium anomalies.

1.3.4 Appearance and Disappearance

Figure 1.8 (b) shows the combined results of appearance and disappearance data. The appearance data are those corresponding to Fig. 1.7 (b), without the controversial low-energy MiniBooNE data. Even with this choice, it is evident that there is a strong tension between the region within the blue contours allowed at 3σ by the appearance data and the combined bound of $\bar{\nu}_e$ and $\bar{\nu}_\mu$ disappearance data that exclude at 3σ all the region outside the two red semicontours. Although the standard goodness-of-fit is fine (54%), the appearance-disappearance parameter goodness-of-fit is as low as 0.015%, disfavoring the global 3+1 fit at 3.8σ. Considering a global fit with the low-energy MiniBooNE data, there is still a favorable standard goodness-of-fit of 21%, but the appearance-disappearance parameter goodness-of-fit drops to 2×10^{-7}, which disfavors the global 3+1 fit at 5.2σ [27].

1.3.5 Conclusion

In has been shown, in the cosmology section, that accommodating SBL data with the different cosmological observation is quite hard. Cosmology itself could be able, in the future, to constrain the number of effective neutrinos in a more precise way, which will automatically constrain the sterile neutrino hypothesis. However, if cosmology will confirm an higher value of N_{eff}, this does not mean that it is due to the presence of a sterile neutrino. Hence, terrestrial experiments are still crucial in the sterile neutrino search. In this respect, the current status of the global fit of appearance and disappearance

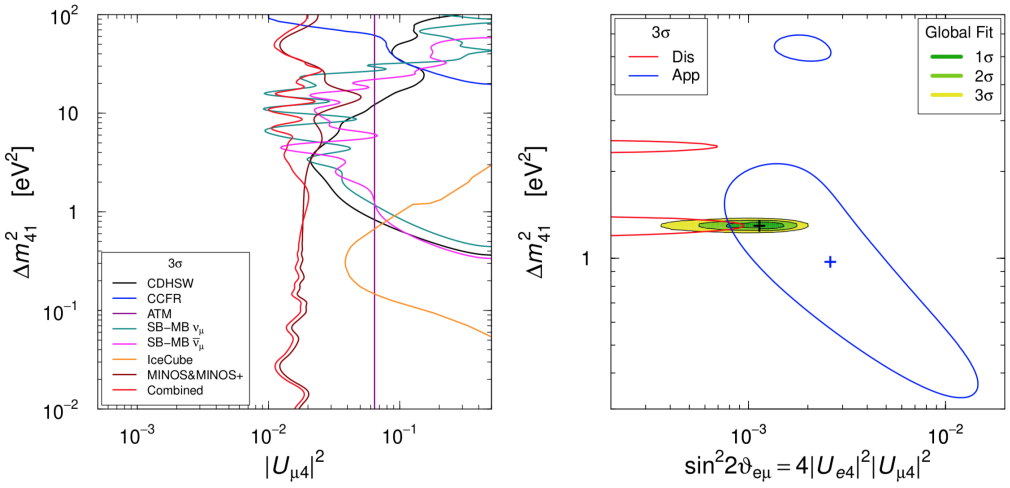

(a) (b)

Figure 1.8: Global fit of SBL ν_μ and $\bar{\nu}_\mu$ disappearance (a) and global fit with appearance + disappearance (b). From [27].

data indicates that the interpretation of the results of some experiment or group of experiments in terms of neutrino oscillations into a sterile state is not correct. Hence there is the need to solve this tension and this will be done by future experiments. In particular, my thesis is focused on the contribution that ANTARES and the future KM3NeT/ORCA can give.

Chapter 2

Theory of Sterile Neutrinos

This chapter aims to give a basic overview of the neutrino physics, focusing on the important points useful to understand sterile neutrinos, i.e. neutrino masses and neutrino oscillations. In particular, since the analysis of this thesis uses atmospheric neutrinos passing through the Earth, neutrino oscillations in matter will also be discussed here. Finally, the key points to understand the analysis of this thesis will be presented: i.e. the impact of additional phases in the sterile analysis and the impact of a low mass sterile neutrino.

2.1 Neutrino Masses

Neutrino mass is by far the most important subject of study in neutrino physics.
In the 60's, when the Standard Model (SM) was proposed ([32],[33],[34]), neutrinos were believed to be massless. Experiments searching for the electron neutrino mass obtained in fact upper limits of about 200 eV, which is smaller than the mass of the electron (0.5 MeV), the lightest known elementary fermion.
Therefore, the Standard Model was formulated without including neutrinos mass terms. To be more precise, a Dirac mass term in the SM Lagrangian requires the existence of right-handed components $\nu_{\beta R}$, such as it can be defined as $\overline{\nu_{\alpha R}}\nu_{\beta L}$. However, in the SM the neutrino fields have only the left-handed component $\nu_{\alpha L}$. For this reason neutrinos are massless [27].
However, when neutrino oscillations were discovered in 1998 in the Super-Kamiokande atmospheric neutrino experiment [30], it became clear that the Standard Model must be extended in order to generate neutrino masses. After that, other experiments with solar, atmospheric, reactor and accelerator

neutrinos have provided compelling evidences for oscillations of neutrinos caused by nonzero neutrino masses and neutrino mixing.
A Dirac neutrino mass can be generated with the same Higgs mechanism that gives masses to quarks and charged leptons in the Standard Model (SM). The only extension of the SM that is needed is the introduction of right-handed components $\nu_{\alpha R}$ of the neutrino fields ($\alpha = e, \mu, \tau$). Such a model is sometimes called the **minimally extended Standard Model**, in which the asymmetry in the SM between the lepton and quark sectors due to the absence of right-handed neutrino fields is eliminated [29].
Neutrinos could also have Majorana mass terms ${\nu^T}_{\alpha L} C^\dagger \nu_{\beta L}$, which involve only the left-handed fields $\nu_{\alpha L}$, but this possibility is forbidden by the SU(2)L $\times$ U(1)Y symmetries of the SM, i.e. by color and electromagnetic gauge invariance for quarks and charged leptons, but are possible for both active (after electroweak symmetry breaking) and sterile neutrinos if there is no conserved lepton number.
These right-handed components are also called "neutral lepton singlets" or "sterile neutrinos", because they do not take part to the Standard Model weak interactions. Moreover, there is no known constraint on the number of right-handed neutrino fields and, instead of considering three right-handed fields $\nu_{\alpha R}$ with $\alpha = e, \mu, \tau$, a general theory must considerN_s right-handed fields ν_{sR} with s = 1,..., N_s. These right-handed neutrino fields can have Majorana mass terms ${\nu^T}_{sR} C^\dagger \nu_{s'R}$ that are invariant under SU(2)L $\times$ U(1)Y gauge transformations and the corresponding masses cannot be generated by the SM Higgs mechanism [31]. Therefore, in general the introduction right-handed neutrino fields implies that:

1. There is some physics beyond the Standard Model.

2. Massive neutrinos are Majorana particles.

There is a mechanism called "**seesaw**" that produces naturally small light neutrino masses given by the relation $m_{light} \sim {m^2}_D / m_R$ where m_D is the scale of the Dirac neutrino masses generated with the standard Higgs mechanism, and m_R is the scale of the masses of very heavy right-handed neutrinos. Since m_D is smaller than the electroweak scale (about 200 GeV), if m_R is very large, say $\sim 10^{14-15}$ GeV as predicted by Grand Unified Theories, the light neutrino masses are naturally smaller than about an eV. In this scenario the right-handed neutrinos are sterile, but decoupled from the accessible low-energy physics.
Our ability to observe the mostly sterile states is proportional to [31]:

$$\Theta^2 \sim \frac{m_{1,2,3}}{m_{4,5,\ldots}} \sim \frac{m_D^2}{m_R^2} \tag{2.1}$$

Given $m_{1,2,3} \leq 10^{-1}$ the mostly sterile states are very weakly coupled unless $\Theta^2 \geq 10^{-2}$, hence $m_{4,5,...} \leq 10$ eV. This generic behaviour of the active–sterile mixing angles is also depicted in Fig. 2.1

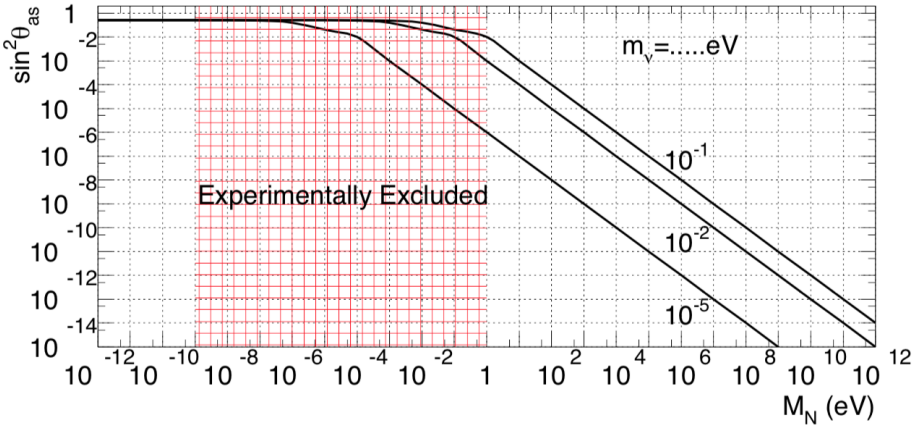

Figure 2.1: Estimate of the magnitude of the mixing between active and sterile neutrinos $sin^2\theta_{as}$ as a function of the right-handed neutrino mass M_R, for different values of the mostly active neutrino masses, $m_\nu = 10^{-1}, 10^{-2}, 10^{-5}$ eV. The hatched region qualitatively indicates the values of M_R that are excluded by the world's particle physics data. From [31].

Fig. 2.1 also shows that the mixing between the light neutrinos and the heavy right-handed neutrinos is strongly suppressed. Therefore, although these sterile neutrinos are very important for the theory, they do not have a phenomenological impact. **However, if there are several right-handed neutrino fields, not all of them have to be very heavy**. Some of them could be light and belong to low-energy new physics beyond the Standard Model. These neutrinos can have masses at all the currently accessible energy scales, from some TeV down to the sub-eV mass scale [27]. Since these neutrinos belong to physics beyond the SM, they do not have standard weak interactions (as well as strong and electromagnetic interactions, as all neutrino fields); their only interaction is gravitational, this is why they are called **sterile**. In principle, they could also have non-standard interactions which are beyond of SM the physics. However, these interactions must have tiny effects on the behaviour of the Standard Model particles, since otherwise they would have been detected. Therefore, the phenomenology of neutrino interactions can be considered as solely due to weak interactions.
In this respect, in most experiments neutrinos are detected through charged-

current (CC) weak interactions which are generated by the Lagrangian

$$\mathcal{L}_{CC} = -\frac{g}{\sqrt{2}} \sum_{\alpha=e,\mu,\tau} \left(\overline{\ell_{\alpha L}} \gamma^{\rho} \nu_{\alpha L} W_{\rho}^{\dagger} + \overline{\nu_{\alpha L}} \gamma^{\rho} \ell_{\alpha L} W_{\rho} \right) \tag{2.2}$$

where W^{ρ} is the field of the W vector boson and g is a coupling constant. These interactions allow us to distinguish the neutrino flavour by detecting the corresponding charged lepton. However, if neutrino masses are considered, the neutrino mixing matrix V has to be introduced, since it relates the neutrinos with given mass, ν_i, to those with given flavour,

$$\nu_l = V_{li} \nu_i \tag{2.3}$$

This way, taking into account the mixing:

$$\mathcal{L}_{CC} = -\frac{g}{\sqrt{2}} \sum_{\alpha=e,\mu,\tau} \sum_{k=1}^{N} \left(\overline{\ell_{\alpha L}} \gamma^{\rho} V_{\alpha k} \nu_{kL} W_{\rho}^{\dagger} + \overline{\nu_{kL}} \star V_{\alpha k} \gamma^{\rho} \ell_{\alpha L} W_{\rho} \right) \tag{2.4}$$

where there are **no upper limits on the value of N, i.e. on the number of massive neutrinos**. Here one can see that although there are only three flavors all the N massive neutrinos (the $\sum_{k=1}^{N}$) take part to charged-current weak interactions (if their masses are kinematically allowed).
Although it is possible to work without a parameterization of the mixing matrix, it is common and often useful to parameterize it in terms of mixing angles and phases. In general, a unitary N×N matrix depends on N^2 independent real parameters. These parameters can be divided into [29]:

$$\frac{N(N-1)}{2} \quad \text{mixing angles,} \tag{2.5}$$

$$\frac{N(N+1)}{2} \quad \text{phases.} \tag{2.6}$$

Hence, the neutrino mixing matrix with N = 3 can be written in terms of three mixing angles and six phases. However, not all the phases are physical observables, actually [29]:

$$2N - 1 = 5 \tag{2.7}$$

phases of the mixing matrix can be eliminated, thus, the quark mixing matrix contains:

$$\frac{N(N+1)}{2} - (2N-1) = 1 \quad \text{physical phase.} \tag{2.8}$$

It is customary to express conveniently the mixing matrix only in terms of these four physical parameters, three mixing angles and one phase, which are measurable quantities. In components:

$$\begin{pmatrix} V_{e1} & V_{e2} & V_{e3} \\ V_{\mu 1} & V_{\mu 2} & V_{e\mu 3} \\ V_{\tau 1} & V_{\tau 2} & V_{\tau 3} \end{pmatrix} = \begin{pmatrix} c_{12}c_{13} & c_{13}s_{12} & s_{13} \\ -c_{23}s_{12}e^{i\phi} - c_{12}s_{13}s_{23} & c_{12}c_{23}e^{i\phi} - s_{12}s_{13}s_{23} & c_{13}s_{23} \\ s_{23}s_{12}e^{i\phi} - c_{12}c_{23}s_{13} & -c_{12}s_{23}e^{i\phi} - c_{23}s_{12}s_{13} & c_{13}c_{23} \end{pmatrix} \tag{2.9}$$

where $c_{ij} = \cos\theta_{ij}$ and $s_{ij} = \sin\theta_{ij}$. The parameterization presented in eq. 2.9 is the standard one, other commonly employed parameterizations have the complex phase in different positions or different names for the mixing angles. This way the mixing matrix can be written as a sequence of Euler rotations

$$V = R_{23}(\theta_{23}) \cdot R_{13}(\theta_{13}) \cdot \mathrm{diag}(1, e^{i\phi}, 1) \cdot R_{12}(\theta_{12}) \tag{2.10}$$

where $R_{ij}(\theta_{ij})$ represents a rotation by θ_{ij} in the ij plane and $i, j = 1, 2, 3$. The elements of the mixing matrix are used to define the neutrino oscillation probabilities.

2.2 Standard Neutrino Oscillation

Oscillations of neutrinos are a consequence of the presence of non zero neutrino masses. In the standard theory of neutrino oscillations [36] a neutrino with flavor α and momentum $\vec{p}$ is described by the flavor state:

$$|\nu_\alpha\rangle = \sum_k V^*_{\alpha k} |\nu_k\rangle \quad (\alpha = e, \mu, \tau) \tag{2.11}$$

where $|\nu_k\rangle$ are the massive neutrino states. This equation is general: no limits on the number of massive neutrinos have been put. Since it is known that the number of active flavor neutrinos is three, corresponding to ν_e, ν_μ, ν_τ, the number of massive neutrinos must be equal to or greater than three. If the number of massive neutrinos is greater than three, the additional neutrinos in the flavor basis are sterile, and in this case, transitions of active flavor neutrinos into sterile ones can be observed only through the disappearance of active neutrinos.
The massive neutrino states $|\nu_k\rangle$ are eigenstates of the Hamiltonian,

$$H |\nu_k\rangle = E_k |\nu_k\rangle \tag{2.12}$$

with energy eigenvalues

$$E_k = \sqrt{\vec{p}^2 + m_k^2} \tag{2.13}$$

The Schrödinger equation

$$i\frac{d}{dt}\left|\nu_k(t)\right\rangle = H\left|\nu_k(t)\right\rangle \tag{2.14}$$

implies that the massive neutrino states evolve in time as plane waves:

$$\left|\nu_k(t)\right\rangle = e^{-iE_k t}\left|\nu_k\right\rangle \tag{2.15}$$

Considering now a flavour state $|\nu_\alpha(t)\rangle$ which describes a neutrino created with a definite flavour α at time t = 0. Putting together the above equations and taking into account unitarity [29], we end up with:

$$\left|\nu_\alpha(t)\right\rangle = \sum_{\beta=e,\mu,\tau}\left(\sum_k V^*_{\alpha k}e^{-iE_k t}V_{\beta k}\right)\left|\nu_\beta\right\rangle \tag{2.16}$$

Hence, the superposition of massive neutrino states $|\nu_\alpha(t)\rangle$, which is the pure flavor state given in Eq. 2.11 at t = 0, becomes a superposition of different flavor states at t > 0 (if the mixing matrix V is not diagonal, i.e. neutrinos are mixed). The coefficient of $|\nu_\beta\rangle$ is the amplitude of $\nu_\alpha \to \nu_\beta$ transitions as a function of time. The transition probability is then given by:

$$P_{\nu_\alpha\to\nu_\beta}(t) = \sum_{k,j} V^*_{\alpha k}V_{\beta k}V_{\alpha j}V^*_{\beta j}e^{-i(E_k-E_j)t} \tag{2.17}$$

For ultrarelativistic neutrinos:

$$E_k \sim E + \frac{m_k^2}{2E} \tag{2.18}$$

Hence,

$$E_k - E_j \sim \frac{m_k^2 - m_j^2}{2E} = \frac{\Delta m^2_{kj}}{2E} \tag{2.19}$$

and $E = |\vec{p}|$ is the neutrino energy, neglecting the mass contribution. From eq. 2.17 we can see that the oscillation between flavours vanishes if $\Delta m^2_{kj} = 0$, and that oscillation experiments can only measure Δm^2_{kj} and not the absolute mass values.
In the standard 3 neutrino scenario, there are only two independent squared-mass differences: the solar and atmospheric Δm^2's given by:

$$\Delta m^2_{SOL} = \Delta m^2_{12} \simeq 7.4\times10^{-5}eV^2, \tag{2.20}$$

$$\Delta m^2_{ATM} = \mid \Delta m^2_{13} \mid = \mid \Delta m^2_{23} \mid \simeq 2.5\times10^{-3}eV^2 \tag{2.21}$$

Hence, there is a hierarchy of Δm^2's, with $\Delta m^2_{ATM} \simeq 34 \Delta m^2_{SOL}$. By convention, Δm^2_{SOL} is assigned to Δm^2_{12}, with the numbering of the neutrino mass eigenstates such that $m_2 > m_1$. On the other hand, ν_3 can be either heavier than ν_2, in the so-called "**normal ordering**" with $\Delta m^2_{13} > \Delta m^2_{23}$, or lighter than ν_1, in the so-called "**inverted ordering**" with $\Delta m^2_{23} < \Delta m^2_{13}$.
It can be seen how the values of Δm^2 influence the oscillation probabilities if we introduce the oscillation length:

$$L^{osc}_{kj} = \frac{4\pi E}{\Delta m^2_{kj}} \tag{2.22}$$

This equation clearly shows that to **bigger values of Δm^2 correspond smaller oscillation lenghts, i.e faster oscillations**. Furthermore, if considering that ultrarelativistic neutrinos propagate almost at the speed of light, t = L (in units of c=1), where L is the distance between the starting point and the measurement point, and we have:

$$P_{\nu_\alpha \to \nu_\beta}(t) = \sum_{k,j} V^*_{\alpha k} V_{\beta k} V_{\alpha j} V^*_{\beta j} \exp\left(-i \frac{\Delta m^2_{kj} L}{2E}\right) \tag{2.23}$$

hence, depending on neutrino energy and from the distance to the neutrino source, we are able to resolve particular values of Δm^2. An important characteristic of neutrino oscillations is that the transitions to different flavors cannot be measured if:

$$\frac{\Delta m^2 L}{2E} << 1 \tag{2.24}$$

On the other hand, for

$$\frac{\Delta m^2 L}{2E} >> 1 \tag{2.25}$$

only the average transition probability is observable. Since the value of Δm^2 is fixed by nature, different experiments can be designed in order to be sensitive to different values of Δm^2, by choosing appropriate values of the ratio L/E. The so-called sensitivity to Δm^2 of an experiment is the value of Δm^2 for which [29]:

$$\frac{\Delta m^2 L}{2E} \sim 1 \tag{2.26}$$

Different types of neutrino oscillation experiments are traditionally classified depending on the average value of the ratio L/E for an experiment, which determines its sensitivity to Δm^2, and some of them are represented in Tab. 2.2. To better visualize this, in Fig. 2.3 I show the probability of a ν_μ to go into ν_e as function of the distance and each of the 4 plots has a different

Type of experiment	L	E	Δm^2 sensitivity
Reactor SBL	$\sim 10\,\mathrm{m}$	$\sim 1\,\mathrm{MeV}$	$\sim 0.1\,\mathrm{eV}^2$
Accelerator SBL (Pion DIF)	$\sim 1\,\mathrm{km}$	$\gtrsim 1\,\mathrm{GeV}$	$\gtrsim 1\,\mathrm{eV}^2$
Accelerator SBL (Muon DAR)	$\sim 10\,\mathrm{m}$	$\sim 10\,\mathrm{MeV}$	$\sim 1\,\mathrm{eV}^2$
Accelerator SBL (Beam Dump)	$\sim 1\,\mathrm{km}$	$\sim 10^2\,\mathrm{GeV}$	$\sim 10^2\,\mathrm{eV}^2$
Reactor LBL	$\sim 1\,\mathrm{km}$	$\sim 1\,\mathrm{MeV}$	$\sim 10^{-3}\,\mathrm{eV}^2$
Accelerator LBL	$\sim 10^3\,\mathrm{km}$	$\gtrsim 1\,\mathrm{GeV}$	$\gtrsim 10^{-3}\,\mathrm{eV}^2$
ATM	20–$10^4\,\mathrm{km}$	0.5–$10^2\,\mathrm{GeV}$	$\sim 10^{-4}\,\mathrm{eV}^2$
Reactor VLB	$\sim 10^2\,\mathrm{km}$	$\sim 1\,\mathrm{MeV}$	$\sim 10^{-5}\,\mathrm{eV}^2$
Accelerator VLB	$\sim 10^4\,\mathrm{km}$	$\gtrsim 1\,\mathrm{GeV}$	$\gtrsim 10^{-4}\,\mathrm{eV}^2$
SOL	$\sim 10^{11}\,\mathrm{km}$	0.2–$15\,\mathrm{MeV}$	$\sim 10^{-12}\,\mathrm{eV}^2$

Figure 2.2: Types of neutrino oscillation experiments with their typical source–detector distance, energy, and sensitivity to Δm^2, which is given by E[MeV]/L[m] = E[GeV]/L[km]. Table taken from [29].

neutrino energy. From it it is clear that by increasing the neutrino energy, we are firstly sensitive to the bigger oscillations driven by Δm^2_{12} and finally to the ones driven by Δm^2_{13}.

What happens when adding a sterile neutrino?

From the conclusions written above, we expect that when adding a sterile neutrino, we introduce another Δm^2_{14}. Also in this case, the higher is its value, the faster the oscillation will be (see again eq. 2.22). For example, considering $\Delta m^2_{14} = 1\ \mathrm{eV}^2$, L $\sim \varnothing_{EARTH} \sim 12700$ km, from eq. 2.26 we have

$$E \sim TeV \tag{2.27}$$

hence, to study this value of mass (or bigger values), higher neutrino energies have to be considered (with the baseline used by neutrino telescopes). This conclusion is important for the sterile neutrino mass analysis that will be described in the last chapter.

2.3 Neutrino Oscillation in Matter

In 1978, L. Wolfenstein [37] discovered that neutrinos propagating in matter are subject to a potential due to charged and neutral current scattering on

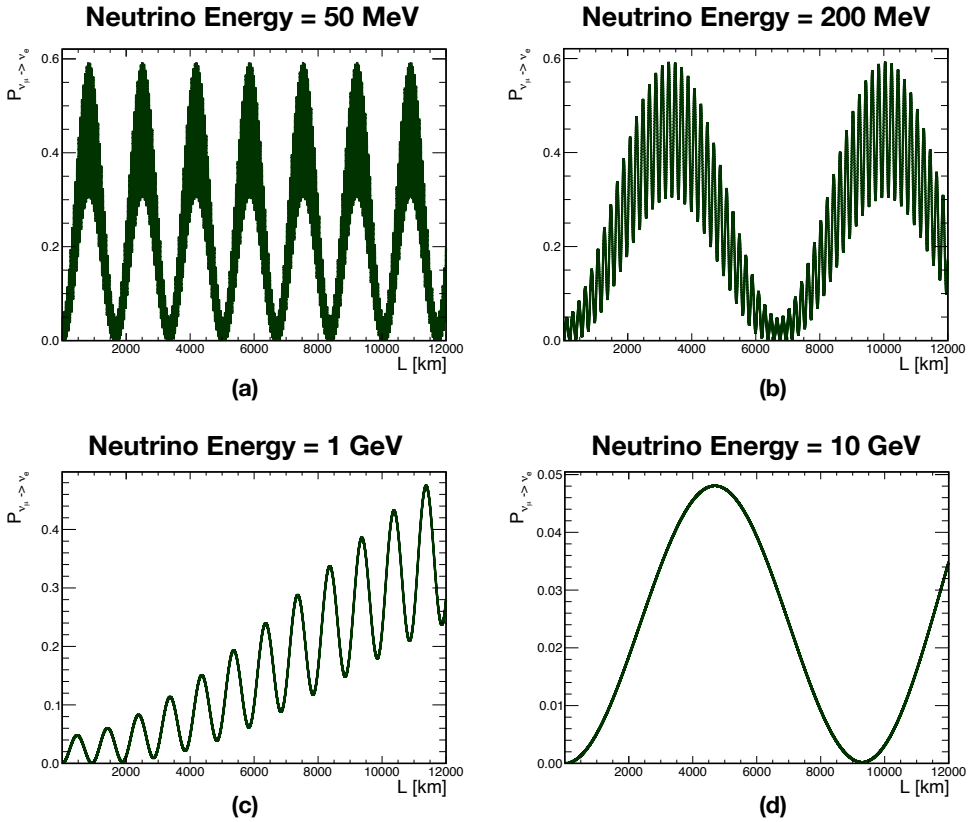

Figure 2.3: Neutrino oscillation probability in vacuum in function of the baseline L for different neutrino energies.

electrons, neutrons, and protons as they propagate through matter. This potential, which is equivalent to an index of refraction, modifies the mixing of neutrinos. This apparently unusual phenomenon, extensively studied by Mikheyev, Smirnov [38] and Wolfenstein, for which it takes the name as MSW effect, has a well known optical analogue: a transparent medium like air or water negligibly absorbs light, but still significantly reduces its speed: $v_{phase} = c/n$, where n is the 'refraction index'. In some materials or in presence of an external magnetic field n is different for different polarizations of light, giving rise to characteristic effects, such as birefringence [35]. The same thing happens for neutrinos. Since matter is composed by electrons (rather than by μ and τ), ν_e interact differently than $\nu_{\mu,\tau}$ giving rise to a flavour-dependent refraction index. Forward scattering of neutrinos interferes with free neutrino propagation, giving rise to refraction. Scattering of ν_l on electrons and quarks mediated by the Z boson (see Fig. 3.7 (a)) is the same

for all flavours $l = e, \mu, \tau$, and therefore does not affect flavour transitions between active neutrinos. The interesting effect is due to $\nu_e e$ scattering mediated by the W boson. In a background composed by non-relativistic and non-polarized electrons and no positrons (e.g. the earth, and to excellent approximation the sun) one can evaluate the matter potential induced by Z and W from electrons, protons and neutrons. In Ref. [39] the calculation of **all** relevant matter potentials that neutrinos experience when propagating through matter in Earth is done. Here, for brevity I report only the results that will be useful to understand the Sterile Neutrino Analysis.
When the neutrinos propagate through matter, the Hamiltonian describing a propagating neutrino flavor has to include the contributions from scattering on particles present. Accordingly, we obtain $H = H_0 + H_I$ where H_0 is the vacuum Hamiltonian and

$$H_I = H_Z^n + H_Z^p + H_Z^e + H_W^e \tag{2.28}$$

where the interaction Hamiltonians are given as $H_Z^i = \mathrm{diag}(V_Z^i, V_Z^i, V_Z^i)$, i = n,p,e, and $H_W^e = \mathrm{diag}(V_W^e, 0, 0)$. The superscript refers to the scattering component while the subscript indicates which gauge boson mediates the reaction, i.e. neutral or charged current. For example, V_Z^e represents the effective matter potential due to NC (neutral-current) scattering on electrons. Note that only matter potentials arising from reactions with electrons, protons, and neutrons, have been included, since the the concentrations of μ and τ particles is virtually zero on Earth. The values of matter potentials for **neutrinos** are here reported from [39]:

$$V_W^e = \sqrt{2} G_F N_e \tag{2.29}$$

$$V_Z^n = -\frac{G_F N_n}{\sqrt{2}} \tag{2.30}$$

$$V_Z^e = -\frac{G_F (1 - 4\sin^2\theta_W) N_e}{\sqrt{2}} \tag{2.31}$$

$$V_Z^p = \frac{G_F (1 - 4\sin^2\theta_W) N_p}{\sqrt{2}} \tag{2.32}$$

These results can not be generalized to be valid also for antineutrinos. In fact in the case of **antineutrinos** the matter potentials have opposite sign with respect to neutrinos:

$$V_{antineutrino} = -V_{neutrino} \tag{2.33}$$

Hence, to build the CC and and NC matter potentials equations from 2.29 to 2.32 have to be put together, considering that:

- the ordinary matter is composed by e, p, n and not by their antiparticles,
- for charge neutrality, $N_e = N_p$,

This way we obtain

$$V_{CC} = V_W^e = \pm\sqrt{2} G_F N_e \tag{2.34}$$

$$\begin{aligned} V_{NC} &= V_Z^e + V_Z^p + V_Z^n \\ &= \mp\frac{G_F(1-4\sin^2\theta_W)N_e}{\sqrt{2}} \pm \frac{G_F(1-4\sin^2\theta_W)N_p}{\sqrt{2}} \mp \frac{G_F N_n}{\sqrt{2}} \\ &= \mp\frac{G_F N_n}{\sqrt{2}} \end{aligned} \tag{2.35}$$

Even if we consider the presence of a sterile neutrino, we have to keep in mind that sterile neutrinos do not carry gauge interactions, hence they do not have either CC or NC couplings with the SM particles. Therefore, in a more general way, if extra sterile neutrinos exist, V_{matter} becomes a bigger diagonal matrix and all its sterile elements vanish [35]. For the case with one sterile neutrino we have:

$$V_{matter} \equiv \sqrt{2} G_F \begin{pmatrix} (N_e - N_n/2) & 0 & 0 & 0 \\ 0 & -N_n/2 & 0 & 0 \\ 0 & 0 & -N_n/2 & 0 \\ 0 & 0 & 0 & 0 \end{pmatrix} . \tag{2.36}$$

2.4 Oscillation Probabilities in the Presence of a Sterile Neutrino

When considering one light sterile neutrino, we have a 4×4 mixing matrix, hence, from eq. 2.5 there are now a total of **6 mixing angles**: the 3 coming from the standard case, and 3 more which are $\theta_{14}, \theta_{24}, \theta_{34}$; and from eq. 2.8 a total of **3 physical phases**, the one coming from the standard case and **2 more** which are δ_{14}, δ_{24}. Considering also the additional Δm^2_{14} there are a total of **6 new free parameters** to account for. The mixing matrix in the (3+1) flavor model can be written as:

$$U \equiv \begin{pmatrix} U_{e1} & U_{e2} & U_{e3} & U_{e4} \\ U_{\mu 1} & U_{\mu 2} & U_{\mu 3} & U_{\mu 4} \\ U_{\tau 1} & U_{\tau 2} & U_{\tau 3} & U_{\tau 4} \\ U_{s1} & U_{s2} & U_{s3} & U_{s4} \end{pmatrix} . \tag{2.37}$$

with the following parameterization:

$$U = R_{34}(\theta_{23})R_{24}(\theta_{24},\delta_{24})R_{14}(\theta_{14})R_{23}(\theta_{23})R_{13})(\theta_{13},\delta_{13})R_{12}(\theta_{12},\delta_{12}) \quad (2.38)$$

The mixing matrix elements which are important in the Sterile Neutrino Analysis are

$$U_{e4} = \sin\theta_{14} \quad (2.39)$$
$$U_{\mu 4} = \cos\theta_{14}\sin\theta_{24} \quad (2.40)$$
$$U_{\tau 4} = \cos\theta_{14}\cos\theta_{24}\sin\theta_{34} \quad (2.41)$$

Fig. 2.4 (a) and (b) aim to give an idea of the impact of some of these

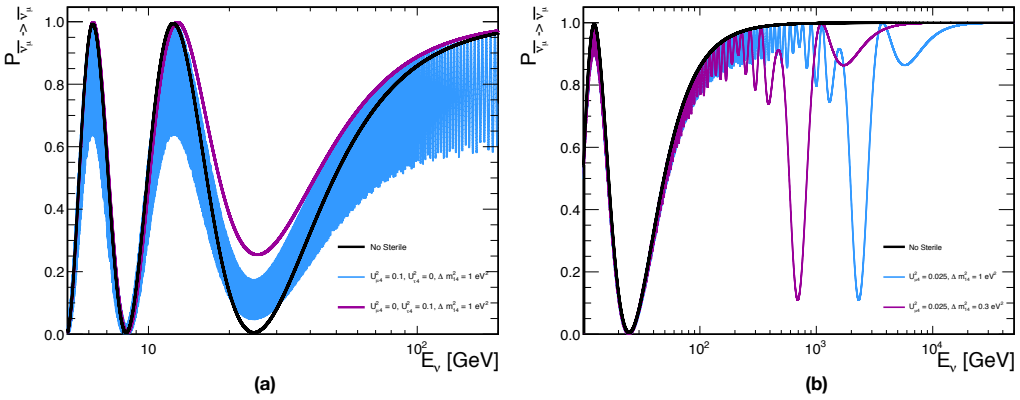

Figure 2.4: Muonic antineutrino disappearance probability in Earth by assuming a baseline L = $\varnothing_{EARTH}$ and comparing the standard case with 3 neutrinos with the case of one additional sterile neutrino.

parameters to the oscillation probabilities: in particular, as stated in sec. 2.2, an additional Δm^2_{14} with a value $> \Delta m^2_{23}$ gives faster oscillations and it can be clearly seen in Fig. 2.4 (b) that there are different signatures given by different values of Δm^2_{14} for higher neutrino energies. Instead, byfix Δm^2_{14} and changing the values of two elements of the mixing matrix 2.37, i.e. $U^2_{\mu 4}$ and $U^2_{\tau 4}$ we have the effect shown in fig. 2.4 (a).

2.4.1 Impact of the additional CP phases: δ_{14} and δ_{24}

Typically, in the sterile neutrino analyses made by other experiments, the two additional CP phases (δ_{14}, δ_{24}) are fixed to 0. Here I want to show that this is in general a wrong assumption for δ_{24} in the standard sterile analysis in which the value of Δm^2_{14} is fixed and the mixing angles θ_{24} and θ_{34} have to be constrained, for two reasons:

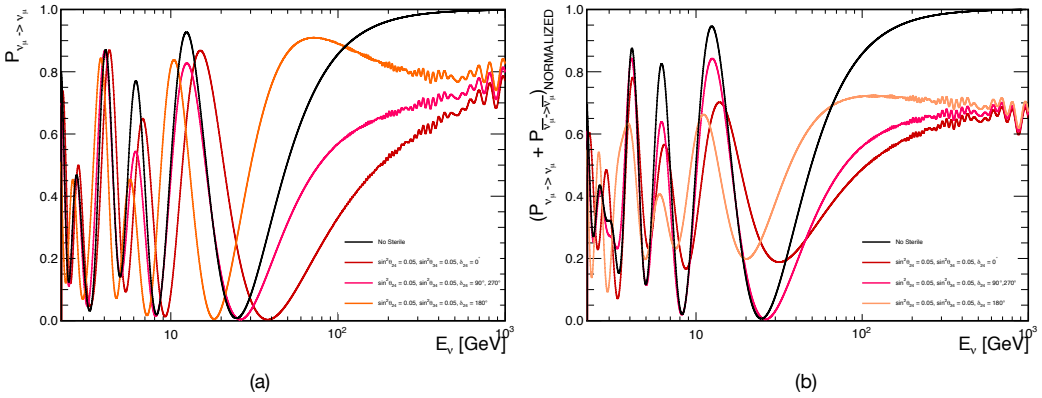

Figure 2.5: ν_μ disappearance probability in the standard 3 neutrinos case and assuming one sterile neutrino with $\Delta m^2_{14} = 1$ and with different values of δ_{24}. The oscillation probabilities have been evaluated with OscProb [40] and here, for both the plots, the *averaged probabilities* are shown, to get rid of the fast oscillations due to the presence of the sterile neutrino mass. In the plots, both $U^2_{\mu 4}$ and $U^2_{\tau 4}$ are $\neq 0$. If $U^2_{\mu 4} = 0$ or $U^2_{\tau 4} = 0$ the effect of δ_{24} vanishes. In (b) the contribution of also antineutrinos has been added to the probability evaluation, weighted by their ratio in the atmospheric neutrino flux and their different cross sections.

1. we have no idea of the value of δ_{24},
2. if we consider the case with both $U_{\mu 4}$ and $U_{\tau 4} \neq 0$ the effect of δ_{24} is actually **not negligible**.

To show this I plot in Fig. 2.5 (a) the ν_μ disappearance probability in the standard 3 neutrinos scenario and assuming a sterile neutrino with $\Delta m^2_{14} = 1$ eV^2, with fixed values of the mixing angles but changing the value of δ_{24}. I have also averaged out the fast oscillations due to Δm^2_{14} (like the light blue curve in Fig. 2.4 (a)) to make the plot easier to visualize. From it it can be clearly seen that δ_{24} impacts quite a lot the oscillation probability in the energy range interesting for both ORCA and ANTARES. To have a more realistic idea of the effect for neutrino telescopes we should keep in mind that they are not able to distinguish between neutrinos and antineutrinos. Hence in Fig. 2.5 (b) I added the contribution of both neutrinos and antineutrinos weighted by assuming their ratio in the atmospheric neutrino flux and their different cross sections. From it, it can be seen that a bit of information is lost but we still expect to have an effect from δ_{24} in the ORCA and ANTARES analyses. This will be shown in Chapter 6.

Finally, Fig. 2.6 shows that in vacuum there is a degeneracy between the neutrino ordering and $\delta_{24} = 0° \rightarrow 180°$. Once matter effects are included, this degeneracy is still valid for $E_\nu > 10GeV$, however it is broken for $E_\nu < 10$ GeV. This is important because the ANTARES energy threshold is $\sim$ 20 GeV, i.e. in that case the degeneracy between ordering and δ_{24} can be assumed, but this is not true for an ORCA-like detector whose energy threshold is $\sim$ 1 GeV.

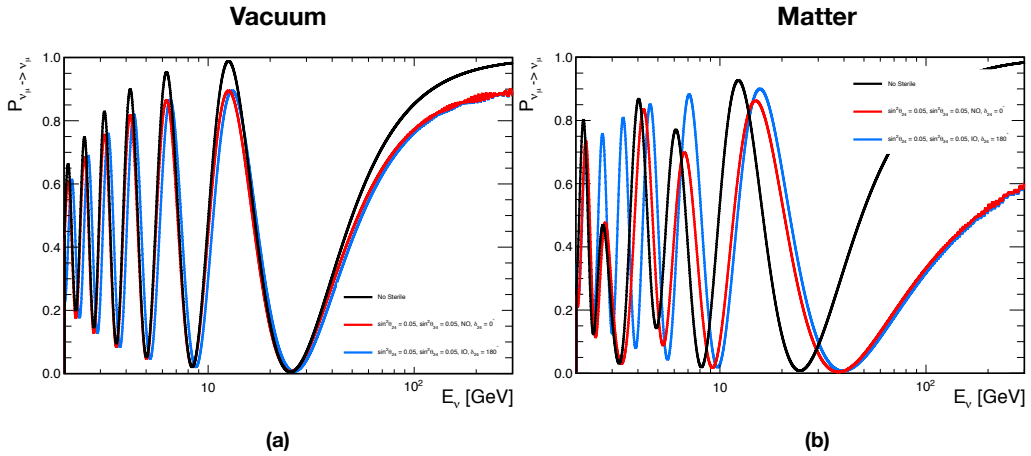

Figure 2.6: Degeneracy between neutrino mass ordering and $\delta_{24} = 0° \rightarrow 180°$ in (a) vaccum and (b) matter. The matter is included with the PREM model and the probabilities are evaluated as "average probability" to get rid of the fast oscillations due to Δm^2_{14}.

For completeness, in Fig. 2.7 the same plot as Fig. 2.5 (a) is shown, but this time by fixing $\delta_{24} = 0$ and changing the value of δ_{14}. The plot shows that δ_{14} **has no impact** in the muon neutrino disappearance in the presence of a sterile neutrino, that is the main observable used by neutrino telescopes when constraining $U_{\mu 4}$ and $U_{\tau 4}$, as it is discussed in the last chapter, hence it can be fixed to 0.

2.4.2 Low Sterile Mass Oscillations

Until now we have focused on $\Delta m^2_{14} > \Delta m^2_{23}$. But in principle, values $< \Delta m^2_{23}$ can be considered. Actually, different experiments show their limits on mixing angles down to $\Delta m^2_{14} = 10^{-5}$ eV^2. To this extent, the best upper limits to date come from the MINOS/MINOS+ experiment [16]. In their analysis [16] that goes down to $\Delta m^2_{14} = 10^{-4}$ eV^2 they detect neutrinos with energies $0 < E_\nu < 40$ GeV thanks to two detectors. The first one,

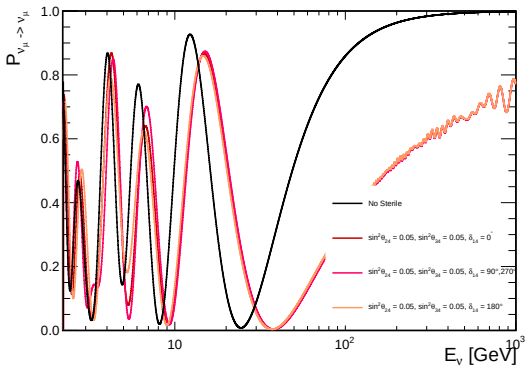

Figure 2.7: ν_μ disappearance probability in the standard 3 neutrinos case and assuming one sterile neutrino with $\Delta m^2_{14} = 1$ and with different values of δ_{14}.

located at 1.04 km from the source, also called Near Detector (ND), and the second, located at 735 km from the source, for which it is referred as Far Detector (FD). With this configuration, neutrinos pass through the Earth's crust. However, due to the relatively short baseline, the crust density which is smaller than the nucleus and the mantle, their analysis is performed in vacuum approximation [16]. Furthermore, for $\Delta m^2_{14} < 0.1$ eV^2 their signal is visible in the FD, hence if we are interested to perform a similar analysis for low neutrino masses, we have to compare our baselines with the one of the FD.
With neutrino telescopes such as ORCA and ANTARES there are 2 advantages with respect to MINOS:

1. longer baselines can be exploited, up to $L = \varnothing_{EARTH}$.
2. matetr effects **can not be neglected** because in our case, the desired neutrinos also travel through the Earth core and mantle.

If we take into account both these 2 points we can see, in Fig. 2.8 the differences in the oscillation probabilities given by different, and small values of Δm^2_{14}.
Already by looking at the oscillation probabilities we can have an idea on what to expect if we perform a mass dependent analysis with both ORCA and ANTARES. This is shown in Fig. 2.9: the effect of low sterile masses is enhanced for neutrino energies < 20 GeV and this is exactly the range for which ORCA is optimised. Instead, for $E_\nu > 20$ GeV the differences become less evident. Considering that the ANTARES energy threshold is ~ 20 GeV, we should not expect high sensitivity for low sterile masses with ANTARES.

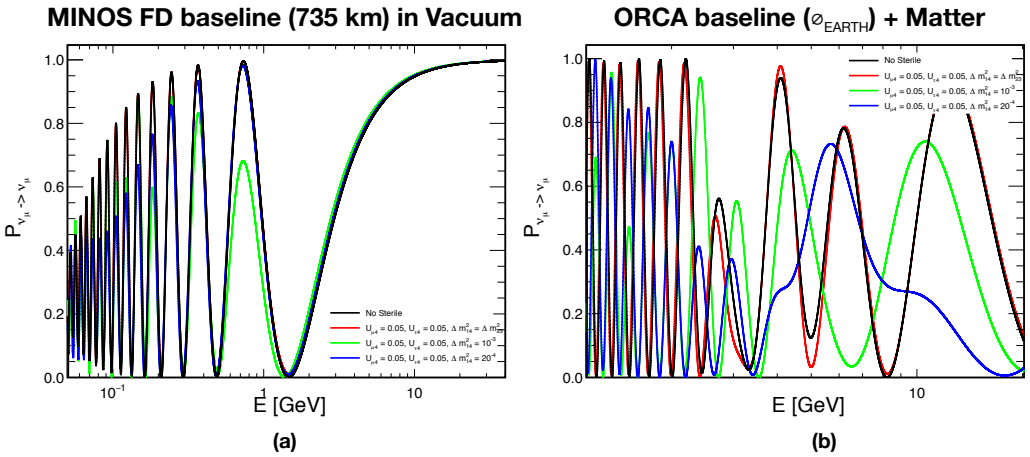

Figure 2.8: Differences in neutrino oscillation probabilities by considering sterile neutrinos with same couplings (i.e. mixing angles) but with different values of Δm^2_{14} for (a) MINOS, FD, with vacuum approximation [16] and (b) ORCA baseline with matter effects with the PREM model [41].

Conclusion

As a conclusion of this chapter I would like to review the main points treated here that will be useful to understand the sterile neutrino analysis of this thesis:

- adding one sterile neutrino to our model introduces 6 new free parameters: 3 mixing angles, one Δm^2 and two CP phases,
- different experiments can constrain some of these parameters,
- the impact of the additional CP phase δ_{24} is not negligible in the sterile neutrino analysis where constraints on $|U_{\mu 4}|^2$ and $|U_{\tau 4}|^2$ want to be put, with a fixed value of Δm^2_{14},
- there is degeneracy, in vacuum, between δ_{24} and the neutrino mass ordering, however, matter effects break this degeneracy in a way that it remains valid only for for $E_\nu > 10GeV$ GeV, this is important because the ANTARES energy threshold is $\sim$ 20 GeV, which means that degeneracy in the ANTARES sterile analysis can be assumed, but for the one made with ORCA, whose energy threshold is $\sim 1-2$ GeV, this can not be done,
- with ORCA we expect to have a big improvement with respect to the current upper limits from MINOS/MINOS+ [16] for low values

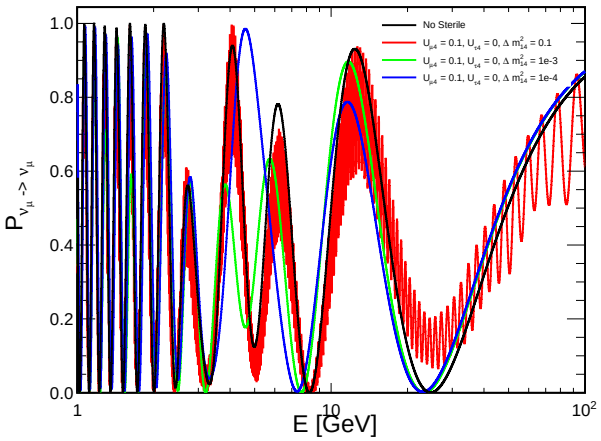

Figure 2.9: Oscillation probability evaluated with OscProb [40] for a baseline of 12000 km and assuming matter effects with the PREM model [41].

of Δm^2_{14}, since longer baseline and matter effects can be exploited.

All these points will be reviewed in the last chapter, which will show the sterile neutrino analysis results.

Chapter 3

Deep Water Neutrino Telescopes

The idea of detecting high energy neutrinos by exploiting huge volumes of transparent medium (water/ice) was first formulated in the 1960s by Markov [42]. But starting from the 1980s, the search for proton decay was the main reason for developing large detectors and underground laboratories. Hence the era of neutrino telescopes is quite new, even if its basic principle is simple: a matrix of light detectors a medium like water, ice, hydrocarbon, argon, gallium and chlorine, which offers large volume of free target for neutrino interactions while providing at the same time a shielding against secondary cosmic rays (CRs). The relativistic charged particles produced by neutrino interaction emit Cherenkov radiation in the transparent medium. If we measure with high precision the number and arrival time of these photons on a three-dimensional array of Photomultiplier Tubes (PMTs), some of the properties of the neutrino (flavor, direction, energy) can be inferred.
The activities for the construction of a neutrino telescope started in the early 1970. The fist projects were DUMAND [43], which was canceled in 1995 since the required submarine technology was not advanced enough at that time, and BAIKAL [45], a telescope in a lake with the same name where the surface is iced during winter.
BAIKAL: Lake Baikal (52°N, 104°E) is the deepest lake in the world, reaching a depth of more than 1600 m and the winter ice covering it as a platform has allowed the construction of a neutrino detector operating since 1993. The ice layer can be used for assembly and deployment of instruments, instead of using ships and underwater remotely operating vehicles. The disadvantage of lake water is that the scattering length is much shorter than in seawater, with a consequent very poor determination of the neutrino direction [47]. The initial detector has been upgraded and it is still operating. Actually,

since 2015, a 1 cubic km telescope, known as Baikal-GVD, which now has 288 modules (representing the first of 8 planned clusters), is taking data [46].
AMANDA: An experiment at the South Pole, at the Amundsen-Scott station where the ice is about 2800 m deep, was pioneered by the Antarctic Muon And Neutrino Detector Array (AMANDA) collaboration [48]. They used a hot water drill to produce holes in the ice, where they put strings of optical sensors before the water in the holes could freeze again. The first AMANDA string was deployed in 1993, at a depth of 800–1000 m [47] and it allowed to find that at that depth the ice had a very short scattering length, ∼50 cm. In 1995–1996 AMANDA deployed 4 strings at depths between 1,500 and 2,000 m which worked as expected, leading to their first atmospheric neutrinos detection. This success led to AMANDA-II, which consisted of 19 strings holding 677 optical sensors [47].
IceCube: At present the only running km3-scale detector is the IceCube neutrino observatory (http://icecube.wisc.edu/) at the geographic South Pole. The instrumented detector volume is a cubic kilometer of highly transparent Antarctic ice and it was built between 2005 and 2010. IceCube uses an array of 5160 Digital Optical Modules (DOMs) deployed on 86 strings at a depth of 1500–2500 m below the surface just above the bedrock in the clear, deep ice. Strings are arranged at the vertices of equilateral triangles that have sides of 125 m. The DOMs are spherical, pressure resistant glass housings containing each a 25 cm diameter photomultiplier tube (PMT) plus electronics for waveform digitization, and vertically spaced 17 m from each other along each string. High quantum efficiency PMTs are used in a denser sub-array located in the center of the detector. This sub-array, called Deep Core, enhances the sensitivity to low energy neutrinos. Finally, a surface cosmic ray (CR) detector, called IceTop, completes the IceCube Observatory. Data acquisition with the complete configuration started in May 2011.
Last but not least, there are ANTARES [58] and KM3NeT [59] in the Mediterranean Sea, which will be better described in this chapter, together with the description of the various steps leading to the detection of the neutrino, starting from the atmospheric neutrino flux production, which is the input of the analysis of this thesis, neutrino detection in water, with its advantages and disadvantages, and the physical principles and technology to make this research possible.

3.1 Atmospheric Neutrino Flux

The interpretation and understanding of the evidence for neutrino oscillations depends on knowledge of the atmospheric neutrino beam. The main

point is to know to what extent uncertainties in the neutrino beam may limit the conclusions about neutrino properties and which features of the evidence for neutrino oscillations are most robust.
The concept of using the atmospheric neutrino beam to look for neutrino oscillations is illustrated in Fig. 3.1: once we have a Cherenkov Telescope (such as could be Super-Kamiokande, Ice Cube, ANTARES or KM3NeT), we can look for neutrinos coming from the opposite Earth hemisphere, also called upgoing neutrinos, which have passed through the Earth. This way we have a long baseline for neutrinos to oscillate and we can also screen from atmospheric muons which represent major the background in these kind of telescopes. With a single detector it is possible simultaneously to cover a

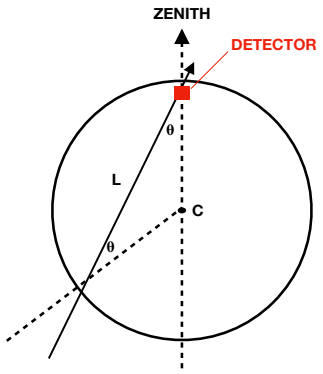

Figure 3.1: Detection scheme of the atmospheric neutrino flux.

range of pathlengths from ~ 10 to $\sim 10^4$ km, corresponding respectively to downward moving and upward moving neutrinos. The atmospheric neutrino beam has an energy spectrum determined by the steeply falling primary cosmic-ray spectrum, which generates the neutrinos by interactions of the cosmic ray nucleons in the atmosphere. In particular, atmospheric neutrinos are produced by the decays of π and K mesons produced in the nuclear interactions of the primary component of cosmic rays in the atmosphere. Tab. 3.2 shows the different production channels with their branching ratios for a p (n) primary cosmic ray. From it we can roughly estimate the expected atmospheric neutrino energy: the neutrino spectrum behaves as $\sim E_\nu^{-2.7}$ at low energies, up to few GeV, then it becomes steeper. This is due to the fact that charged pions with energy above 10 GeV have a Lorentz factor of $\gamma_\pi > 70$ and travel $\gamma_\pi \tau_\pi c > 0.4$ km [52]. The evaluation of the interaction

length for an atmospheric density of about $\rho = 10^{-3}$ g/cm^3 and for a nuclear interaction cross section $\sigma_n = \pi r_n^2$ corresponding to a radius of $r_n = 1$ fm, leads to a mean free path of $\lambda_n = 1/(N_A \rho \sigma_n) = 0.5$ km, where N_A is the Avogadro number. Therefore, the higher the pion energy, the smaller their chance to decay before losing a significant fraction of energy. For this reason, atmospheric neutrinos are distributed as $\sim E_\nu^{-3.7}$ in the region 100 GeV - 100 TeV and depleted at higher energies [52]. The most energetic pions take $\sim$ 1/5 of the energy of the primary, then every decay particle carries away, on average, a similar amount of energy. There are two γ-rays for the π^0 decay and four particles for the full decay of $\pi^\pm$ (see Fig. 3.2) so, on average, the photons are twice as energetic as the corresponding neutrinos. Thus, each γ-ray carries away about 1/10 of the primary energy, while this fraction becomes 1/20 for the neutrino [52].

	Reaction/Decay	Branching ratio (%)
(A)	$p\,(n) + A \rightarrow \pi^\pm X,\ K^\pm X,\ K_L X$	
(B1)	$\pi^\pm \rightarrow \mu^\pm + \nu_\mu\,(\bar{\nu}_\mu)$	99.9877
(B2)	$\rightarrow e^\pm + \nu_e\,(\bar{\nu}_e)$	0.0123
(C1)	$K^\pm \rightarrow \mu^\pm + \nu_\mu\,(\bar{\nu}_\mu)$	63.56
(C2)	$\rightarrow \pi^0 + \mu^\pm + \nu_\mu\,(\bar{\nu}_\mu)$	3.352
(C3)	$\rightarrow \pi^0 + e^\pm + \nu_e\,(\bar{\nu}_e)$	5.07
(D1)	$K_L \rightarrow \pi^\pm + \mu^\mp + \bar{\nu}_\mu\,(\nu_\mu)$	27.04
(D2)	$\rightarrow \pi^\pm + e^\mp + \bar{\nu}_e\,(\nu_e)$	40.55
(E)	$\mu^\pm \rightarrow e^\pm + \bar{\nu}_\mu(\nu_\mu) + \nu_e\,(\bar{\nu}_e)$	100

Figure 3.2: Branching ratios of primary cosmic rays interactions in the atmosphere. Taken from [2].

Calculation of the atmospheric neutrino fluxes requires knowledge of the primary cosmic-ray fluxes and composition, and the hadronic interactions [50]. Atmospheric neutrinos with energy of $\sim$ few GeV are mostly produced by primary cosmic rays with energy of <100 GeV. For primary cosmic-rays in this energy range, a flux modulation due to the solar activity and the effects of Earth's geomagnetic fields should be taken into account. In particular, the atmospheric neutrino fluxes in the low-energy region depend on the location on the Earth. Detailed calculations of the atmospheric neutrino fluxes are performed by Honda [77] with a typical uncertainty of 10 $\sim$ 20%.
From the dominant production mechanism of the atmospheric neutrinos, we can readily understand some relations that exist between the atmospheric ν_μ, $\bar{\nu_\mu}$, ν_e, $\bar{\nu_e}$ fluxes without detailed calculations. For the ratio of the fluxes of $(\nu_\mu + \bar{\nu_\mu})$ and $(\nu_e + \bar{\nu_e})$ at low energies ($\leq$ 1 GeV), where almost all produced muons decay before reaching the ground, we have approximately

$(\nu_\mu + \bar{\nu_\mu})/(\nu_e + \bar{\nu_e}) \sim 2$. As the neutrino energy increases, this ratio increases because an increasing fraction of muons do not decay before reaching the ground (the Earth surface) and being absorbed [2].
Another important feature of the atmospheric neutrino fluxes is that the zenith angle distribution for each neutrino type is up-down symmetric above $\sim$ 1 GeV, if there are no neutrino oscillations. As the neutrino energy becomes lower than $\sim$ 1 GeV, however, zenith angle distributions start to show deviations from up-down symmetric shapes due to the geomagnetic effects on primary cosmic rays.

3.1.1 Uncertainties

A crucial part of the study of oscillation effects with atmospheric neutrinos is a detailed knowledge of the atmospheric neutrino beam at production, before oscillations occur. The uncertainties that we have in the evaluation of the neutrino flux of course impact the oscillation analyses, for which they should be taken into account as systematics. The uncertainties on the calculated flux become a limiting factor when one uses the atmospheric neutrino beam to search for sub-leading effects such as θ_{13} mixing, sub-maximal mixing in the atmospheric sector or effects of solar mixing [50].
In the practice, neutrino fluxes are computed using Monte-Carlo simulations where the the cosmic ray cascade is simulated step-by-step for each track to include all the possible details, such as the Earth's magnetic field, the density profile of the atmosphere, particle energy loss, etc. The primary cosmic ray flux in the energy range $<$ 20 GeV is affected by the Earth's magnetic field, which is the main reason why flux evaluation depends on the location on Earth, and it is also modulated by the solar wind which varies with the 11-year solar cycle [50].
The atmospheric flux has also a zenith angle dependence due to high energy muons that hit the Earth's surface and stop before decaying: this is due to the fact that vertical muons with energy above $\sim$3 GeV have a path length of about 20 km. However, it is possible to have path lengths up to 500 km for horizontal muons and so, in the horizontal fluxes, higher energy neutrinos from muon decay are present.
When dealing with analyses based on the atmospheric neutrino flux, it is important to keep in mind that the main challenge in estimating the uncertainties in neutrino fluxes is to assign the right errors to the different measurements which are taken as input to the calculation, in this sense, the uncertainties we have to date come from:

1. the hadron production uncertainties, these represent the main limita-

tion in the evaluation of the atmospheric neutrino flux,

2. the primary cosmic ray flux uncertainties, which represent a lower level limitation.

The dependence of the fluxes on the atmospheric density as a function of altitude, the details of muon energy loss in the atmosphere and the tracking in the Earth's magnetic field are instead found to be small [50].
The smartest way to limit the impact of these uncertainties is to consider ratios of fluxes: this way large cancellations of these errors occur, because any change in the flux production affects the numerator and denominator in similar ways (e.g. in the ν_μ/ν_e ratio, both the ν_μ and ν_e flavoured neutrinos are mainly produced in association with muons, therefore an increase in e.g. pion production will increase the muon flux by a similar amount which will increase both ν_μ and ν_e fluxes by similar amounts). This cancellation is fundamental in extracting neutrino oscillation information from atmospheric neutrinos. Data analyses are constructed to take advantage of cancellation of uncertainties in the ratios.

3.1.2 Hadron Production Uncertainties

As already stated in the previous section, hadron production uncertainties are the biggest source of uncertainties in computing atmospheric neutrino fluxes. The errors on the hadron production have been estimated using only experimental measurements [50] and the uncertainty is due to the large regions of parameter space (incident parent total energy E_i, secondary total energy E_s, or equivalently, x_{lab}, defined as $\mathrm{E}_s/\mathrm{E}_i$, transverse momentum p_T, target atomic weight A, projectile, secondary particle type) which are only sparsely populated by measurements from accelerators.
Hence, the assignment of uncertainties to the different parts of the parameter space is partially based on the availability of data and partially by extrapolation (when there were no available data). This has largely been done in a model independent way, but with a few guiding indicators.
The uncertainties are incorporated by dividing the phase space for meson production from protons on light-nuclear targets into regions (see Fig. 3.3) and assigning an uncertainty to that region based on the experimental errors and/or the degree to which extrapolation from neighbouring regions in x_{lab}, p_T or target type is required.
The effects of these uncertainties is propagated through the calculation by assigning a weight to each neutrino based on the parent energy and meson type of the first meson produced in the chain of direct descendants within the shower starting from the primary cosmic ray.

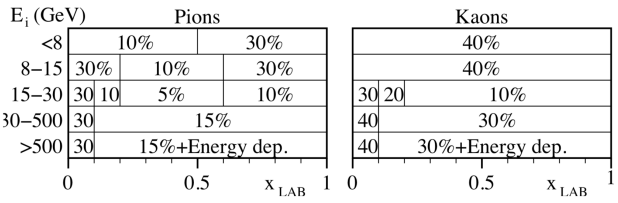

Figure 3.3: Uncertainty assignments for different phase space regions for π and K production. E_i is the energy of the primary. Figure taken from [50].

3.1.3 Primary Flux Uncertainties

Primary flux measurements are challenging because they require a variety of experimental techniques to cover the full energy region between 1 GeV and 10 TeV, moreover, the steeply falling flux as a function of energy makes calibration a critical issue and the experimental apparatus needs to be operated in a hostile environment on a balloon or spacecraft. More precisely, measurements up to 200 GeV/n are possible using balloon or spacecraft, at higher energies instead, fluxes are determined by balloon borne emulsion-calorimeter techniques which are less precise.
The primary flux uncertainties are incorporated into the uncertainties on the neutrino fluxes in a similarly to the hadron production uncertainties. The primary flux has been parameterized by Gaisser, Stanev, Honda and Lipari (GSHL) as:

$$\Phi(E_p) = a\left[E_p + b\exp\left(c\sqrt{E_p}\right)\right]^{-d} \tag{3.1}$$

where E_p is the primary energy in GeV (or GeV/nucleon for nuclear cosmic rays - i.e. no protons) and $d = \gamma + 1$ is the differential spectral index. This parametrisation is an extension to the power-law spectrum:

$$\Phi(E_p) = aE_p^{-d} \tag{3.2}$$

where a is a normalization factor and d the spectral index. The parameters b and c govern the effects of solar modulation on the primary flux and are relevant only at energies < 10 GeV/n.
The parameter d governs the most striking feature of the cosmic ray fluxes: the extremely steep fall-off with energy. The uncertainties are obtained by estimating the variation required in the parameters a to d to suitably cover the spread in the modern measurements. The original values used [50] are shown in Fig. 3.4 (a).
The uncertainty on the parameter d is increased by a factor of three for primaries above 200 GeV/n where the fluxes can not be measured with spectrometers. A more recent work [51] has included recent measurements of

Parameter	Proton fluxes	Nuclear fluxes
a (normalization)	1.49 ± 0.10	0.060 ± 0.004
b	2.15 ± 0.025	1.25 ± 0.03
c	-2.21 ± 0.02	-0.14 ± 0.02
d (index) $<$ 200GeV/n	2.74 ± 0.01	2.64 ± 0.02
$>$ 200GeV/n	2.74 ± 0.03	2.64 ± 0.04

(a)

Parameter	σ		w
	This work	Barr *et al.*	
a	3.9%	6.7%	0.6
b	5.6%	1.4%	4.0
c	17.7%	10.5%	1.7
d	0.3%	0.4%	0.7

(b)

Figure 3.4: (a) Summary of primary flux parameter variation[50]. (b) Updated uncertainties on primary flux parameters [51].

the cosmic-ray primaries collected since 2005. They obtain an uncertainty related to the primary cosmic rays of around (5–15)%, depending on energy, which is about a factor of two smaller than the previously determined uncertainty. The hadron production uncertainty is added in quadrature to obtain the total uncertainty on the neutrino flux, which is reduced by $\sim 5\%$. Fig. 3.4 (b) shows the updated uncertainties on the parameters, compared with the previous work.
Fig. 3.5 (a) and (b) show the updated (from [51]) uncertainties on the total neutrino flux, showing also how much it is impacted by the uncertainties of the primary flux.

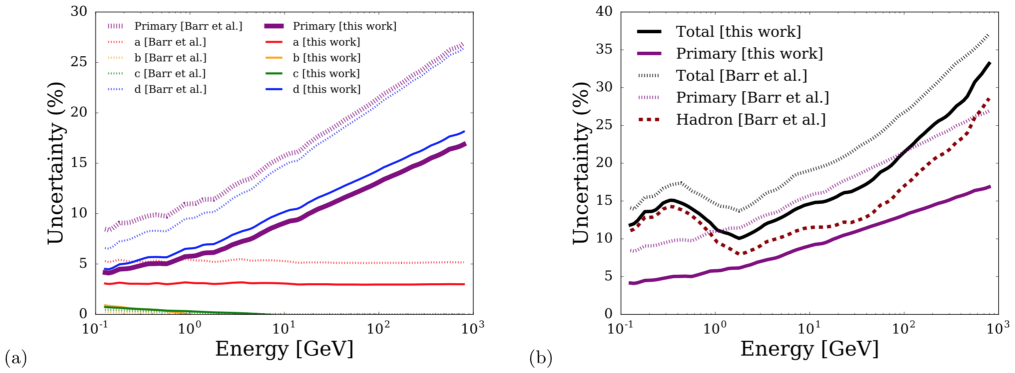

(a) (b)

Figure 3.5: Uncertainties on the primary flux parameters (a) and on the total flux (b). Both figures are taken from [51].

Finally the analyses typically make use of the three neutrino type ratios where error cancellations result in a significant uncertainty reduction. To this extent, Fig. 3.6 shows the uncertainties all three neutrino type ratios averaged over all directions which are important for neutrino oscillation studies. The uncertainties described here enter in the Sterile Neutrino analysis

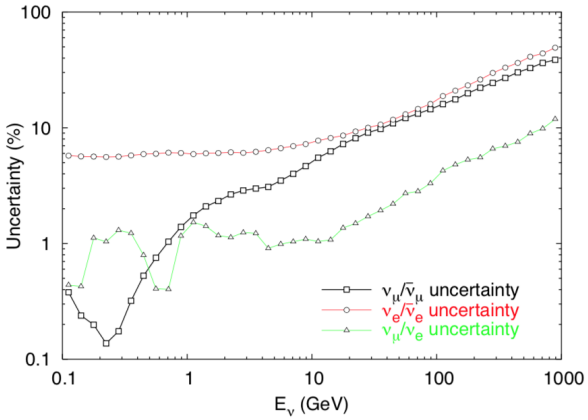

Figure 3.6: Uncertainties all three neutrino type ratios averaged over all directions. Taken from [51].

as systematic errors to be taken into account during the fit. Hence this part will be resumed in Chapter 6.

3.2 Neutrino Interactions

Neutrino interactions are described with an impressive accuracy by the Standard Model. So far no deviations from the standard neutrino interactions have been found in experimental data. To better understand the neutrino interactions interesting for our studies with ORCA and ANTARES it is useful to start by describing the simplest cases of neutrino-lepton scattering and finally describe the more complicated case, the deep inelastic scattering. Before proceeding, it is worth to introduce the variables useful to understand neutrino interaction relations:

$$s = (p_\nu + p_l)^2 \quad \text{(center of mass energy)}, \tag{3.3}$$

$$Q^2 = -q^2 = (p_\nu - k_l)^2 \quad \text{(4-momentum transfer)}, \tag{3.4}$$

$$y = \frac{p_l \cdot q}{p_l \cdot p_\nu} = \frac{E_\nu - E_l}{E_\nu} \quad \text{(inelasticity)}. \tag{3.5}$$

$$x = \frac{Q^2}{2M_{Target}\nu} \quad \text{(Feynman scaling)}. \tag{3.6}$$

$$\frac{1 + \cos\theta^*}{2} = 1 - y \quad \text{(center-of-mass scattering angle)} \tag{3.7}$$

3.2.1 Neutrino-Lepton Scattering

Neutrinos can interact with leptons via the exchange of a Z boson, referred as Neutral Current Interaction (NC), or via the exchange of a W boson, referred as Charge Current Interaction (CC). Fig. 3.7 represents an example of NC and CC interaction in the case of $\nu - e$ scattering.

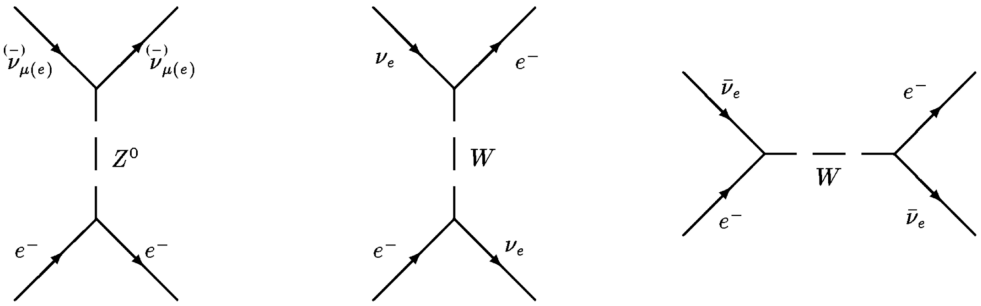

(a) (b) (c)

Figure 3.7: Feynman diagrams for NC (a) and CC (b, c) scattering of $\nu - e$.

In the case of a ν_f CC interaction with a free fermion:

$$\nu_f \, l \rightarrow f \, l^* \tag{3.8}$$

a charged lepton is produced. The cross section for this process is [29]:

$$\sigma = \frac{G_F^2 s}{\pi} = 17.2 \times 10^{-42} \, \mathrm{cm}^2 \times \mathrm{E}_\nu/\mathrm{GeV} \tag{3.9}$$

And it shows that the neutrino cross section grows linearly with neutrino energy, and since:

$$s = m_l^2 + 2 m_l E_\nu \tag{3.10}$$

it is evident that the cross section also depends on the mass of the target, hence if we consider as targets electrons (e) and nucleons (n), we have that:

$$\sigma_n \sim 10^3 \sigma_e \tag{3.11}$$

This is important because it tells us that a neutrino traveling in water has an higher probability to scatter of nuclei/nucleons than on the atomic electrons, and the scattering with nucleons produces hadronic showers, as we will se in the next section.

Finally, eq. 3.9 shows that the cross section does not depend on the neutrino-lepton scattering angle: this is completely true for massless leptons, for which chirality and helicity coincide, but we can assume it also when the considered energies are $>> m_l$. In particular, since the neutrino is left-handed, and the same is for the lepton, we have a total spin along the interaction axis equal to 0, i.e. s-wave, which is isotropic, hence there is not a preferred direction. This is not true for the antineutrino: in fact antineutrinos are right-handed, hence in this case the total spin along the interaction axis is 1, i.e. p-wave, which has an angular dependence. In particular:

$$\frac{\sigma_{CC}(\nu\, l)}{\sigma_{CC}(\bar{\nu}\, l)} = 3 \tag{3.12}$$

Hence, due to this helicity difference and an integration over all the solid angle, the antineutrino cross section is 1/3 of the neutrino cross section.
In the case of a NC interaction:

$$\nu_f\, l \rightarrow \nu_f\, l \tag{3.13}$$

the Z boson couples with both the left and right-handed components of the lepton. Hence, in this case, the total cross section is the sum of the two cross sections (with spin J=0,1).

3.2.2 Neutrino-Nucleus Scattering

The standard matter is composed by nuclei and electrons. Neutrinos can interact with both of them, however, as already shown in the previous section, the cross-section is much smaller for electrons than for nucleons. Ideally then experiments would like to study neutrino interactions directly on nucleons, but a target of pure neutrons is similarly impractical to construct. Driven by the need for higher interaction rates in large active detectors, experiments build their detectors around targets of heavier nuclei such as carbon, oxygen (water) or iron. But the fact that the target nucleons are then contained within a nucleus, and the fact that they have a complex internal structure introduces effects which significantly complicates the resulting interactions observed in the detector.
Furthermore, as we move up farther in neutrino energy, the description of the scattering becomes increasingly more diverse. In the energy range from $\sim$ 1 GeV up to 10 GeV, there are several distinct neutrino scattering mechanisms which compete with each other. The possibilities fall into three main categories [54]:

1. **Elastic and quasi elastic scattering:** Neutrinos can elastically scatter off an entire nucleon liberating a nucleon (or multiple nucleons) from the target.

2. **Resonance production:** Neutrinos can excite the target nucleon to a resonance state. The resultant baryonic resonance (Δ, N^*) decays to a variety of possible mesonic final states producing combinations of nucleons and mesons.

3. **Deep Inelastic Scattering:** Given enough energy, the neutrino can resolve the individual quark constituents of the nucleon. This is called deep inelastic scattering and manifests in the creation of a hadronic shower.

The result of these competing processes is that the final products of neutrino interactions include a variety of states ranging from the emission of nucleons to more complex final states including pions, kaons, and collections of mesons. This energy regime is often referred to as the "transition region" because it corresponds to the boundary between quasi-elastic scattering (in which the target is a nucleon) on the one end and deep inelastic scattering (in which the target is the constituent parton inside the nucleon) on the other.

Quasi Elastic Scattering (QE)

For neutrino energies less than $\sim$ 2 GeV, neutrino-hadron interactions are predominantly quasi-elastic (QE), which means that the neutrino scatters off an entire nucleon rather than its internal constituents, the partons. In a charged current neutrino QE interaction, the target neutron is converted to a proton. In the case of an antineutrino scattering, the target proton is converted into a neutron [54]:

$$\nu_f \, n \rightarrow f^- p, \quad \bar{\nu}_f \, p \rightarrow f^+ n \tag{3.14}$$

where f is the flavour of the considered neutrino. The final state is typically a single nucleon, but it can also include multiple nucleons.

Resonance Production (RES)

Given enough energy, neutrinos can excite the nucleon to an excited state, giving rise to an inelastic process. The excited states are baryon resonances (N^*) which quickly decay, typically in a nucleon and single pion final state:

$$\nu_l + N \rightarrow l^- + N^* \tag{3.15}$$

$$N^* \rightarrow \pi + N' \tag{3.16}$$

where N,N' = n,p. Other higher multiplicity decay modes are also possible.

Deep Inelastic Scattering (DIS)

At sufficient energies, the neutrino is able to transfer sufficient momentum that the internal structure of the nucleon can be resolved. In deep inelastic scattering, the neutrino scatters off a parton in the nucleon via the exchange of a virtual W or Z boson producing a lepton and a hadronic system in the final state. Both CC and NC processes are possible:

$$\nu_l\, N \rightarrow l^-\, X \quad \bar{\nu}_l\, N \rightarrow l^+\, X, \quad l = e, \mu, \tau \tag{3.17}$$

$$\nu_l\, N \rightarrow \nu_l\, X \quad \bar{\nu}_l\, N \rightarrow \bar{\nu}_l\, X, \quad l = e, \mu, \tau \tag{3.18}$$

The current interpretation of the DIS processes is based on the quark–parton model of hadrons [55]. According to this model, a nucleon is a composite system of three valence quarks and a sea of quark–antiquark pairs of all flavors. In the DIS processes, the intermediate virtual gauge boson (W, Z) which connects the lepton vertex to the hadronic vertex interacts directly with the quark constituents of the nucleon.
To better understand the DIS process it is easier to start by considering the elastic scattering process of neutrinos on nucleons. In this case the total cross section rises linearly with energy, for sufficiently low energies. However, if the Q^2 of the reaction is high enough, the differential elastic cross section, $d\sigma/dQ^2$ will start to fall with Q^2 because the nucleon will break apart when too much Q^2 is transferred. At some point, the cross section stops to rise with energy because the elastic process only occurs up to a finite Q^2, and the s at this high energy exceeds that Q^2. However, at the same point, new inelastic processes will become energetically possible, such as the production of a single pion. These will rise with energy, initially quadratically and then linearly until they too reach their Q^2 limit, at which point their cross section stops rising with energy [55]. As illustrated in Figure 3.8 (a), this process repeats itself, resulting in a linear rise of the total cross section with energy.

A linear rise with energy is expected in the case of point like scattering. This simple picture, while possibly helpful in the region of transition between elastic and inelastic scattering, is not a good explanation for understanding the high energy behavior of inelastic scattering. Instead, this inelastic process can be described as scattering of neutrinos from quarks inside the strongly bound system. Quarks are fundamental particles, and therefore the cross

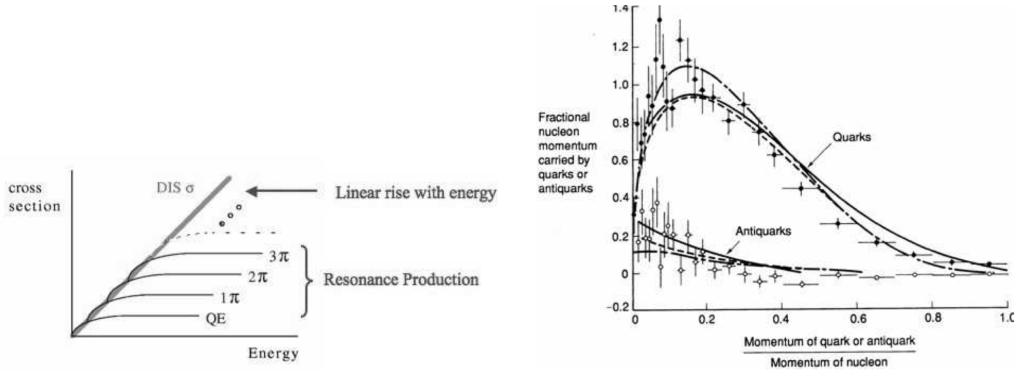

(a) (b)

Figure 3.8: (a) Diagram representing the rise of the cross section with energy including all the inelastic channels appearing with growing energy. (b) Quark and anti-quark momentum density distribution in the nucleon as a function of x. Both figures are taken from [55].

section of neutrino quark scattering will rise linearly with energy. However, these quarks are not free, but they are surrounded by other quarks/gluons. Hence, to really understand and describe deep inelastic scattering, we have to keep in mind this.

In scheme of neutrinos scattering from constituents of strongly bound systems, the variable x defined in eq. 3.6 represents the fractional momentum of the target nucleon carried by the parton in a frame where the target momentum is very large. The basic idea of this frame is that the nucleon is seen by the incoming lepton as flat and static because of length contraction and time dilation, and the incoming lepton interacts with a single one of these frozen partons, carrying a momentum fraction x (see Fig. 3.8 (b) which shows an illustration of typical quark and anti-quark distributions in a nucleon at moderate Q^2).

If we finally focus on chirality and total spin in neutrinos-quarks interactions, we have that in the high energy limit helicity and chirality are equivalent, hence for the case of a quark, the charged-current weak interaction will select left-handed quarks just as it did left-handed electrons, and the net spin along the interaction axis will be zero. By contrast, for the case of neutrino scattering from anti-quarks, the target will be right-handed in the center-of-mass frame, and in this case the net spin along the interaction axis will be one. This fact, combined with the smaller momentum fraction carried by

antiquarks than is carried by quarks (Fig. 3.8 (b)), means that:

$$\sigma_\nu \sim 2\,\sigma_{\bar{\nu}} \tag{3.19}$$

Overview

Fig. 3.9 shows the neutrino (a) and antineutrino (b) cross sections divided by energy in the region where the three processed described above (QE, RES, DIS) compete with each other.

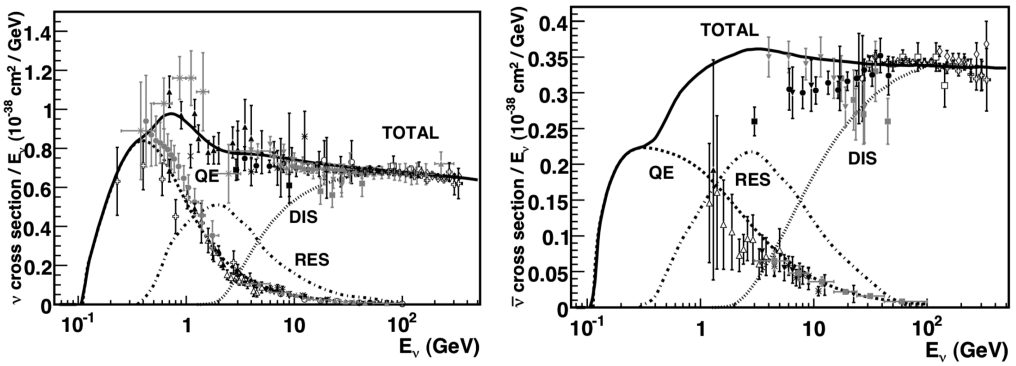

(a) Neutrino (b) Antineutrino

Figure 3.9: Neutrino (a) and Antineutrino (b) cross sections divided by neutrino energy. In both the figures are shown the contributions to the total cross section of the three processes in this energy region: quasi elastic scattering (QE), resonance production (RES), deep inelastic scattering (DIS).

The figure teaches us three main things. First, the total cross sections approaches a linear dependence of neutrino energy. This scaling behavior is predicted by the quark parton model [55] and is expected if point-like scattering off quarks dominates the scattering mechanism, for example in the case of deep inelastic scattering. Such assumptions break down, of course, at lower neutrino energies (i.e., lower momentum transfers). Second, antineutrino cross sections are typically less well-measured than their neutrino counterparts. This is generally due to lower statistics and larger background contamination present in that case. Third, the antineutrino cross section is $\sim$ a factor 3-2 (in function of energy) smaller than the neutrino cross section. This has to be taken into account when we want to evaluate the expected events in our Cherenkov telescopes.

Summary

The message of this section is that a precise evaluation of neutrino scattering on nuclei/nucleons is not straightforward. Especially in the energy region < 10 GeV, which is the transition region. Ref. [53] shows that a simple extrapolation of DIS in this low energy region is not a good option, since it does not take into account nonperturbative effects which may be important. The way to deal with these uncertainties is to consider them as systematics in our analyses.

3.3 Event Topologies in Neutrino Telescopes

The neutrino interactions discussed in the previous section, give **two** different event topologies in neutrino telescopes.
The first are **track-like** events (Fig. 3.10 (a)), in which a ν_μ interacts CC with the target, producing a muon which in the water has a path of:

$$L_\mu \sim 4\,\mathrm{m/GeV} \tag{3.20}$$

in the muon energy region of few GeV up to 1 TeV. Hence it produces a long track in the water.
Then there are the **shower-like** events (Fig. 3.10 (b)) which can be produced in different ways:

- ν_e CC interactions which produce an electron that starts an **electromagnetic shower**.
- **All** NC and CC interactions of neutrinos with nuclei produce **hadronic showers**.

Already from Fig. 3.10 (a-b) we can see that a shower is shorter and more extended with respect of a track, and this has a consequence that the direction estimation of a track is easier to reconstruct. Since my thesis was focused on shower reconstruction, more details on showers topology will be given on the corresponding chapter. Now it is useful to understand how these events are observed in a neutrino telescope, and to do this the Cherenkov effect has to be introduced.

3.4 The Cherenkov Effect

When a fast charged particle travels at a uniform velocity in a dielectric medium, the associated electromagnetic field close to the particle polarizes

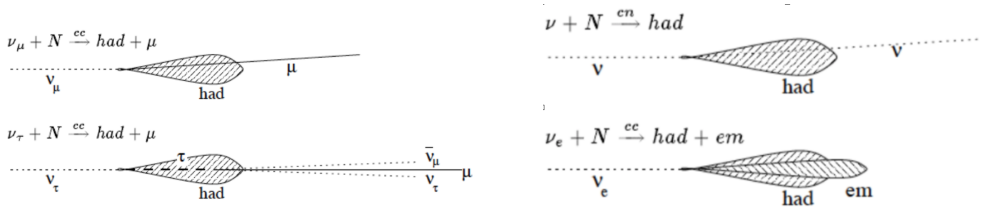

Figure 3.10: Track-like (a) and shower-like (b) events seen in a neutrino telescope.

the medium along its track, so that the electrons attached to the atoms follow the waveform of the pulse as the particle goes by. It is most important to realize in this process that the atoms are not excited by the electron and neither are they removed from their bound states (ionization). It is true that there is in addition ionization, when the impacts are sufficiently close, but the process with which we are concerned here arises from only very small displacements by a very large number of electrons. Now, in the general case, when the particle is slow, the radiation from these displaced electrons, which return immediately to their normal positions after the particle has passed, is not observed, owing to destructive interference. If, however, the velocity of the particle in the medium is faster than the phase velocity of light in the medium, the wavelets from all portions of the track are in phase with one another on a wavefront inclined to the direction of the track, and a coherent radiation is then observed [56]. From Fig. 3.11 (a), if a particle traverses a distance AB inside a dielectric medium at a high velocity βc, where c is the velocity of light in vacuum, and we denote separate points P_1, P_2, P_3 as sources of spherical wavelets, then the resulting wavefront will lie along the line BC, and the direction of emission of the radiation will be along the line AC, at right angles to BC. Now, the distance the particles will have gone in a time Δt, will be $AB = \beta c \Delta t$; in the same time the light will have travelled a distance $AC = (c/n)\Delta t$ where n is the refractive index of the medium. From these two equalities it is at once seen that there is a very fundamental relation between the velocity of the particle, the refractive index of the medium, and the angle at which the light is emitted. This, known as the Cerenkov relation, is:

$$\cos\theta_C = (1/n\beta), \quad \beta = v/c \tag{3.21}$$

Thus we see that the Cerenkov effect is the electromagnetic or optical analogue of the "supersonic bang," or the bow wave from a ship travelling through water faster than the natural velocity of surface waves on the water.

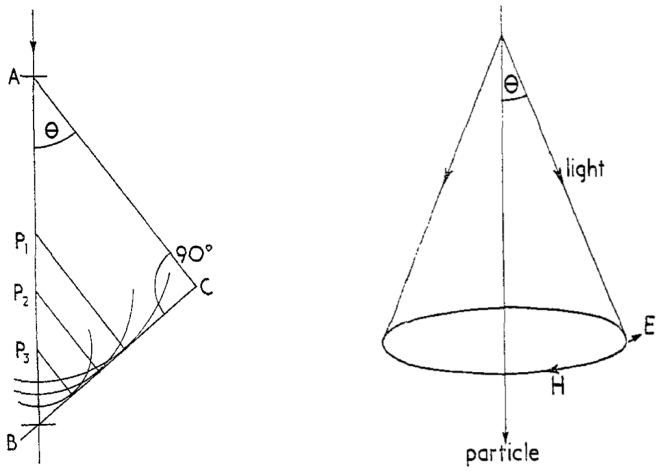

(a) (b)

Figure 3.11: Representation of the Cherenkov effect. Taken from [56].

From eq. 3.21 we can conclude 2 things:

1. There is a **threshold** condition, when $\beta_t = 1/n$ and $\theta = 0$, below this value, no radiation takes place.

2. There is a **maximum angle** at which the light may be emitted, when the particle is travelling at ultra relativistic velocities. This arises when $\beta \to 1$, in which case $\theta_{max} \to \cos^{-1}(1/n)$.

Fig. 3.11 (a) has only been drawn in one plane and the light is emitted over a conical surface, the axis of which coincides with that of the particle. The radiation has unique polarization properties, the electric vector $\vec{E}$ is always at right angles to the direction of propagation of the light, and the magnetic vector $\vec{H}$ is always tangential to the surface of the cone, as in Fig. 3.11 (b). Eq. 3.21 shows that the relation between the Cherenkov angle and the particle velocity is inherently limited by the material in which the Cherenkov radiation is emitted. In order to distinguish between relativistic particles, Cherenkov detectors require the radiator materials to have a relative permittivity ϵ_r ($n = \sqrt{\epsilon_r}$) very close to unity, otherwise the Cherenkov angle would saturate to a value independent of the particle velocity.
It should be mentioned that most materials are dispersive, i.e. their refractive index varies with frequency. Therefore the photons of different energy are scattered in various angles. In this case the radiation is concentrated in a thin conical shell whose vertex is at the moving charge, and whose opening

half-angle η is given by [2]:

$$\cot\eta = \Big[\frac{d}{d\omega}(\omega\tan\theta_C)\Big]_{\omega_0} = \Big[\tan\theta_C + \beta^2\omega n(\omega)\frac{dn}{d\omega}\cot\theta_C\Big] \tag{3.22}$$

where ω_0 is the central value of the small frequency range under consideration. This cone has a opening half-angle η, and, unless the medium is non-dispersive ($dn/d\omega = 0$), $\theta_C + \eta \neq 90°$.
The number of photons produced per unit path length of a particle with charge ze and per unit energy interval of the photons is:

$$\begin{aligned}\frac{d^2N}{dEdx} = \frac{\alpha z^2}{\hbar c}\sin^2\theta_C = \frac{\alpha^2 z^2}{r_e m_e c^2}\big(1 - \frac{1}{\beta^2 n^2(E)}\big) \\ \sim 370\sin^2\theta_C(E)\mathrm{eV}^{-1}\mathrm{cm}^{-1}(z=1)\end{aligned} \tag{3.23}$$

or, equivalently,

$$\frac{d^2N}{dxd\lambda} = \frac{2\pi\alpha z^2}{\lambda^2}\big(1 - \frac{1}{\beta^2 n^2(\lambda)}\big) \tag{3.24}$$

This formula shows that shorter wavelengths contribute more significantly to Cherenkov radiation. However, photons with wavelengths below 300 nm are strongly suppress by the light absorption of water/ice. Typically, the number of Cherenkov photons emitted per cm of track length is about 340 in the wavelength between 300 and 600 nm which is appropriate for detection by photomultiplier tubes (PMT) [29].

3.5 Photomultiplier Tubes (PMTs)

A PMT converts light into an electrical signal, then amplifies that signal by the emission of secondary electrons. Fig. 3.12 (a) shows the basic elements:

- a photocathode which converts light flux into electron flux;
- an electron-optical input system which focuses and accelerates the electron flux;
- an electron multiplier consisting of a series of secondary-emission electrodes (dynodes);
- an anode which collects the electron flux from the multiplier and supplies the output signal.

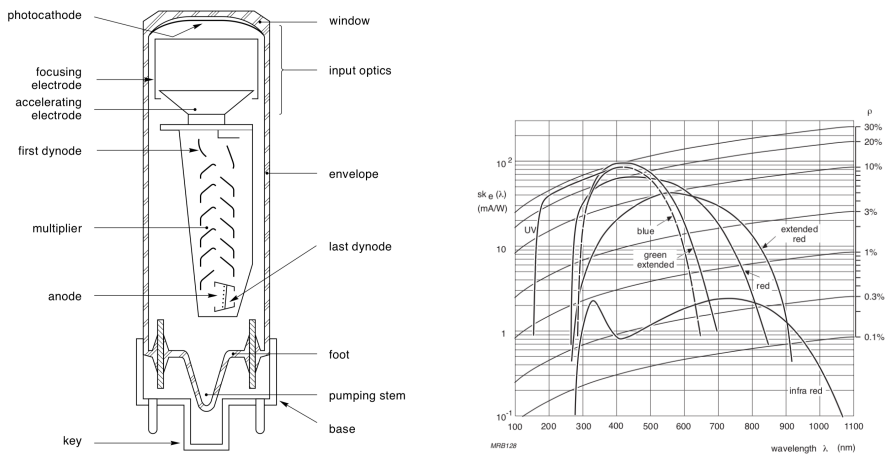

(a) (b)

Figure 3.12: caption

The two fundamental phenomena for the operation of a photomultiplier are photoemission and secondary emission. Photoemission the process for which an incident photon hits the photocathode material and gives its energy to a bounded electron, giving it enough energy to escape. If the number of the photoelectrons escaping from the photocathode and hitting the first dynode is n_k, and the dynode gain is g_1, the number of resulting secondary electrons is $n_k g_1$. Then, assuming the second dynode to have a gain g_2, it in turn emits $n_k g_1 g_2$ electrons. The process repeats from dynode to dynode up to the anode where the electrons are finally collected. If N is the number of dynodes, the number of electrons collected is:

$$n_a = n_k \prod_{i=1}^{N} g_i \tag{3.25}$$

For example, assuming the gain of each dynode equal to 4, the current amplification M of a ten-stage multiplier is:

$$M = \frac{n_a}{n_k} = \prod_{i=1}^{10} g_i \approx 10^6 \tag{3.26}$$

This process is enhanced by accelerating and focusing electrons with electric fields between the dynodes.
The cathodes normally used in photomultipliers are made of a deposited photoemissive semiconductor. They can mainly be dived in two classes [57]:

- semi-transparent cathodes, the most widely used, deposited on the inside of the input window; electrons are emitted from the side opposite

to the incident light. The cathode can be large (from ten to a few hundred millimetres in diameter) and the window on which it is deposited can be flat or curved.

- opaque cathodes, deposited on a metal electrode inside the tube. Electrons are emitted from the illuminated side. The area is usually limited to a few square centimetres because of the size of the focusing electrodes.

From the standard types, the most used photocathode materials are silver-oxygen-caesium (AgOCs), antimony- caesium (SbCs), and the bi-and trialkali compounds SbKCs, SbRbCs, and $SbNa_2KCs$. Examples of the sensitivities of different photocathodes as functions of wavelength, known as spectral sensitivity characteristics, are shown in Fig. 3.12 (b). They are limited at long wavelengths by the photoemission threshold of the material, and at short wavelengths by the transmission of the window [57].
It is useful to introduce also the gain of a PMT, defined as the ratio I_a/I_k of the anode current I_a due to a cathode photocurrent I_k:

$$G = \frac{I_a}{I_k} \tag{3.27}$$

It can be shown [57] that the gain increases rapidly with the applied voltage:

$$G = \prod_{i=1}^{N} k_i V_i^{\alpha} \tag{3.28}$$

where k_i is a proportionality constant, V_i the inter-dynode voltage per stage and α is between 0.6 and 0.8 [57]. Since V_i is a fraction k_i' of the supply voltage V_{th}, we have:

$$G = \prod_{i=1}^{N} k_i (k_i')^{\alpha} V_{th}^{\alpha} = K V_{th}^{N\alpha} \tag{3.29}$$

where the constant K depends on the dynodes material and the voltage division between them [57]. Thus, the gain for a 10-stage tube increases as about the 7th power of the supply voltage. With tubes available to date, gains of 10^6 are often obtained with supply voltages between 800 V and 1200 V.

Environmental Considerations

Environmental factors such as temperature, magnetic fields, background radiation and atmosphere can affect the operation of a photomultiplier in varying degrees, temporarily or permanently [57]. In some cases, the effects can

be compensated. Magnetic fields even as weak as the Earth's affect photomultiplier performances. In fact, a rotation of the horizontally mounted tube about its main axis shows a variation of anode sensitivity due to the varying effect of the Earth's field on the electron trajectories, and the corresponding variation of collection efficiency in all stages. Highly focused tubes, in which the electron impact areas on the dynodes are small, are the most sensitive to magnetic effects; a transverse flux density of a few tenths of a millitesla can reduce gain by 50%. Magnetic influence is greatest in the electron-optical input system, where electron trajectories are longest. Increasing the voltage across the input system increases the energy of the electrons and decreases the sensitivity to magnetic fields.

3.6 ANTARES

ANTARES is an acronym for 'Astronomy with a Neutrino Telescope and Abyss environmental RESearch'. It is a deep-water neutrino telescope located at a depth of 2475 m in the Mediterranean Sea, 40 km off the coast of Toulon (France). The basic detection element is the optical module (OM), a 17" inches glass sphere, housing a 10" photomultiplier tube and the electronics that provide the high voltage. Three OMs are grouped together, looking downwards at 45°, together with a titanium container, the Local Control Module (LCM) which houses the offshore electronics and embedded processors (see Fig. 3.13 (a)), to form a storey and 25 vertical storeys compose a string, for a total of 12 strings. The distance between two adjacent floors is 14.5 m and 100 m from the seabed to the first storey (see Fig. 3.14 (a)).
The Data Acquisition system (DAQ) is based on the "all-data-to-shore" concept: all signals from the PMTs that pass a preset threshold (typically 0.3 Single Photo Electron (SPE)) are digitized in a custom built ASIC chip, the Analogue Ring Sampler (ARS) [58], and all digital data are sent to shore where they are processed in real-time by a farm of commodity PCs. The data flow ranges from a couple of Gb s^{-1} to several tens of Gb s^{-1}, depending on the level of the submarine bioluminescent activity. In ANTARES the data from the 3 OMs are digitised in the LCM, which contains an FPGA and a microprocessor which outputs the digitised data. The card is also equipped with dedicated memory to allow local data storage and it manages the delayed transmission of data in order to avoid network congestion.
The photomultiplier tube selected for the ANTARES detector is the Hamamatsu R7081-20 which has a diameter of 10 inches and has 14 amplification stages. The timing resolution of the PMT is one of the key parameters that determine the angular resolution of the detector. It is determined by the

spread in the transit time. This transit time spread (TTS) is about 1.3 ns (RMS) for this PMT. A large part of the PMT is enclosed in a cage of high permeability metal, which serves to shield the Earth's magnetic field, which, in the ANTARES site, has a magnitude of approximately 46 μT and points downward at 31.5° from the vertical, thus optimising the uniformity of the PMT response (see Fig. 3.13 (b)).

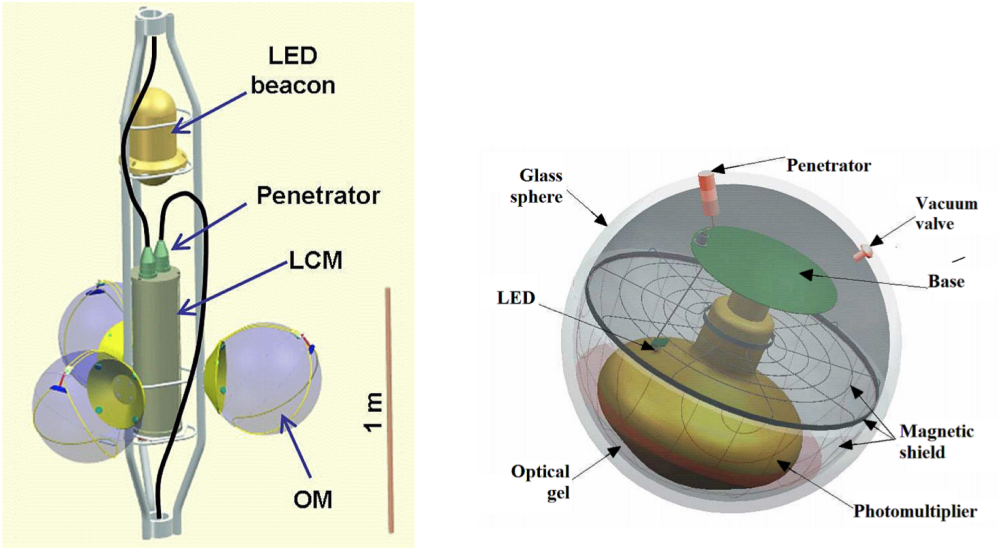

(a) (b)

Figure 3.13: (a) ANTARES storey. (b) ANTARES optical module.

With its geometry, ANTARES has an energy threshold of $\sim$ GeV and its performances are shown in Tab. 3.1. Further details on the ANTARES Tele-

ANTARES	Angular Resolution	Energy Resolution
Tracks	$< 0.4°$, for E $>$ 10 TeV	~ 0.35 in $\log_{10}(E_{reco}/E_{\mu})$
Showers	$< 3°$, for 1 TeV $<$ E $<$ 0.5 PeV	$\sim 10\%$

Table 3.1: ANTARES direction and energy resolutions for track-like and shower-like events.

scope will be given in the next chapters. For an overview I refer to [58].

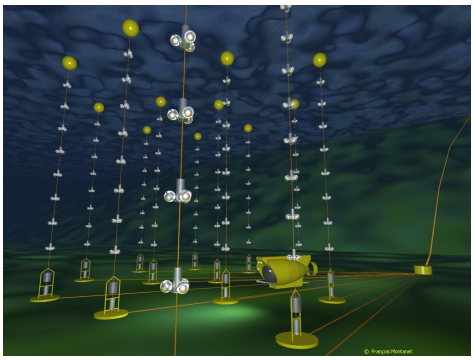

(a)

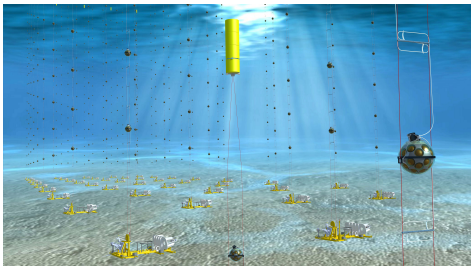

(b)

Figure 3.14: (a) ANTARES representation. (b) KM3NeT representation.

3.7 KM3NeT/ORCA & ARCA

The KM3NeT Collaboration has planned and started the construction of a multi-potential neutrino telescope located in the Mediterranean Sea [59]. The telescope will be composed of 3 building blocks; two of them will be located 80 km off-shore of Portopalo di Capo Passero, in Sicily (Italy), and they are referred as ARCA (Astroparticle Research with Cosmics in the Abyss). The remaining building block, located 40 km off-shore of Toulon, France, is referred as ORCA (Oscillation Research with Cosmics in the Abyss). Their construction has already started, in particular, ORCA is being deployed about 10 km west of the site of the ANTARES detector. Upon completion ORCA will consist of 120 flexible, 200 m high, detection units (DUs), each of which comprises 18 Digital Optical Modules (DOMs). A DOM is a pressure resistant, 17-inch diameter glass sphere containing a total of 31, 3", PMTs and their associated electronics. The vertical spacing between DOMs is 9 m and the DUs are separated on average by 23 m from each other on the seafloor. The main difference between ORCA and ARCA is the detector density: ARCA will consist of 230 flexible, 700 m height, DUs, 95 m distant from each other, each of them comprising 18 DOMs with a vertical distance of 36 m. Fig. 3.14 (b) shows a representation of KM3NeT, that is the same for both ORCA and ARCA since their main difference is the detector density. ORCA is denser than ARCA. The reason is that it is optimised for particle physics studies with atmospheric neutrinos in the few GeV range. ARCA instead, is optimised for high energy ($E_\nu > 1TeV$) astrophysical neutrino searches. The ORCA total instrumented volume is approximately 8 Mton [59]. Tab. 3.2 shows ORCA and ARCA direction resolution. Compared with ANTARES (Tab. 3.1) ARCA performs better, in fact ARCA will allow

high precision measurements. ORCA instead performs worse, especially at low energy: this is due in part to the kinematics of neutrino interactions which are an intrinsic limit in this low energy region and also because lower energy events produce less Cherenkov photons, so the reconstruction errors are bigger.

	Angular Resolution
KM3NeT/ORCA	
Tracks	$\sim 18^\circ$ at $E_\nu = 1$ GeV, $\sim 2^\circ$ at $E_\nu \sim 100$ GeV
Showers	$\sim 20^\circ$ at $E_\nu = 1$ GeV, $\sim 2^\circ$ at $E_\nu \sim 100$ GeV
KM3NeT/ARCA	
Tracks	$< 0.2^\circ$ at $E_\nu > 10$ TeV
Showers	$< 2^\circ$ at $E_\nu = 50$ TeV

Table 3.2: ORCA and ARCA direction resolution for track-like and shower-like events.

3.7.1 Digital Optical Module (DOM) and PMTs

The design of the DOM has several advantages over traditional optical modules using single large PMTs, as it houses three to four times the photo-cathode area in a single sphere and has an almost uniform angular coverage. As the photo-cathode is segmented, the identification of more than one photon arriving at the DOM can be done with high efficiency and purity. In addition, the directional information provides improved rejection of optical background [59]. The PMTs are arranged in 5 rings of 6 PMTs plus a single PMT at the bottom pointing vertically downwards. The PMTs are spaced at 60° in azimuth and successive rings are staggered by 30°. There are 19 PMTs in the lower hemisphere and 12 PMTs in the upper hemisphere. The PMTs are held in place by a 3D printed support. The photon collection efficiency is increased by 20–40% by a reflector ring around the face of each PMT. Each PMT has an individual low-power high-voltage base with integrated amplification and tuneable discrimination. The arrival time and the time-over-threshold (ToT) of each PMT, are recorded by an individual time-to-digital converter implemented in a FPGA already present inside od the DOM: this is the reason why they are called **Digital** Optical Modules, instead of only Optical Modules, as in the ANTARES case, because in this case the conversion analog-to-digital is done inside of the sphere, in ANTARES instead it was done in the LCM. The threshold is set at the level of 0.3 of

the mean single photon pulse height and the high voltage is set to provide an amplification of 3×10^6. In particular, the PMTs used by KM3NeT are 3-inches Hamamatsu; Fig. 3.16 (a) shows their measured quantum efficiency (QE), from it we can se that wavelength window at which the QE is higher is between 300-500 nm. The timing accuracy and the photon counting capability are the main parameters that determine the detector event reconstruction accuracy. The measurement of the arrival times of photons on the PMTs is crucial since it affects the accuracy of the event reconstruction. The charge estimate is based on the number of hit PMTs on each DOM and on the Time over Threshold (ToT) values of the PMT pulses. In particular, the arrival time and the time-over-threshold (ToT) of each PMT are recorded by an individual time-to-digital converter implemented in a FPGA. In normal operation, only ToT signals are digitised. The derived ToT distribution is peaked at 26.4 ns (which corresponds to 1 photoelectron), see Fig. 3.15.

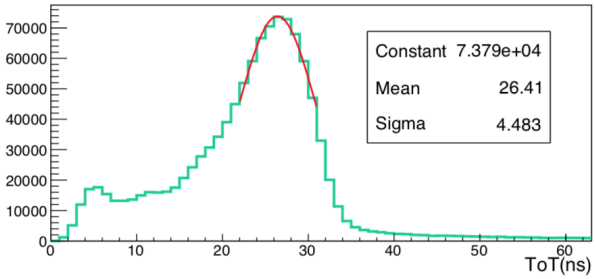

Figure 3.15: Typical ToT distribution. The curve shows the fit of peak whose value corresponds to 26.4 ns. Figure taken from [60].

The accuracy of this estimation affects the reconstructed energy resolution. Time characteristics of PMTs have been measured by detecting and analysing the so-called first photon hits, i.e. pulses detected in a window of 200 ns around the expected arrival time of the PMT signal. The distribution of arrival time of the first hits for a typical PMT is shown in Fig. 3.16 (b). The main peak of the distribution corresponds to the PMT transit time (TT) and the transit time spread (TTS) is defined as the FWHM of this peak whose distribution stays below 5 ns [60].
The optical module also contains three calibration sensors: 1) The LED nano-beacon, which illuminates the optical module(s) vertically above; 2) A compass and tilt-meter for orientation calibration; 3) An acoustic piezo sensor glued to the inner surface of the glass sphere for position calibration. Currently, 4 ORCA DUs have been deployed in the sea and are taking data. The ORCA data acquisition system, as well as its reconstructions and Par-

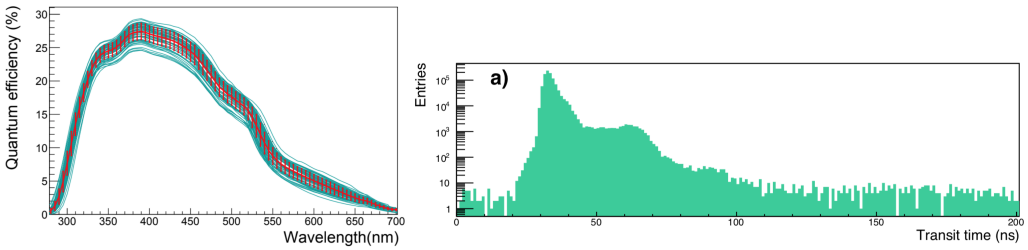

(a) (b)

Figure 3.16: (a) Measured QEs of the 3-inches, Hamamatru PMTs used in KM3NeT. (b) Measured arrival time of the first hit for the same PMTs. Both figures are taken from [60].

ticle Identification (PID) algorithms will be largely discussed in the next chapters.

3.8 Background in the Deep Sea

In the deep sea there are 3 sources of background:

1. Atmospheric muons, produced in the interactions of primary cosmic rays in the atmosphere. Muons are the most abundant charged particles arriving at sea level and the only ones able to penetrate deep underground. The reason relies on their small energy loss (only ∼2 GeV across the whole atmosphere), the relatively long lifetime, and the fairly small interaction cross-section. The flux of muons with energy >1 GeV at sea level is of the order of 200 particles/(m^2 s). They are only partially absorbed in the deep sea (see Fig 3.17), so they represent a dangerous background for neutrino telescopes, because they can be mis-reconstructed as muons coming from the neutrino signal. On the other side, since they are the most abundant signal, they can be used to calibrate the detectors and to check their expected response to charged particles.

2. ^{40}K, is by far the dominant of all radioactive isotopes present in natural seawater. With a half-time of about 1.277 Gyr, this isotope decays beta in two dominant modes which are above the threshold for Cherenkov light production. These decay channels are:

$$^{40}\mathrm{K} \rightarrow ^{40}\mathrm{Ca} + \mathrm{e}^- + \bar{\nu}_e \qquad (89.3\%)$$

$$^{40}\mathrm{K} + \mathrm{e}^- \rightarrow ^{40}\mathrm{Ar} + \gamma + \nu_e \qquad (10.7\%)$$

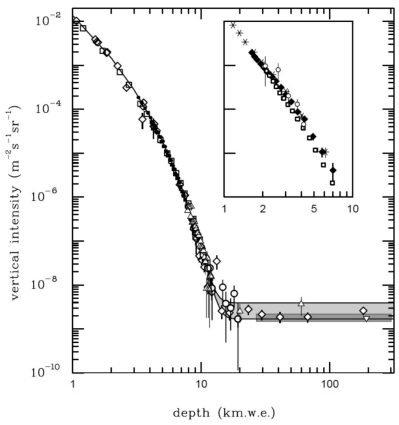

Figure 3.17: Vertical muon intensity versus depth. The quantity on the x-axis is the depth, expressed in km of water equivalent: 1 km.w.e. = 10^5 g cm^{-2} of standard rock. Figure taken from [47].

In the sea water, the ^{40}K activity is quite stable, within 0.1% [61]. Since the physics involved is well known, its contribution is easily simulated by Monte Carlo and it should be taken into account in reconstruction algorithms, as it is discussed in Chapter 4. Moreover, ^{40}K can be a useful tool to monitor the OM/DOM efficiency, since coincidences induced by the same ^{40}K decay process contribute to hit pairs on adjacent OMs with small time differences Δt. The monitoring of the ANTARES PMTs has been performed by using this method, and it is shown in Fig. 3.18.

3. Bioluminescence, mainly due to steady glow of bacteria and flashes produced by animals. These can give rise to an optical background which occasionally can reach a level of several orders of magnitude larger than that due to ^{40}K.

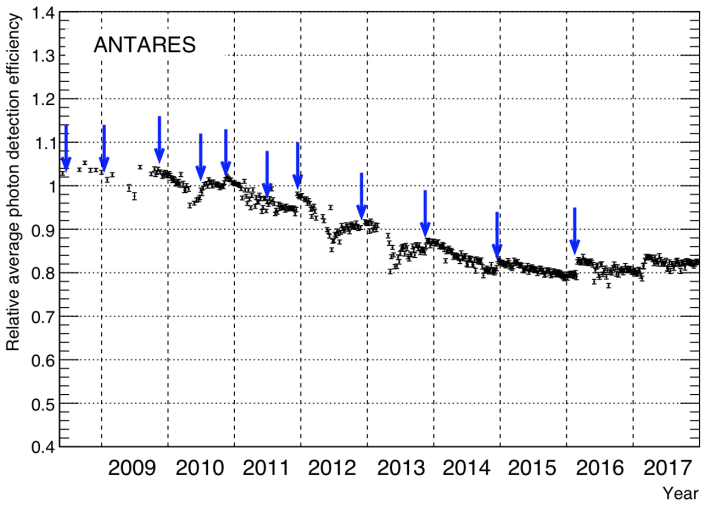

Figure 3.18: Relative ANTARES OM efficiency averaged over the whole detector as a function of time. The blue arrows indicate the periods in which high voltage tuning of the PMTs has been performed, while error bars indicate the statistical error σ_{mean} on the mean efficiency. Figure taken from [62].

Chapter 4

KM3NeT Monitoring Channel Analysis

In this chapter the work I have done to analyze real data coming from ORCA and ARCA is presented. Though not strictly correlated with the main subject of my thesis, this service task allowed me both to better understand the KM3NeT Data Acquisition System (DAQ) and to provide relevant tools for a correct on-line data taking.
In the first part of the chapter, the KM3NeT data acquisition system is described. This is useful to understand the work I have done, which is explained in the second part of the chapter, together with the analyses I made with real data coming both from ORCA and ARCA.

4.1 UDP Packets

The communication between the Detector and the Shore Station exploits the Ethernet II standard as data link layer, i.e. the unit element exchanged in the on off shore segment is an Ethernet packet, which embeds the Ethernet frame. This packet is composed of a network layer (IPv4) and a transport layer (UDP) [63]. In particular, as shown in Fig. 4.1, there is:

1. a IPv4 header carrying the IP addresses of the source (i.e. CLBs) and the destination of the packet,

2. the UDP header (specifying the source and destination ports),

3. the UDP payload which is the actual place where the KM3NeT data are stored.

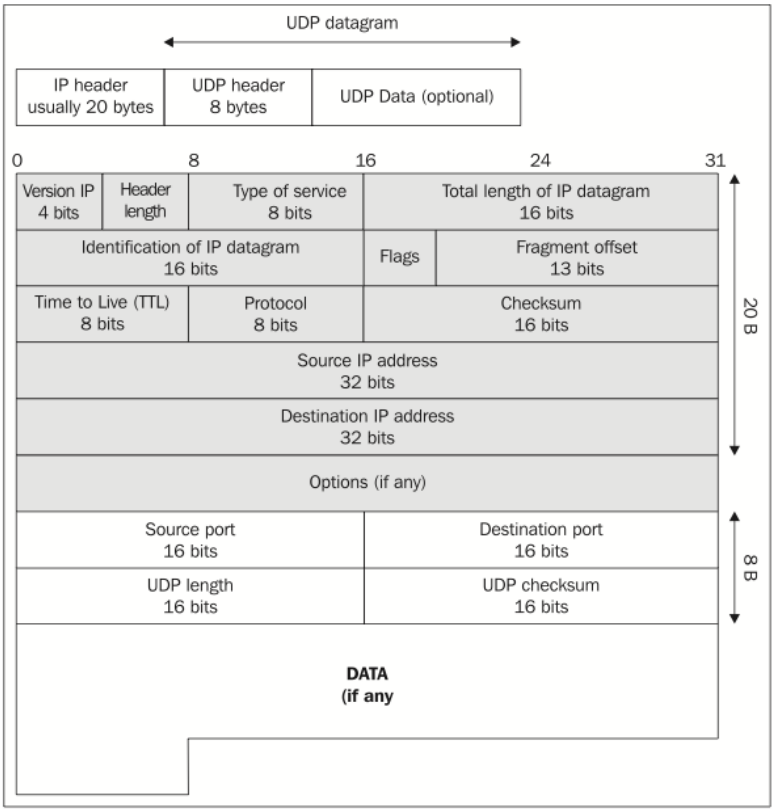

Figure 4.1: Scheme of the Ethernet payload: the IP and UDP headers and the KM3NeT data payload.

Hence, to summarize, **the communication between the Detector and the Shore Station (and vice-versa) is done via UDP packets**. Each CLB has a preconfigured destination IP address onshore where to address the measured data. Such an IP address is stored in the IPMUX memory and it is shared among the data transmission [63]. Different destination ports are used to separate the optical and the acoustic data (see Section 4.5). The destination IP address, as well as the source one (i.e. the CLB IP address), is stored in the IP header of the packets. The port information is stored in the header of all the UDP datagram (see Fig. 4.1).

4.2 Timeslices and Frames

KM3NeT data are thought as a continuous stream of packets sent at specific time intervals of a certain fixed duration ΔTS, called timeslices (TSs) [64]. Data occurring within the same TS are supposed to be uncorrelated to

those belonging to other timeslices, which means that it is unlikely to find a neutrino event split in two consecutive TS. This is much more true if ΔTS $>> \Delta\nu$, where $\Delta\nu \sim 3\,\mu s$ is the duration of a muon event in 1 km3 size telescope. Hence the chosen time interval of a timeslice in KM3NeT is **100 ms**.
During this time interval, each DOM of the Detector collects data and sends them to shore as a **frame**. Generally, when referring to one timeslice of data it is intended all the frames from all the DOMs corresponding to that timeslice. The frame composition is performed onboard of the CLBs.

4.3 Data Channels

In KM3NeT there are three main data streams [65]:

- **Fast Acquisition Data Stream (FDS)**: it includes three channels
  - **Optical Data (or TDC Channel)**: (from offshore to shore) it is composed of the digitized signals (the hits) produced by all the 3" PMTs of the DOMs. The optical information provides the observables needed for the principal Physics and Astrophysics measures performed with the KM3NeT telescope. The basic information of the optical hit is its time of occurrence and the time-over-threshold (ToT).
  - **Acoustic Data (or AES Channel)**: (from offshore to shore) it is composed of the digitized signals of the acoustic sensors (piezoelectric sensor, on the DOMs, and hydrophones on the string-bases and Calibration Units). The acoustic information is used to retrieve the position of each element of the strings (DOMs and string-base).
  - **Monitoring Channel**: (from offshore to shore) it is composed of the information retrieved onboard of each CLB from the AHRS (tiltmeter+compass) and SHT21 (temperature and relative humidity) instruments, PMTs rates, etc [66].

  The fast acquisition data streams originates in the CLBs of the offshore DOMs and are sent to the Shore Station. Each CLB sends to shore the TDC, AES and Monitor data which are organised in three separated bunches of Ethernet-UDP packets (see Fig. 4.2). **The Monitoring channel has only 1 UDP packet per frame (i.e. per time slice). For the TDC and AES channels, due to the amount of**

data, one single frame is fragmented in different UDP packets, which are re-aggregated on shore; the number of UDP packets depends on the size of the collected information.

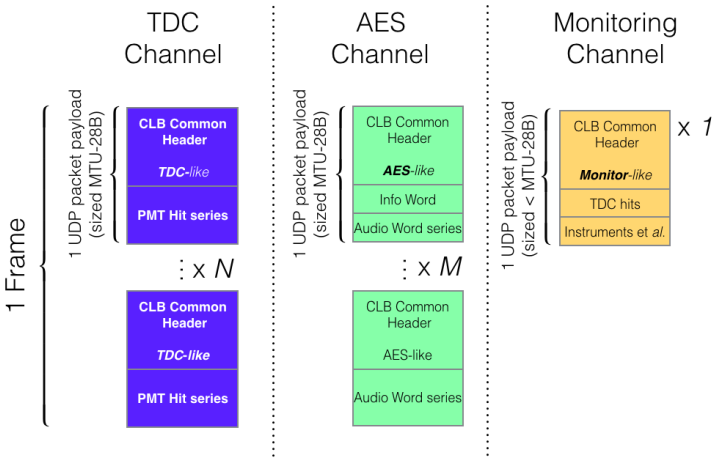

Figure 4.2: The three flavour of fast acquisition data streams. Note that the Monitoring channel has only 1 UDP packet per frame (i.e. per time slice). For the TDC and AES channels, the number of UDP packets depends on the size of the collected information. Generally the UDP packet numbers are different for TDC and AES channels.

- **Slow Control Stream**: (bidirectional) commands to the detector and possible feedbacks to the shore-station.
- **Instruments Information Stream**: produced by the DOMs.

Since the optical information is directly related to the main scientific goals of the KM3NeT telescope, it drives the organization of the detector data acquisition [67]. The optical stream represent always the largest throughput from the detector. We can estimate it by focusing our attention to the data recorded by the PMTs. The intensity of the optical background is relevant (see Sec. 3.8 for a description of the optical background in deep sea). In the following we refer to the optical continuous background rate on a PMT as the summation of the rates from ^{40}K decays and from bioluminescence. The ^{40}K contribution is constant and depends essentially on the PMT surface and threshold settings. For example on a 10" PMT (such as for ANTARES or NEMO) with a threshold set at 0.25 photon electron (p.e.) the ^{40}K background rate is within the range 45-50 kHz. The bursts of bioluminescence could enhance the measured hit rate up to 10 MHz with the same 10"

PMT settings. The quantity of the bioluminescence nuisance is related to the depth of the submarine site which hosts the telescope. The deeper is the site, the less is the contribution of bioluminescence. In the case of one KM3NeT 3" PMTs, we can obtain the related optical background rate by simply considering a conversion factor given by the ratio of the square of the PMT radii:

$$f = \frac{R^2_{3"}}{R^2_{10"}} = 0.1 \tag{4.1}$$

This imply that for a 3" PMT the ^{40}K background continuous rate is $\sim$ 5 kHz. In order to set a realistic lower bound to the bioluminescence burst contribution we can refer to the measurement performed in the Capo Passero site (at 3500 m below the sea level) with the NEMO Phase 2 Tower. After more than one year of data taking, it was measured the average single rate per each one of the 10" PMTs within the range of 48-52 kHz, confirming the general assumption of quasi-pure ^{40}K contribution.
The French site of Toulon, which is shallower than that of Capo Passero, is showing higher rates due to an enhanced bioluminescence activity. Recent measurements, performed with a test DOM on the ANTARES Instrumented line, show an average rate of 9.5 kHz for each of the 31 3" PMTs of the DOM. Such rates are higher than what is measured in Capo Passero. In order to sketch the complete scenario of estimations to be kept as reference we mark as minimum rate the value of a continous 6 kHz per 3" PMTs, 10 kHz as conservative rate and finally 15 kHz as maximum rate, used to set an upper limit (far from being realistic) used as maximum tolerance for the optical TriDAS (Trigger and Data Acquisition System).
In any case, according to the all data to shore philosophy, a large throughput (up to several hundreds of gigabit per seconds) is sent from off shore to on shore, through the electro-optical cable. In order to reject as much optical background as possible, a continuous online data filtering (trigger algorithms) must be organized so to act on coherent groups of data [67]. Few categories of transient astrophysical phenomena such as Gamma Ray Bursts (GRB) or SuperNova explosions can be triggered by some external alerting system connected to the detector. More generally, the neutrino telescope doesn't benefit of any specific time indication for starting the data acquisition, which must always be running.
All the DOMs in the Detector are synchronized with a precision better than 1 ns (see Sec. 4.5). The command telling when all the CLB must start the time-slicing is broadcasted from the shore station to all the DOMs. Such starting time is known with a precision better than 1 ns [64]. In this case, the framing is performed coherently by each CLB. With "coherently" we

mean that the time-alignment within 1 ns of the frames from all the DOMs of the telescope is a practically perfect synchronization (with respect to the duration of a time-slice which is of the order of 100 ms). This is shown in Fig. 4.3, where each colored block is the frame delivered by every DOM referring to the same timeslice.

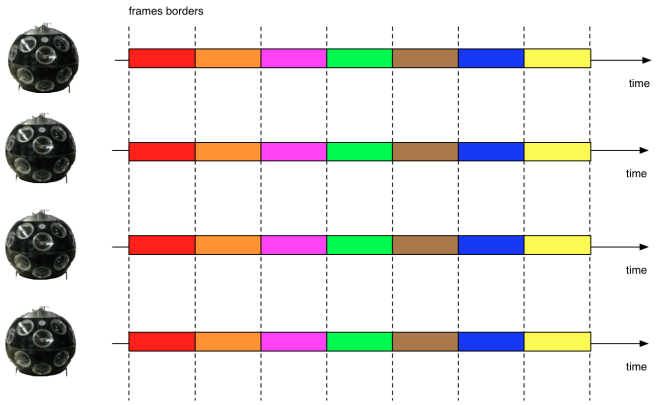

Figure 4.3: The framing on each DOM in the calibrated scenario. All the frames are coherent within a precision better than 1 ns.

Each frame which is sent to shore, via UDP packet, will be accompanied by the absolute timestamp of the beginning of the frame. For the TDC and AES channels, each frame will be sent to shore fragmented into multiple UDP datagrams. Inside each datagram with a fragment of one given frame, the same start-time info of that very frame is repeated, and each UDP packet has its own index so that, when they arrive on shore, they can be re-organized in a single frame by the DataQueue (see Sec. 4.5).
At this point, an overview of the KM3NeT Data Acquisition can clarify and complete some points mentioned above.

4.4 Data Acquisition Stages

The concept of timeslice characterizes the whole data acquisition system, which is composed of four parts [65]:

1. data aggregation, providing coherent bunches of data, grouped according to the same timeslice. For a DOM, the gathered data corresponding to one timeslice is called frame. Generally, when referring to one timeslice of data it refers to all the frames from all the DOMs corresponding to that very timeslice. The frame composition is performed onboard of the CLBs.

2. data routing, addressing all the data occurred in one TS from all the detector to one specific server of the computing facility that will analyze the them. This task is performed by the DataQueue processes.

3. data processing, the correction of the acquired data by the calibration parameters, the distribution of physical and DAQ information to monitoring terminals, the application of the trigger algorithms to the data flow (task assigned to the DataFilter processes) and the consequent event building with the data survived after the selections (task assigned to the Data Writer process). The optical throughput should be suppressed by almost 4 orders of magnitude (see documentation from General references and Trigger studies) with respect to the background contamination. This challenging trigger and data acquisition system (also called TriDAS) requires special fast data filtering algorithms, efficient data distribution and an adequate computing infrastructure.

4. data storing, saving the recorded data into persistent media, eventually organized according to some database structure.

4.5 KM3NeT Data Acquisition System

The KM3NeT Data Acquisition System (DAQ) is summarised in Fig. 4.4. Following the direction from offshore to shore [63]:

- **White Rabbit Switch Infrastructure**: it is used to achieve the sub-nanosecond time synchronisation among the DOMs.

- **DataQueues**: multiple processes/servers which receive the UDP datagrams containing the optical and acoustic data, reconstruct the frames and transfer them to the DataFilters.

- **DataFilters**: multiple processes/servers which apply the trigger algorithms to the incoming (optical and acoustic) data. The optical DataFilters pass the selected events to the DataWriter; the acoustic DataFilters send their output to the DataBaseWriter, which is part of the Control Unit.

- **DataWriter**: single process which collects the selected events from the optical DataFilters and write them to a ROOT file on the local storage.

- **Control Unit**: the collection of services for operating the offshore detector and the onshore Trigger and Data Acquisition System (**TriDAS**) which is composed of DataQueues, DataFilters, DataWriters etc.

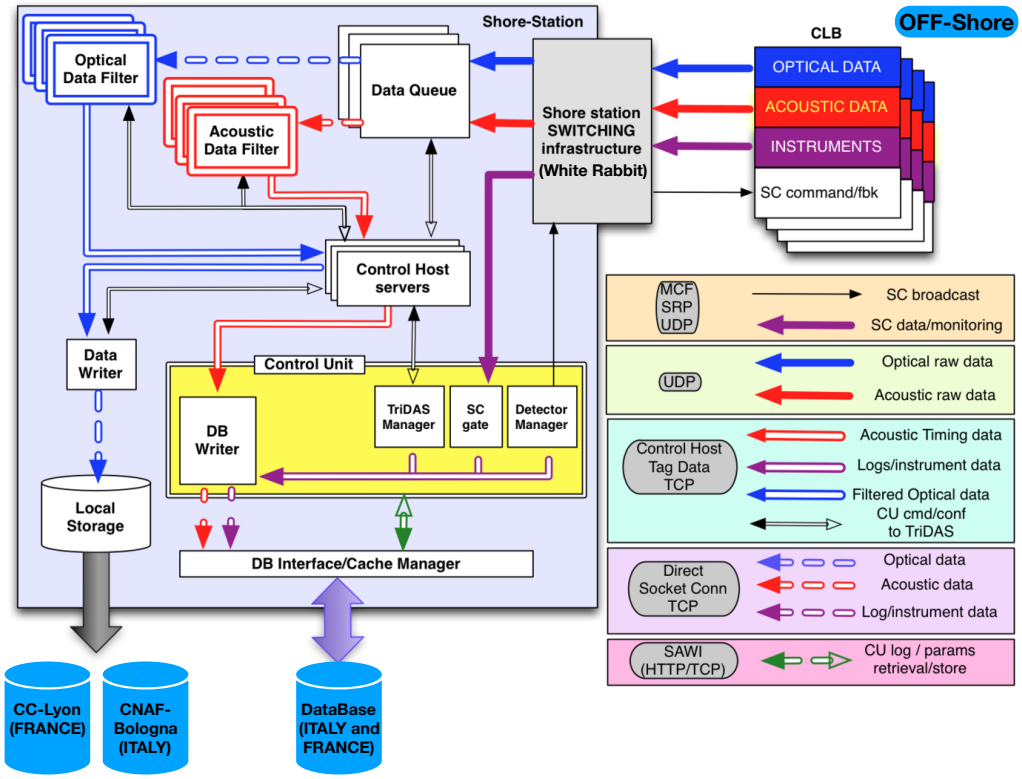

Figure 4.4: KM3NeT DAQ Design.

Each of these points can be described in more detail.

4.5.1 White Rabbit Switch

From the DAQ perspective, the shore station front-end to the submarine detector is represented by the White Rabbit switching infrastructure which is an extension of Ethernet that provides sub-nanosecond synchronisation of timing and data transfer. White Rabbit allows to timestamp measured data with precision and lets the trigger data taking in large installations while at the same time using the same network to transmit data. Every single DOM has one wavelength to communicate with the onshore station, instead, the communication from the onshore station to the DOMs uses just one wavelength which reaches all the DOMs. To give a more quantitative idea of the wavelengths needed we can consider that for the full ORCA the communication between shore station and DOMs passes through 5 Junction Boxes (JB, see Fig. 4.5), each JB has 8 connectors: each connector is able to power 4 DUs in series and 5 of these 8 connectors are dedicated for the

series of 4 DUs. Hence, **for each JB**, we have: 5 (connectors) × 4 (DUs in series per connector) × 18 (DOMs per DU), for a total of **360** wavelengths which are sent to shore and controlled by the White Rabbit System.

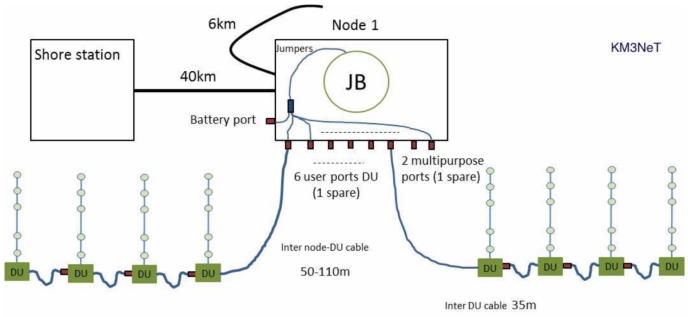

Figure 4.5: Scheme of the KM3NeT/ORCA Junction Box. Figure taken from [59].

The optical signals arriving from offshore through the fibres of the main electro-optical cable are demultiplexed in several independent channels, one for each DOM. By means of a stacked switching infrastructure, the DOMs throughputs are addressed to the first layers of the DAQ system. It is at this point that optical and acoustic data streams are separated from the Slow Control data flow. The first two are addressed to the DataQueue servers, the second is routed to the Control Unit.

4.5.2 DataQueue, DataFilters and DataWriter

Each DataQueue process is interfaced to a fixed number of CLBs. The DataQueues receive the optical and acoustic frames through UDP packets and retransmit them to the proper DataFilters. The online selection of the optical data is performed only after having reconstructed a full timeslice. It means that all the present DataQueues must transmit to the very same DataFilter all the frames corresponding to the same timeslice. In other terms, each Optical DataFilter applies its trigger algorithms to a particular data-set obtained from all the detection elements of the telescope, but corresponding to a limited time interval.
The selected optical data are addressed to the single DataWriter process which will write them into ROOT-files in the local storage. The produced post-trigger ROOT-files have a maximum size of some GB. During the same run more post-trigger files can be dumped. Once a file is completed it can be copied from the local storage to the final persistence storaging archive.

4.6 Monitoring Channel

After an overview ok the KM3NeT DAQ we can now focus on the work I have done with the monitoring channel. As stated above, the Monitoring Channel is part of the Fast Data Acquisition and, differently from the optical and acoustic channels, it uses one single UDP packet for each frame (instead of having a fragmented frame). Fig. 4.6 shows all the information sent by the monitoring channel: it refers to optical data, and, as each UDP packet, it contains the RUN number, the Timeslice start in UTC time, the DOM Identifier, **if** the High Rate Veto (HRV) has been activated or not, the PMTs rates for that frame: it is important to specify that the HRV is set at 15 kHz and when it is activated, this is the maximum rate saved in the optical channel, instead, the monitoring channel saves the real values of the rates when they are above the HRV, hence it can be used to monitor also the bioluminescence.

Section	Offset (bytes)	Lenght	Type	Name	Description
Header	0	4	CHAR[4]	DTYPE	DataType = "TMCH"
	4	4	U32	RUNNO	Run number
	8	4	U32	UDPSEQ	UDP Sequence number
	12	8	2xU32	TSSTART	Timeslice start UTC time
	20	4	U32	DOMID	DOM Identifier
	24	4	BITMAP	STATUS I	Bits 0..30: Veto activated, channels 1 to 31. Bit 31: Time valid
	28	4	BITMAP	STATUS II	Bits 0..30: FIFO Full channels 1 to 31. Bit 31:'0' **
	32	4	BITMAP	STATUS III	Not yet defined (bits 0..31 ='0') **
	36	4	BITMAP	STATUS IV	Not yet defined (bits 0..31 ='0') **
TDC Hits	40	124	U32[31]	HITCNT	TDC Hit counter values
	164	4	BITMAP	HRVBMP	High-Rate veto activated: Bit 0..30: Channels 1 to 31

Software	168	4	BITMAP	FLAGS	Content flags:
					`Bit 0 : AHRS data valid`
					`Bit 3-1: Structure version:`
					`* 000 - Version 1`
					`* 001 - Version 2`
					`* 010 - Unused!`
					`* 011 - Version 3`

	172	4	FLOAT	YAW	AHRS Yaw *
	176	4	FLOAT	PITCH	AHRS Pitch *
	180	4	FLOAT	ROLL	AHRS Roll *
	184	4	FLOAT	AX	Accelerometer X, in G
	188	4	FLOAT	AY	Accelerometer Y, in G
	192	4	FLOAT	AZ	Accelerometer Z, in G
	196	4	FLOAT	GX	Gyro rotation X, in deg/sec *
	200	4	FLOAT	GY	Gyro rotation Y, in deg/sec *
	204	4	FLOAT	GZ	Gyro rotation Z, in deg/sec *
	208	4	FLOAT	HX	Compass X, in Gauss
	212	4	FLOAT	HY	Compass Y, in Gauss
	216	4	FLOAT	HZ	Compass Z, in Gauss
	220	2	I16	TEMP	Temperature (1/100th of a degree)
	222	2	U16	HUMID	Humidity (1/100th RH)
	224	4	BITMAP	TDCFULL	Last frame TDC full flags: Bit 0..30: Channel 1 to 31. Bit 31 : Timeslice start FIFO
	228	4	BITMAP	AESFULL	Last frame AES full: Bit 0: AES FIFO. Bit 31: Timeslice start FIFO
	232	4	U32	FLUSHC	Number of flushes during current frame
	236	4	U32	TSLICEDUR	Timeslice duration in microseconds [v2]
	238	2	U16	TDC_ST_COMMIT	State-machine TDC supertime fifo commit size [v3]
	240	2	U16	AES_ST_COMMIT	State-machine AES supertime fifo commit size [v3]

Figure 4.6: Summary information of the Monitoring Channel.

As seen in Fig. 4.6, other information contained in the monitoring channel are the yaw, pitch and roll which monitor the DOMs orientation (in the 3 dimensions), the compasses, the temperature and humidity, the TS duration and other variables like "State-machine TDC, AES supertime fifo" which are related to the time synchronization of the frames. Hence this channel can really be used to monitor not only the PMT rates, but also their time synchronization and the DOMs orientation.
In this context I have developed two codes in python: **udpAnalyzer.py** and **udpRates.py** which analyse the DOMs time synchronization and the PMTs rates respectively.

4.6.1 udpAnalyser.py

I developed this code to make several time checks among UDP packets. In particular, it checks, for each DOM:

- if there are some UDP packets missing,
- the consistency of the time difference between consecutive udp packets from the same DOM (100 ms),
- the consistency between the timestamp of each udp packet and the machine time in which the code is running ($<$ 1 minute).
- the correlation between a time de-synchronization and some of the FIFO variables present in the channel

Output: if an error occurs, an error message is printed on the screen and a counting variable is incremented (for each type of error). These counting variables are saved in a .csv file as summary information for each run. This file is then uploaded to the KM3NeT database, allowing to perform an analysis, in parallel of the optical channel one, that can be used to define the quality of a run, i.e. if it is a good or bad run for physics analyses.

4.6.2 udpRates.py

I developed this code check the rate of each PMT of each DOM. In particular, for each PMT, it saves the following values:

- The lowest rate during the run,
- The highest rate during the run: this is useful because due to HRV (High Rate Veto) this variable is not accessible from the offline data,

- The mean PMT rate of the run,
- The mean DOM rate of the run,

Output: Also in this case, these variables are saved in a .csv file which is uploaded to the KM3NeT database.

4.7 ORCA & ARCA Data quality

Both udpAnalyser and udpRates have been run on ORCA and ARCA at different period of times. Hence some of the plots presented here may refer for example to ORCA with only 1 DU, or more DUs (but this will be explicitly written in each plot), this is because ORCA deployment has start during my PhD so there have been periods with different numbers of DUs. Up to now, there are **4 DUs** operating for ORCA and **1 DU** operating for ARCA. Both the codes are continuously running on ORCA and ARCA via tmux sessions. To better understand the correlation between PMT identification numbers and their positions in the DOM, which can be useful to understand some of the plots shown in this section, see Fig. 4.7.

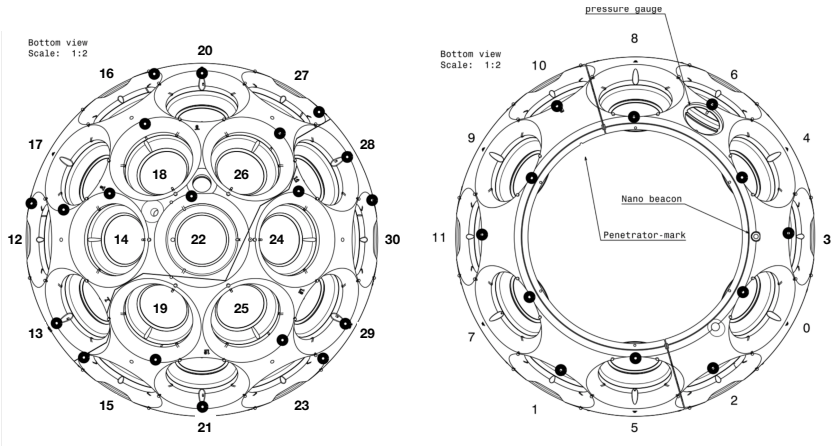

Figure 4.7: PMTs identification numbers correlated with their positions in the DOM.

Fig. 4.8 shows the DOMs mean rates for ORCA-DU1 (a), for 2 weeks of data taking in April 2019, and ARCA-DU1 (b) for 5 days of data taking in February 2019.
As we can see from the ORCA plot, there is an evident period of higher bioluminescence. We can highlight it if we look at the mean PMTs rates per

run (Fig. 4.9). In this case we can see that for ARCA the PMT rates have a mean value of 6.5 kHz, but since the analyzed data cover only 5 days we are not able to se if there are bioluminescence peaks. Instead, for ORCA (Fig. 4.9 (a)), we can see that for the period with low bioluminescence the mean PMT rates are $\sim$ 9.5 kHz. After the deployment of other 4 DUs for ORCA (in which we lost the communication with DU1), udpAnalyser and udpRates are constantly running on ORCA since 15th of July 2019. This has allowed me to monitor the data for a period of 2 months (up to today which is 15th of September 2019). If we look at PMTs mean rates, Fig. 4.10 we can notice different things:

- there are periods with high bioluminescence, and these are seen by all the 4 DUs,
- in periods with low bioluminescence, the mean PMT rates are $\sim$ 9.5-10 kHz, coherent with fig. 4.9 (a),
- DU3 has higher mean rate values with respect to the other DUs, and this seems to be something indipendent from bioluminescence, since it is seems to be a constant shift.

To figure out what is happening with DU3 we can have a look at the DOMs mean rates to see if there is a particular DOM which has higher rates. This is shown in Fig. 4.11: it is evident that DOM9 has very high rates with respect to the other DOMs. And this is the reason why we see an higher mean PMT rate for DU3 in Fig. 4.10.
We can investigate the issue even further by plotting the PMTs mean rates, but this time focusing on particular PMTs. For brevity, I report the result which is shown in Fig. 4.12: we can clearly see that PMT 21 (see Fig. 4.7 for its position in the DOMs) on DOM 9 has a very high rate. Its behaviour is under investigation.
If we focus instead on a DU which doesn't have this issue, as could be for DU4, we can see from Fig. 4.13 that we have some periods of bioluminescence, as already seen from Fig. 4.10, but in this case we can notice that the bioluminescence seems to **not** depend too much on the depth, in the sense that, when there is bioluminescence, all the DOMs of the DU have higher rates. This could be due because ORCA's DUs are 200 m height, instead for ARCA they are 700 m so in that case we could have a depth dependence.
From Fig. 4.13 we can also notice one run with higher rates for all DOMs: this is a **calibration run**, in particular a nanobeacon calibration for DU4: in this case all the beacons on one string are activated simultaneously. The beacons are located in the upper DOMs hemisphere (see Fig. 4.7), in particular near

to PMT 3 and 4. To make sure that the light from different beacons can not be confused the beacons are flashed one after the other with a given time delay between them. The bottom floor flashes first, so we do not expect to see more light in the PMTs located in the lower DOM 1 hemisphere, then the second floor, etc. In this case it could be interesting to see, for that run, the distribution of PMTs mean rates in function of their position. This is shown in Fig. 4.14. From the plot we can conclude, by taking into account that PMTs from **0** to **11** are in the upper DOM hemisphere and the others in the lower hemisphere, that:

- we have higher rates for PMTs > 12 (i.e. lower hemisphere) and this is consistent with the fact that the light is coming from the beacon located in the DOM below,
- PMTs > 12 in DOM 1 have rates consistent with ^{40}K since they are not too much affected by the light coming from the beacon located in the upper hemisphere of DOM 1,
- PMT 3-4, which are located near to the nanobeacon, are affected from its light, so they have higher rates with respect to the other PMTs in the upper hemisphere.

Finally, with the tools I have developed, we are able to make more other plots, like PMTs highest rates, which is not accessible from the optical offline data due to the HRV and it is clearly related to the bioluminescence (see Fig. 4.15), PMTs lowest rates, time synchronization errors distribution, etc. For brevity I reported here only a subset of those plots.
All the plots presented here and, more in general, made with the information coming from the monitoring channel are in agreement and, in some things, complementary to the optical channel data so they can be used as a cross-check and to define the quality of runs.
Now that we have dealt with the KM3NeT data taking we can make a step forward and focus on the reconstruction algorithms. In particular on shower reconstruction which has been one of the main topics of my thesis.

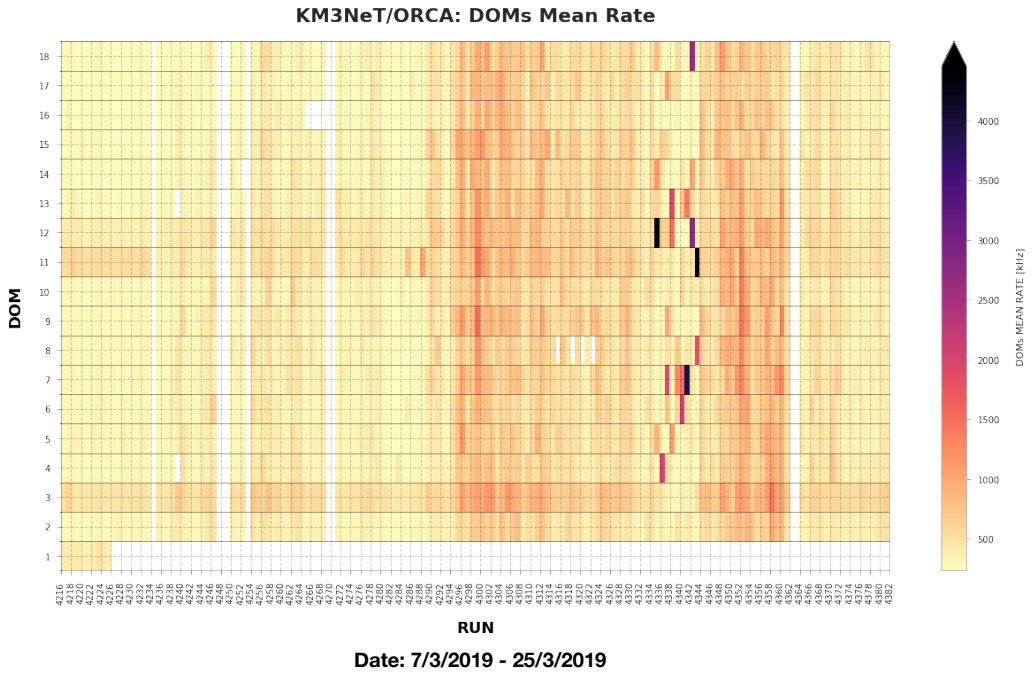

(a)

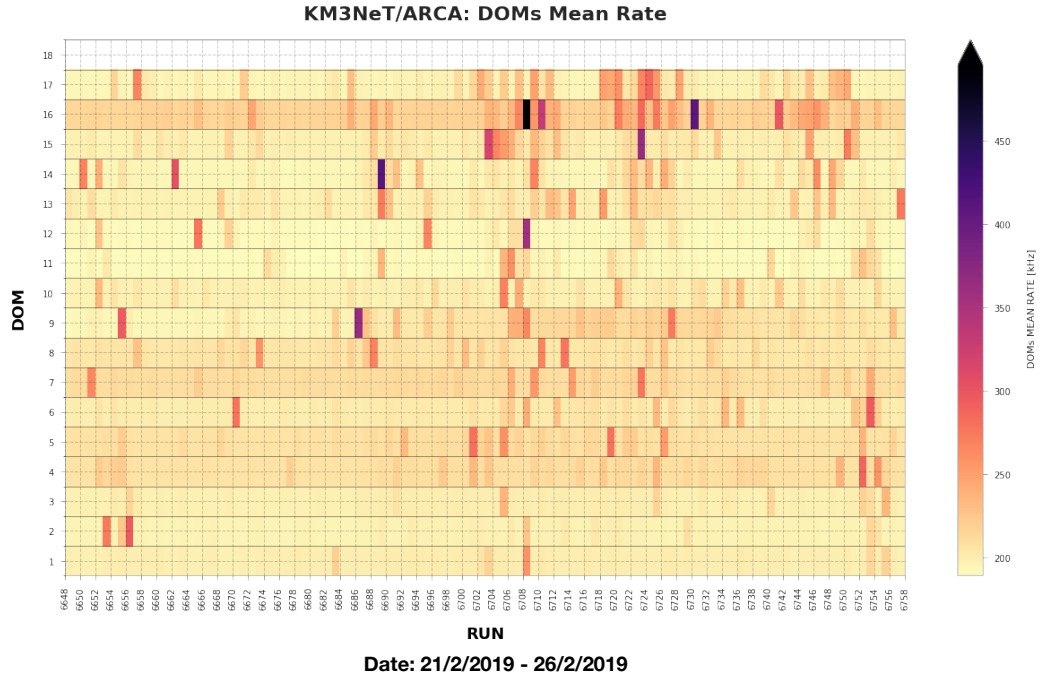

(b)

Figure 4.8: KM3NeT/ORCA-DU1 & ARCA Mean DOMs Rates. ORCA data refer to 2 weeks of data taking in April 2019, ARCA data to 5 days of data taking in February 2019.

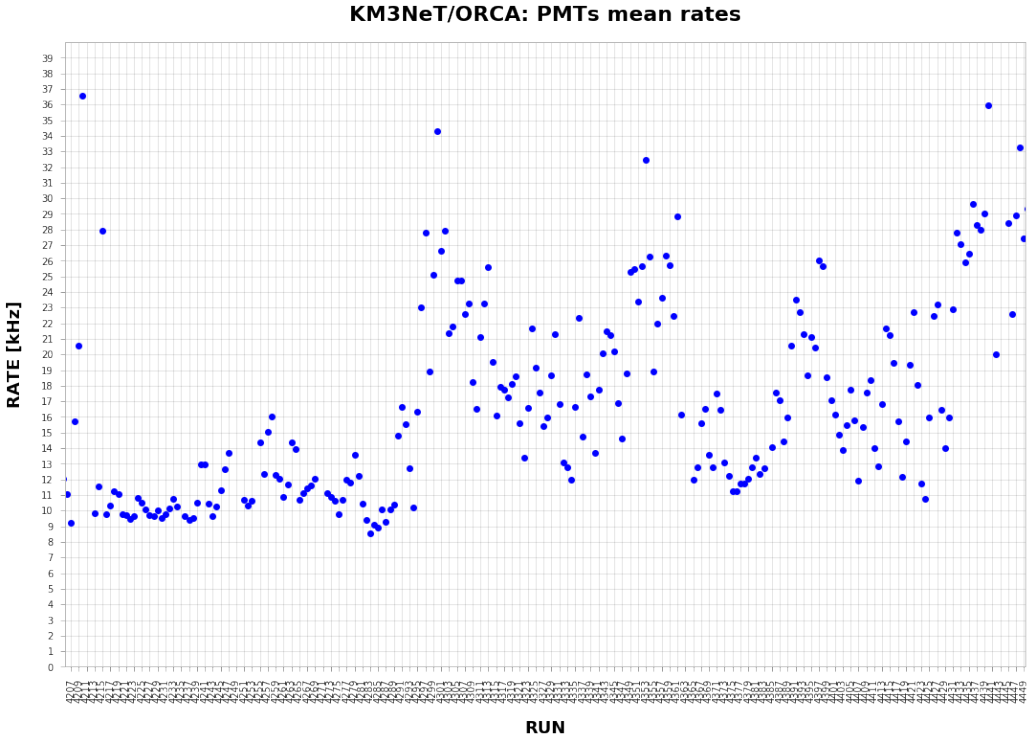

(a)

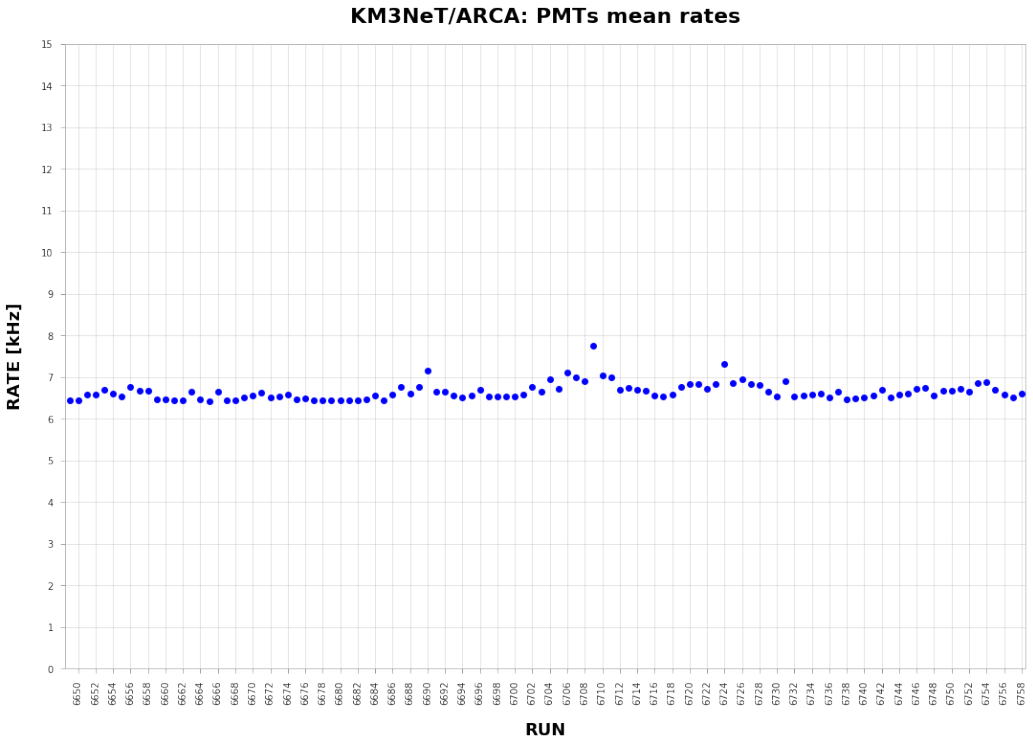

(b)

Figure 4.9: KM3NeT/ORCA & ARCA Mean DOMs Rates.

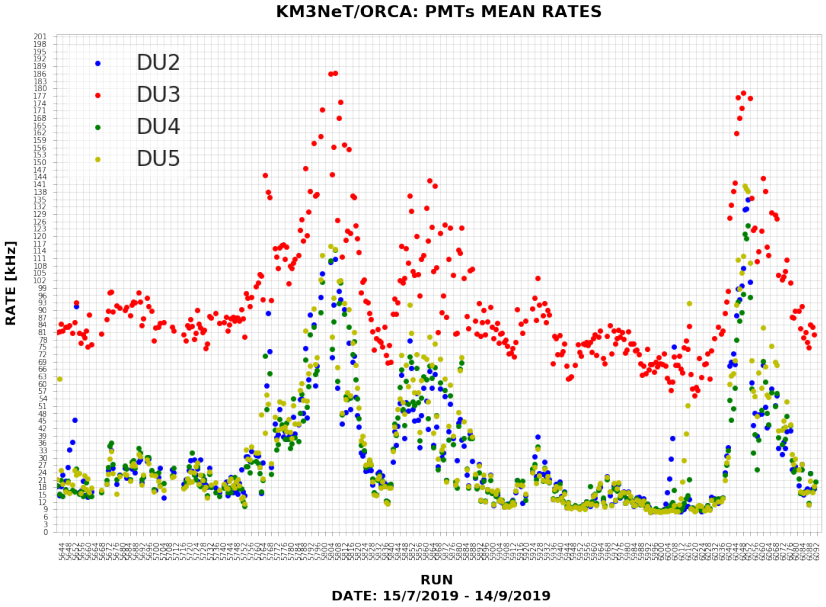

Figure 4.10: ORCA PMTs mean rates. This plot refers to ORCA with 4 DUs (namely DU2-3-4-5).

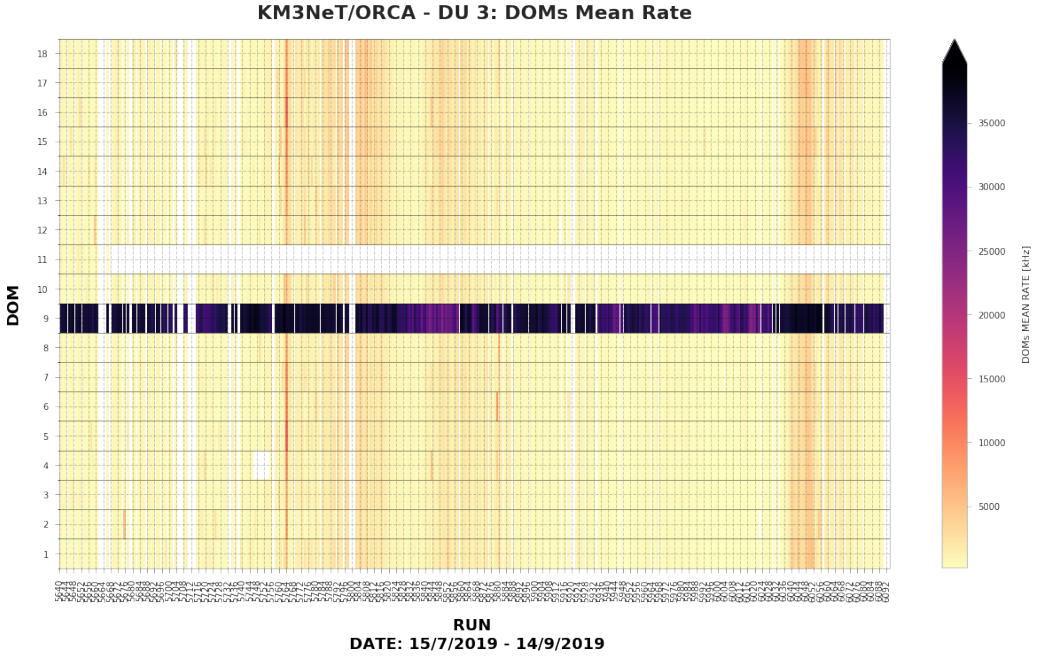

Figure 4.11: ORCA-DU3 DOMs Mean rates.

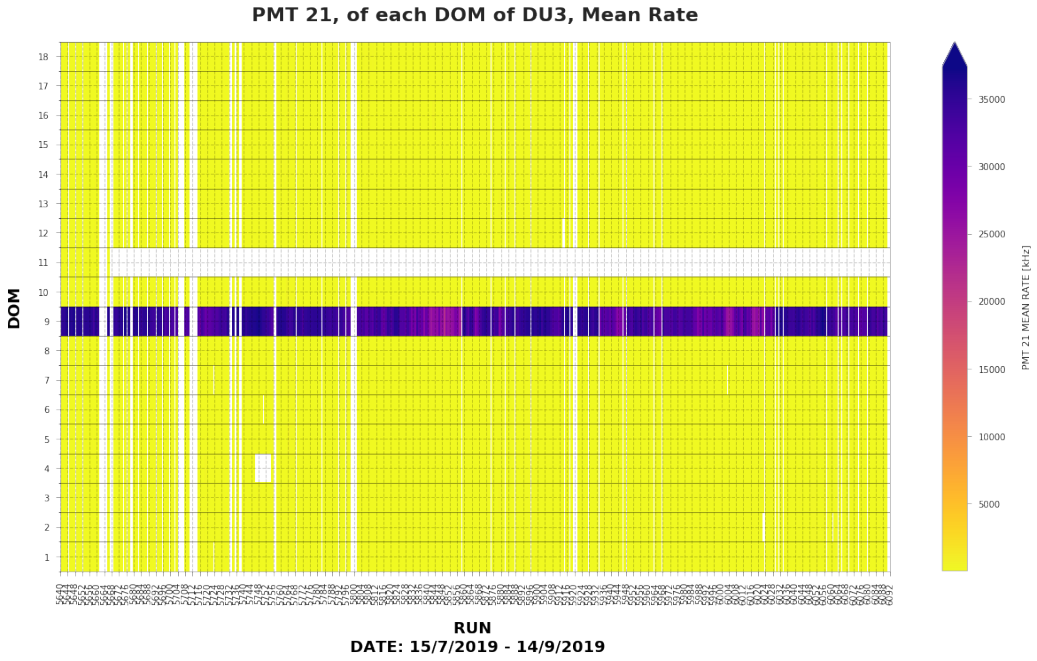

Figure 4.12: PMT 21 mean rates of all DOMs of DU3.

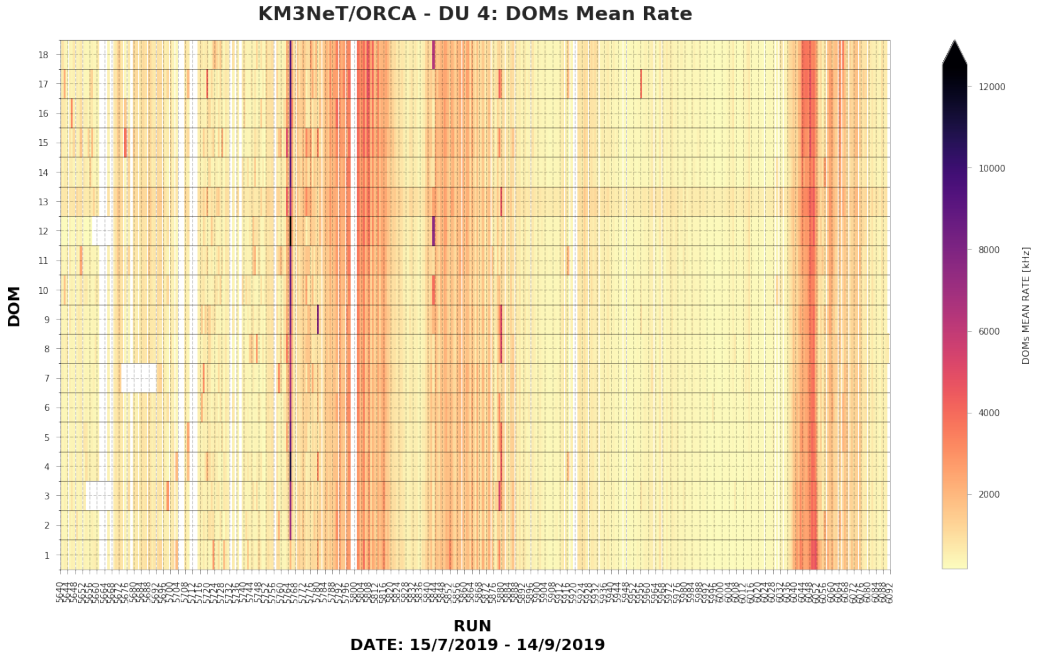

Figure 4.13: ORCA-DU4 DOMs Mean rates.

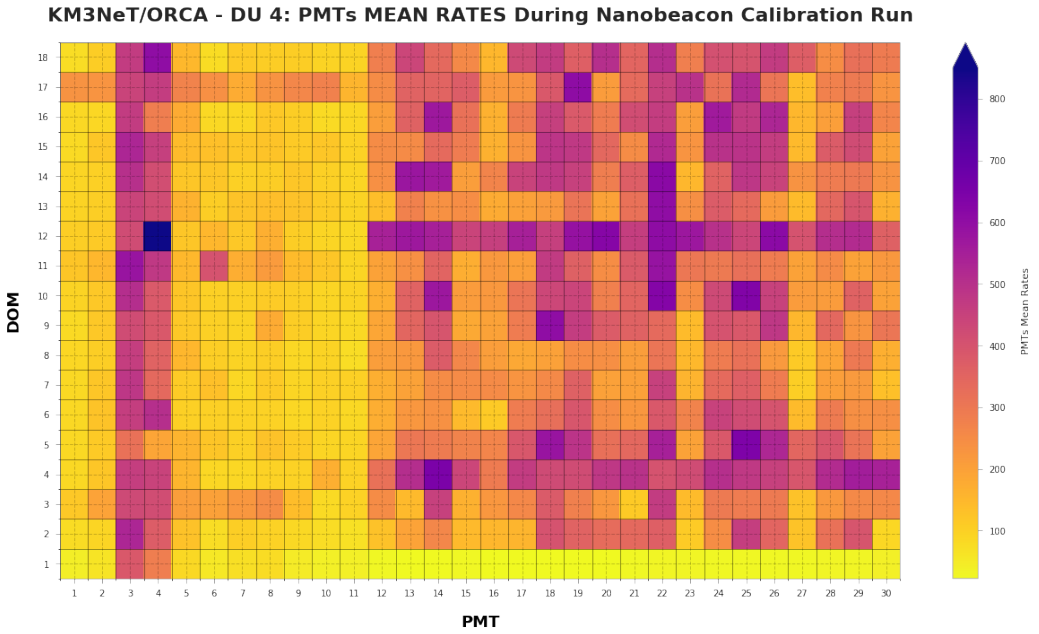

Figure 4.14: ORCA-DU4 Mean PMTs rates during a Nanobeacon Calibration Run. PMTs from 0 to 11 are located in the upper DOMs hemisphere.

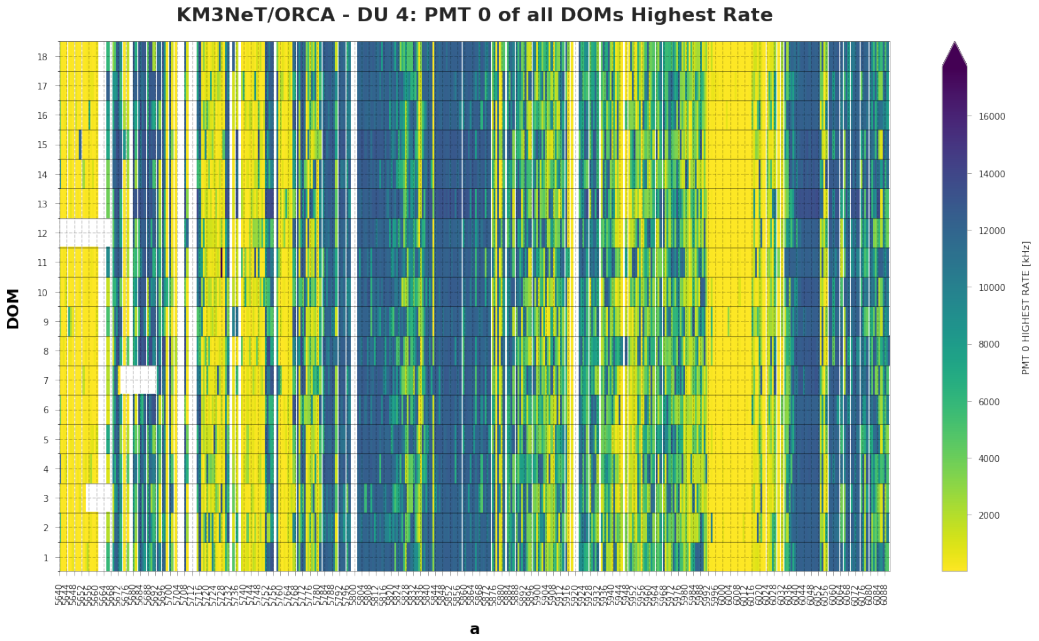

Figure 4.15: ORCA - DU 4: PMT 0 (in the upper DOMs hemisphere) highest rates.

Chapter 5

Shower Reconstruction in KM3NeT/ORCA

This chapter describes the shower reconstruction algorithm I developed for KM3NeT/ORCA and its performances. Actually, a previous shower reconstruction has been developed and used for ORCA that will be here referred as "Standard Reconstruction" (see Ref. [68]). Even if very well performing, it has been developed in an old framework, called *SeaTray* [69], that is the official framework for data processing and event reconstruction in ANTARES. In KM3NeT instead, a new framework has been developed, called **Jpp** [70], a Java inspired set of C++ interfaces, classes and methods, which is now widely used, for trigger algorithms, track reconstruction, optical data analysis, PDFs creation, etc. Hence there was the need to include in the Jpp framework also the shower reconstruction so that it could be easily used with the KM3NeT data. My task has been to develop the shower reconstruction in the Jpp framework with a different approach from the Standard Reconstruction and comparing the results.
In this chapter I will firstly introduce the shower topology, then I will focus on the observables needed for the reconstruction and finally I will describe the reconstruction procedure and its performances.

5.1 Electromagnetic Shower Topology

At low energies electrons and positrons primarily lose energy by ionization, although other processes (Moller scattering, Bhabha scattering, e+ annihilation) contribute, as shown in Fig. 5.1 [2].
At high energies instead electrons and positrons predominantly lose energy in matter by bremsstrahlung, while high-energy photons by e^+e^- pair pro-

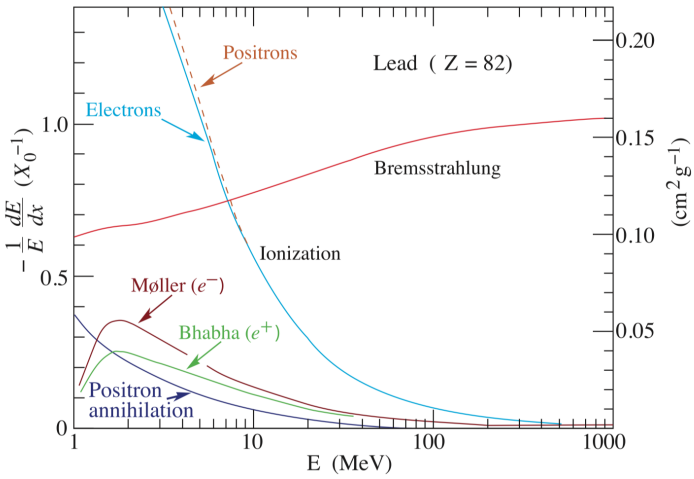

Figure 5.1: Fractional energy loss per radiation length in lead as a function of electron or positron energy. Figure taken from [2].

duction. The characteristic amount of traversed matter for these related interactions is called radiation length X_0, usually measured in g cm^{-2}. It is both

- he mean distance over which a high-energy electron loses all but 1/e of its energy by bremsstrahlung,
- $\frac{7}{9}$ of the mean free path for pair production by a high-energy photon [2].

While ionization loss rates rise logarithmically with energy, bremsstrahlung losses rise nearly linearly. It is possible to define the critical energy E_C as the energy at which the two loss rates are equal. In water [2],

$$E_C \sim 80\,\mathrm{MeV}, \text{ for electrons/positrons} \quad (5.1)$$

$$E_C \sim 1\,\mathrm{TeV}, \text{ for muons} \quad (5.2)$$

When a high-energy electron or photon passes through a thick absorber, it generates more and more photons and electrons with lower energies via pair production and bremsstrahlung, giving rise to an electromagnetic shower. Electron energies eventually fall below the critical energy, and then dissipate their remaining energy by ionization and excitation rather than by the generation of more shower particles.
The shape of electromagnetic showers and its evolution have been extensively studied by different experiments [2] and it will be described in the next session.

5.1.1 Longitudinal and Transverse EM Shower Profile

The energy deposition of an electromagnetic cascade as a function of the longitudinal distance L is reasonably well described by:

$$P_{emission}(L, a, b) = L^{a-1} \frac{e^{-L/b}}{b^a \Gamma(a)} \tag{5.3}$$

where L is the longitudinal distance from the EM shower starting point and a, b are respectively the *shape* parameter, that varies linearly with $\ln E$ and the *scale* parameter, that is approximately constant. Their values in sea water have been evaluated in Ref. [71] with a fit performed for different shower energies. The result is:

$$a = 1.85 + 0.62 \cdot \ln \frac{E}{\text{GeV}} \tag{5.4}$$

$$b = 0.54 \tag{5.5}$$

In Fig. 5.2 I show the EM shower emission probability in water for different primary electron energies.

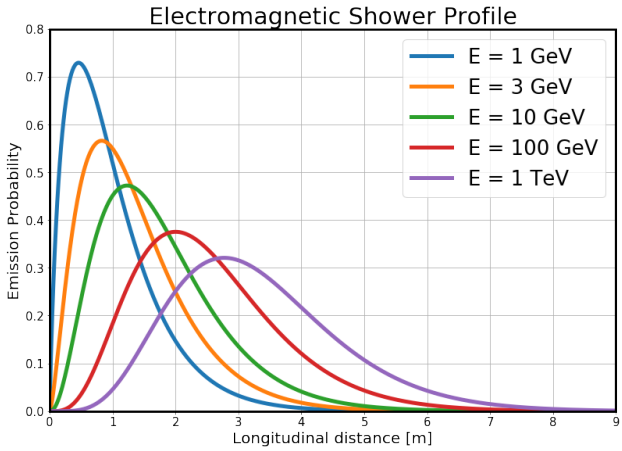

Figure 5.2: Longitudinal light emission probability for electromagnetic showers with different energies in water.

The transverse development of electromagnetic showers in different materials scales fairly accurately with the Moliere radius R_M, given by:

$$R_M = X_0 \frac{E_S}{E_C} \tag{5.6}$$

where $X_0 \sim 39$ cm in water, $E_S = \sqrt{4\pi/\alpha} m_e c^2 = 21.2$ MeV is the scale energy, and E_C is given by 5.2, hence

$$R_M \sim 10\,\text{cm in water} \tag{5.7}$$

On average, only 10% of the energy lies outside the cylinder with radius R_M. About 99% is contained inside of 3.5 R_M [2].

5.2 Hadronc Shower Topology

Every neutrino interaction (NC and CC) with nuclei produces hadronic particles which initiate hadronic showers. Fig. 5.3 shows the kinetic energy distributions for the different particle species produced in such hadronic interactions: we can see that the dominant particle species are pions, protons and neutrons. The excess of low-energy protons and neutrons comes from the 'breakup' of the nucleus [68].

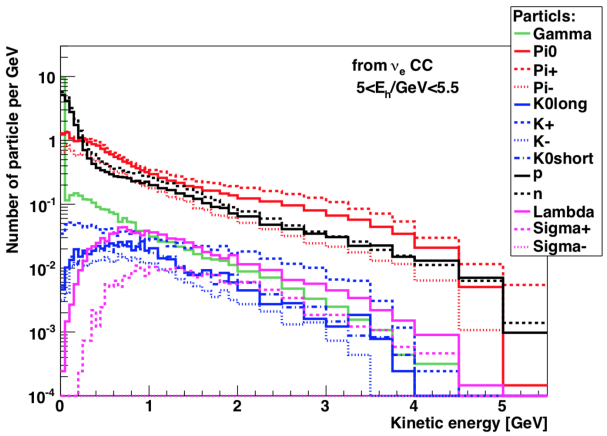

Figure 5.3: Kinetic energy distributions for different particle species in hadronic showers produced in ν-CC events. Figure taken from [68].

Showers developed by hadrons have a more complex topology with respect to EM showers, that is given by the strong interaction, which is responsible for [73]:

- The occurrence of nuclear reactions. In these processes, hadronic particles are released from atomic nuclei. These particles can be neutral (neutrons), i.e. not visible by our detector, or can further interact with the surrounding medium creating other particles with lower energies. The sum of these processes results in the fact that part of the released energy is *invisible for our detector*.

- The production of hadronic shower particles. The vast majority of these, $\sim$ 90%, are pions (see Fig. 5.3). The neutral pions decay in 2 photons, which develop an em shower.

The EM showers initiated by π_0s develop in the same way as the standard ones initiated by high-energy photons. The fraction of the shower energy carried by this EM component, f_{em}, varies strongly from event to event. On average, this fraction increases with the shower energy, since more π_0s are produced by secondary and higher-order shower particles: **the larger the shower energy, the more generations of shower particles, hence the more generation of π_0, the larger f_{em}.** Typically, f_{em} increases from ∼30% at 10 GeV to ∼50% at 100 GeV [73].
These characteristics have important consequences for shower reconstructions:

- As a result of the invisible-energy phenomenon, the detected signals for hadrons are in general smaller than for electrons of the same energy (non-compensation).
- Since the EM energy fraction is energy dependent, the detected energy is non-linear for hadronic showers.

The energy in ORCA is estimated counting the number of detected Cherenkov photons (hits) by our PMTs.

5.3 Detected photons (Hits) from EM and Hadronic Shower

Fig. 5.4 (a) shows that the number of detected photons (hits) from a pure EM shower is linearly proportional on the shower energy, as discussed in Sec. 5.1. However, in Sec. 5.2, we have seen that this is not true in the case of hadronic shower. Actually, the number of photons coming from an hadronic shower $N_{\gamma,H}$ can be expressed as a fraction f_H relative to that from electromagnetic cascades of the same energy, $N_{\gamma,e}$, i.e.

$$N_{\gamma,H}(E_H) = f_H(E_H) N_{\gamma,e}(E_H) \tag{5.8}$$

The fraction f_H has been estimated in [74]:

$$f_H(E_H) = 1 - 0.681 \left(\frac{E_H}{0.863\,\text{GeV}} \right)^{-0.207} \tag{5.9}$$

Fig. 5.4 (b) shows this fraction as function of the hadronic shower energy I obtained with the ORCA MC. In red it is shown eq. 5.9 and we can see that there is consistency between the two.
The value of f_H never reaches 1 due to the invisible-energy discussed in Sec.

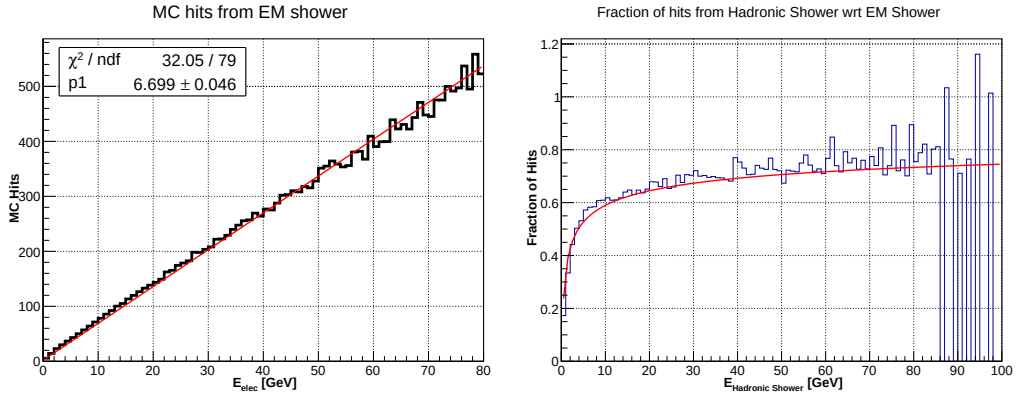

(a) (b)

Figure 5.4: (a) Number of hits from a pure EM shower in function of the primary electron energy. The red line is the fit with: $N_{hits} = p1 \times E_{elec}$. (b) Fractional number of photons of an hadronic shower with respect to a pure EM one with the same energy. The red line shows the same quantity evaluated using eq. 5.9.

5.2. And the fact that f_H grows at higher energies is due to the increased π_0 production which develops EM showers (Sec. 5.2). Actually, from Fig. 5.4 (b) we can also notice that at higher energies f_H tends to remain approximately constant: this is due to the fact that at higher energies, the em shower produced by π_0s starts to be important, hence, the ratio with the hits due to a standard EM shower tends to be constant.
Fig. 5.4 shows that the number of hits seen by our detector is the crucial information for shower reconstruction. However, from PMTs we also have the ToT information (see Sec. 3.7.1). Hence, it is natural to ask whether this information can actually help the reconstruction.

5.3.1 ToT information vs Number of Hits

Since the DOMs used in KM3NeT have 31 PMTs, we have another information of the energy of an event: the total number of hits. At the same time, the ToT provides information of the charge, since it is related to the number of photoelectrons detected by a PMT. Hence it is worth to see if these 2 quantities, **mean number of hits** and **mean ToT**, are both important in evaluating the energy of an event, or maybe one of the two, or even better, the combination of the two, has more impact in reconstruction algorithms.
Up to now, the ToT is not considered in the standard reconstruction algo-

rithms.
The plot in Fig. 5.5 (a) shows the ToT distribution as a function of the distance from the neutrino interaction vertex and neutrino energy and in Fig. 5.6 (a) we can see a projection for fixed distances. Fig. 5.5 (b) instead shows the number of hits distribution, to visualize the difference with respect to the ToT information. Finally, Fig. 5.6 (b) shows the ratio N_{hits}/ToT as a function of the neutrino energy. These plots have been done by selecting well contained events, in particular, whose neutrino interaction vertex was inside of a sphere of 50 m radius from the detector center.

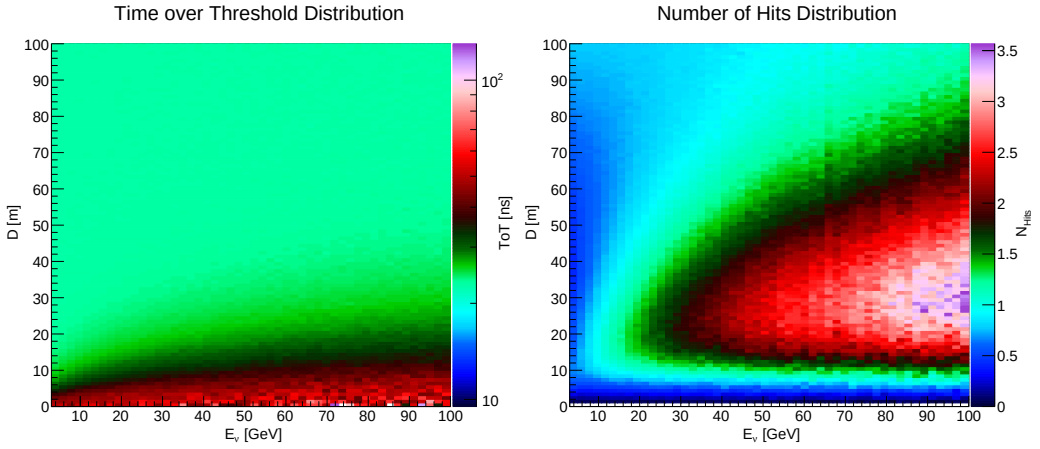

(a) (b)

Figure 5.5: (a) ToT and (b) number of hits distributions in function of neutrino energy and distance from the neutrino interaction vertex.

We can conclude from Fig. 5.5 (a) and Fig. 5.6 (a) that the ToT information can be useful only for hits quite near to the shower vertex, because at higher distances the mean ToT value tends to flatten to $\sim$ 25 ns, the value for 1 single photo electron. However, if we compare Fig. 5.5 (a) with (b) and especially with Fig. 5.6 (b) we can clearly see that the number of hits has a stronger dependence both on neutrino energy and distance. This is why the current reconstruction algorithms (for tracks and showers) use the number of hits and not the ToT.
But still, more investigations on the ToT need to be done, in particular, it can be useful, if we consider hits at small distances from the reconstructed shower vertex, to maybe estimate the energy.

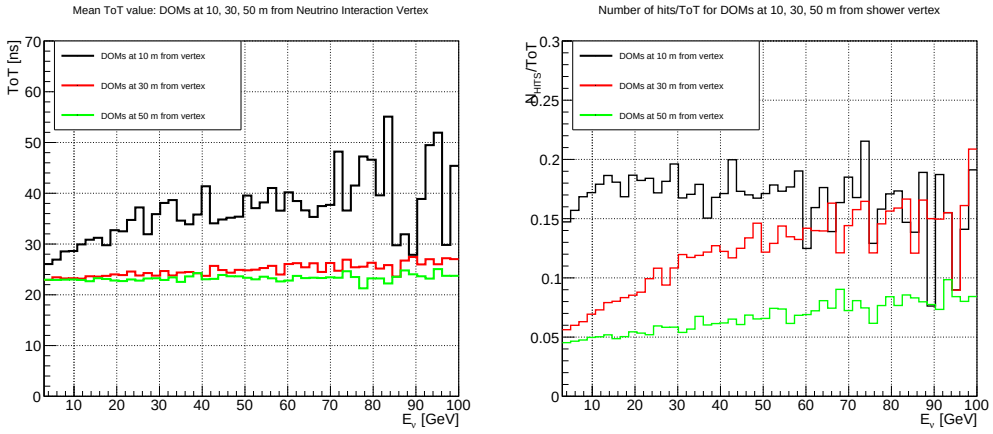

(a) (b)

Figure 5.6: (a) Mean ToT as a function of neutrino energy for fixed distanced from the neutrino interaction vertex. (b) Ratio between mean number of hits and mean ToT as a function of neutrino energy.

5.4 Shower Reconstruction Scheme

The shower reconstruction algorithm scheme is shown in Fig. 5.7.
First the shower vertex is reconstruted, intended not as the neutrino interaction vertex but as the shower brightest point. As we have seen in Fig. 5.2 this point is shifted with respect to the neutrino interaction vertex by a few meters (depending on the shower energy). Finally the fundamental quantities, i.e. the shower direction and energy can be reconstructed. For particle identification studies (PID) it is also useful to estimate the Bjorken Y, defined in eq. 3.5 to evaluate whether an event is more EM or Hadronic like. However, this variable is very hard to reconstruct with the ORCA PMT density. All these points will be described here. But firstly I want to clarify that the concept of all the reconstruction steps is to find the best variables values (such as shower position, direction and energy) by a fit which maximises a defined Likelihood landscape (actually a minimisation on -Log Likelihood is performed). In this respect, I have used the same minimiser for all the reconstruction steps.
In general, finding a global extremum is a very difficult problem. And unfortunately there is no perfect minimisation/maximisation algorithm, hence the choice of the minimiser can be based on [72] methods that need only evaluations of the function to be minimised and methods that also require the derivative of the function. In the multidimensional case, this derivative is the

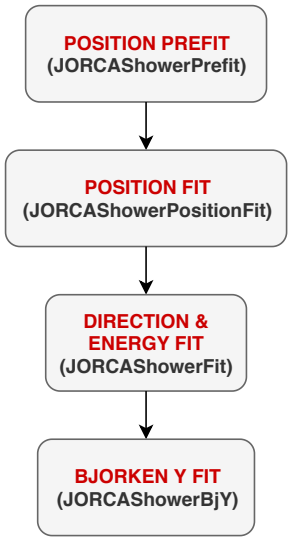

Figure 5.7: Scheme of the Shower Reconstruction algorithm.

gradient. Algorithms using the derivative are somewhat more powerful than those using only the function, but not always enough so as to compensate for the additional calculations of the derivatives (they are of course slower). The minimiser used in my shower reconstruction is JSimplex, based on Powell's algorithm [72] and implemented into Jpp. It does not evaluate the likelihood gradient but it evaluates the function value given a set of initial directions for the descent. The reason of this choice is that the shower reconstruction is by definition slow because for each triggered event it has to loop over **all** the PMTs within a certain distance from the reconstructed vertex. Hence an algorithm that evaluate also the gradient for each minimization step would be too slow.
With this in mind, each reconstruction step can now be described.

5.4.1 Position Prefit

The first thing to do in a reconstruction algorithm is the hit (detected photons by PMTs) selection: in this part it is very important to find a good cluster of hits, because due to the amount of ^{40}K and bioluminescence background, a fraction of the selected hits can be background hits and they could worsen the reconstruction performances. Each single hit in the detector, before any selection, is called **L0**. Two hits in the same DOM which occur in a certain

time window Δt and in a certain angle are called **L2** hits. Similarly, 3 hits on the same DOM occurring in a certain Δt and angle are called $L3$ and so on.
Since the ^{40}K background is casual, it will produce many random L0 hits. Instead, we should expect that due to this randomness, the probability to produce two or more hits on the same DOM (L2, L3, etc) in a certain Δt and angle decreases.
Hits coming from a shower, instead, are causally correlated according to:

$$t_{res} = t_{hit} - t_{vx} - d/c_{water} \tag{5.10}$$

where t_{hit} is the time at which the hit is detected by the PMT, t_{vx} is the vertex time, d the distance between the shower vertex position and the photon detection position and c_{water} is the speed of light in water.
More in general, 2 hits, i and j are causally connected if they satisfy:

$$|t_i - t_j| \leq |\vec{x}_i - \vec{x}_j|/c_{water} + T_{extra} \tag{5.11}$$

with T_{extra} accounting for timing uncertainties as well as photon scattering. Its value will be discussed later.
The prefit algorithm starts by selecting:

- a cluster of causally connected L2s defined with $\Delta t = 20$ ns and $\cos\alpha = -0.7$ which corresponds to an angle $\alpha \sim 135°$.

The hit correlation follows eq. 5.11 with $|\vec{x}_i - \vec{x}_j| = 50$ m and $T_{extra} = 20$ ns. Once the cluster of causally connected L2 hits is created, a loop over all L0s is done: in this loop, each L0 is checked if it is causally connected to one of the L2 hits using again eq. 5.11 with $|\vec{x}_i - \vec{x}_j| = 50$ m and $T_{extra} = 20$ ns. If yes: the L0 is added to the L2 cluster, otherwise it is not considered.
After adding L0s to L2s, **only** the L0s are again clusterized with the same causality hypothesis. The reason why only L0s are clusterized is because we don't want to accidentally lose some L2s of the initial cluster during this procedure.
At this point we have a cluster of causally connected L2+L0 hits and the first fit can start. This first fit is conceptually simple: it finds the barycenter of these hits according to the scheme of Fig. 5.8.
To find the barycenter of the hits it follows two cases, based on the size of the L2+L0 cluster:

1. if the number of L2+L0 hits (i.e. the size of the cluster) is ≤ 40 (this value has been chosen as it appears to give the best reconstruction performances), it considers all hits from the first one to the **last** hit of

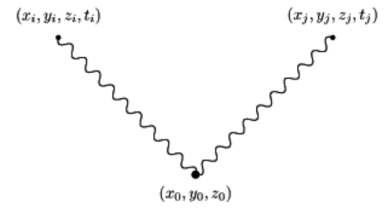

$$t_j = t_0 + \frac{c}{n} \times \sqrt{((x_j - x_0)^2 + (y_j - y_0)^2 + (z_j - z_0)^2)}$$

x_0 = x position of vertex (fit parameter)
y_0 = y position of vertex (fit parameter)
z_0 = z position of vertex (fit parameter)
t_0 = time at vertex (fit parameter)

c = speed of light (in vacuum)
n = index of refraction

$$t'_j \equiv nct_j$$
$$t'_0 \equiv nct_0$$
$$\Rightarrow (t'_j - t'_0)^2 = (x_j - x_0)^2 + (y_j - y_0)^2 + (z_j - z_0)^2$$

Figure 5.8: Scheme for the barycenter evaluation of 4D points (x,y,z,t) used in the vertex prefit.

the cluster and makes the baricenter fit. Then, it removes the last hit and performs again the barycenter fit with the same cluster except for that one. This procedure is done by removing time by time hits and it stops when the cluster remains with the first 4 hits: this is because we want to reconstruct a 4D point (x,y,z,t), and since this is a linear problem, we need at least 4 hits for that, hence we cannot remove them. From all these minimizations, the best barycenter (in terms of the final likelihood value), that is the vertex hypothesis, is chosen.

2. if the number of L2+L0 hits is ≥ 40: in this case the barycenter evaluation is done just once with all the hits in the cluster. The reason for this is mainly because it saves computational time and the final result does not change with respect to the procedure of the previous point.

After this step we have the **first reconstructed vertex**. But since this procedure is really sensitive to background hits in the hit selection, the result is not optimal. Hence, still in the prefit code a second fit, more precise and based on the standard shower reconstruction procedure, is applied:

- Starting from the first reconstructed vertex (x_0, y_0, z_0, t_0), a grid of vertex hypotheses is built around it in (x,y,z,t) (in particular in x,y,z

goes from ±20 m by steps of 20 m, and in time goes from ±50 ns by steps of 25 ns).

- For each of these vertex hypotheses, a new cluster of only L0 hits, causally connected to these vertexes by the eq. 5.10 with D = 80 m and $\Delta t = 100$ ns is built.

- The selected L0s are fit with their vertex hypothesis by using an **analytical PDF** taken from [68]:

$$P(t_{res}, \psi) = \frac{1}{\sqrt{a^2 + (t_{res}/ns)^2} + p(\psi)} \tag{5.12}$$

where the parameter a $\neq 0$ avoids the singularity for vanishing t_{res}. The function $p(\psi)$ penalises hits on PMTs that are not oriented towards the assumed vertex position. The penality is given by:

$$p(\psi) = \begin{cases} 0 & \text{if } \cos\psi < 0 \\ p_{max} & \text{if } \cos\psi > \cos\psi_{th} \\ p_{max} \times \cos\psi / \cos\psi_{th} & \text{else.} \end{cases}$$

where ψ_{th} is a threshold defining at which angle the maximal penalty p_{max} is reached [68]. For PMTs close to the vertex, a larger value for ψ_{th} is desirable in order to avoid rapid changes in the penalty for minor changes in the vertex position hypothesis. Therefore, a distance-dependent ψ_{th} is used:

$$\cos\psi_{th} = \frac{d_{ref}}{\sqrt{d_{ref}^2 + d^2}} \tag{5.13}$$

where d is the vertex-PMT distance and d_{ref} is a reference distance. In the following, a = 2 ns, $p_{max} = 100$ and $d_{ref} = 10$ m are used. Fig. 5.10 shows the improvement obtained by this second prefit procedure with respect to the barycenter one.
These reconstructed vertexes are finally sorted by looking at the quality of the fit and saved in a file.

5.4.2 Position Reconstruction

This second step has been introduced to improve the performances of the vertex prefit. In particular, it takes the first best reconstructed position from the previous step and performs a more precise fit. In this case, it selects again L0 hits but with these criteria: starting from the previous reconstructed vertex we can define the distance D, the time residual t_{res} and the angle Θ between the hit PMT and the vertex, then the hit is kept if:

- D $<$ 80m
- -40 ns $< t_{res} <$ 40 ns
- $\Theta <= 90°$

Hence, after this procedure we have a cluster of selected L0 hits and a vertex hypothesis. What we need now is a likelihood landscape to maximize. In order to build the likelihood we need a PDF (probability density function) of the detected hits.

PDF

The PDF used for the second vertex fit is shown in Fig. 5.9. It has been built from triggered hits from ORCA MC files and it already takes into account hits due to ^{40}K. The PDF is a function of time residuals defined in eq. 5.10 and of the distance, D, from the **neutrino interaction vertex** and every entry of the histogram has been scaled by $1/D^2$ to take into account the fact that at bigger distances we have more DOMs (and consecutively more PMTs). The scaling as D^2 appears to be a good approximation. If we wouldn't take into account the ^{40}K hits, the PDF would be empty for $\Delta t < 0$ since we couldn't have hits from the shower before it. In the PDF we can also see that we have more hits at higher t_{res} for higher distances: this is due to the scattering of the Cherenkov light in water, whose impact grows with distance.

Vertex Hypotheses

Once the PDF has been chosen, the reconstruction procedure can start: starting from the best reconstructed vertex from the position prefit, a grid of vertex hypotheses is built around it, in particular, these points are shifted in (x,y,z) by $\pm$ 28 m in steps of 6 m and in time by $\pm$ 60 ns in steps of 15 ns. For each of these vertex hypotheses the likelihood is evaluated and they are finally sorted by it. Then, the best 35 vertex hypotheses are taken for the likelihood maximization and finally sorted and saved in the output file.
Fig. 5.10 shows the median position reconstruction error with respect to the neutrino interaction vertex for the position prefit and fit (blue line). Since the error is referred to the neutrino interaction point, and we are actually reconstructing the shower brightest point, shifted of $>$ 1 m from it, part of this error accounts for this fact.
Fig. 5.11 shows the longitudinal and transverse error with respect to the shower brightest point for the standard reconstruction (a) and my reconstruction (b). From the comparison we can see that for my reconstruction

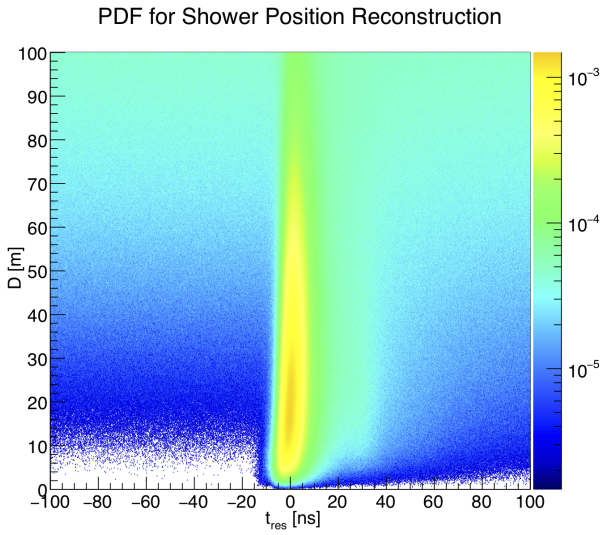

Figure 5.9: PDF of hits in function of time residual and distance with respect to the neutrino interaction vertex. This PDF is used for the second position reconstruction.

the peak is more centered to 0, but I have more outliers. However they appear to be comparable.
Once we have a good reconstructed vertex we can proceed with the direction and energy reconstructions, which are the important variables needed for analyses.

5.4.3 Energy and Direction Reconstruction

The energy and direction reconstruction is done at the PMT level. The standard reconstruction instead is done at the DOM level, i.e. the PMTs information of each DOM are summed. The reason for my approach is that:

1. it has never been tried before,
2. if we look at single PMTs we can easily consider in the reconstruction their real detection efficiencies, PMT by PMT (once they are all measured) instead of taking a reference value from MC.

Also in this case, the reconstruction starts with L0 hits. Again, it takes the best reconstructed vertex from the position fit and builds a cluster of L0 hits around it with these criteria:

- D $<$ 80 m

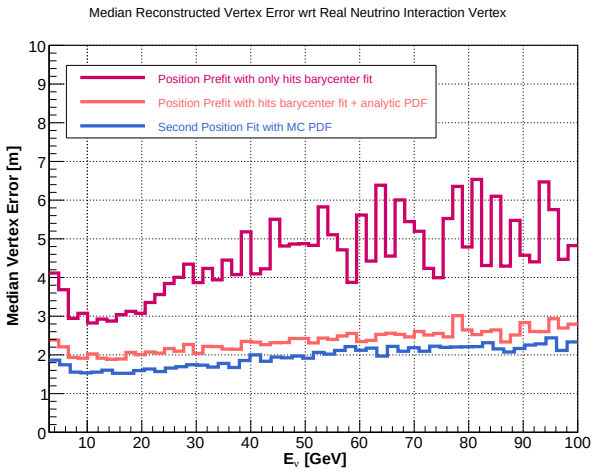

Figure 5.10: Median reconstruction error with respect to the neutrino interaction point. The error is shown for both the prefit procedures and for the fit.

- -25 ns $< t_{res} <$ 25 ns
- $\Theta <= 90°$

This cluster of hits is then used to evaluate the initial energy hypothesis and the initial direction. In particular, for the direction, the PMT positions of each L0 hit are considered with respect to the shower vertex and their vectorial sum is performed. The result of the sum is taken as first direction hypothesis. Instead, the energy starting value is evaluated by looking at the number of selected hits.
Hence, as in the previous step, we have a shower hypothesis and a cluster of L0 hits and we need a PDF to build the likelihood to maximize.

5.4.4 Parameterized PDF at PMT level

The PDF used for the direction and energy reconstruction is a pure EM parameterized PDF. I.e. it is built with a Jpp application that tabulates the arrival time of the Cherenkov light on a PMT from a shower in function of

$$\text{PDF} = P(D, \theta_0, \theta_{PMT}, \phi_{PMT}) \tag{5.14}$$

where, as shown in Fig. 5.12, D = distance between the vertex and the PMT, θ_0 = cosine of the photon emission angle with respect to the electron direction, θ_{PMT}, ϕ_{PMT} = orientation angles of the PMT. The orientation of

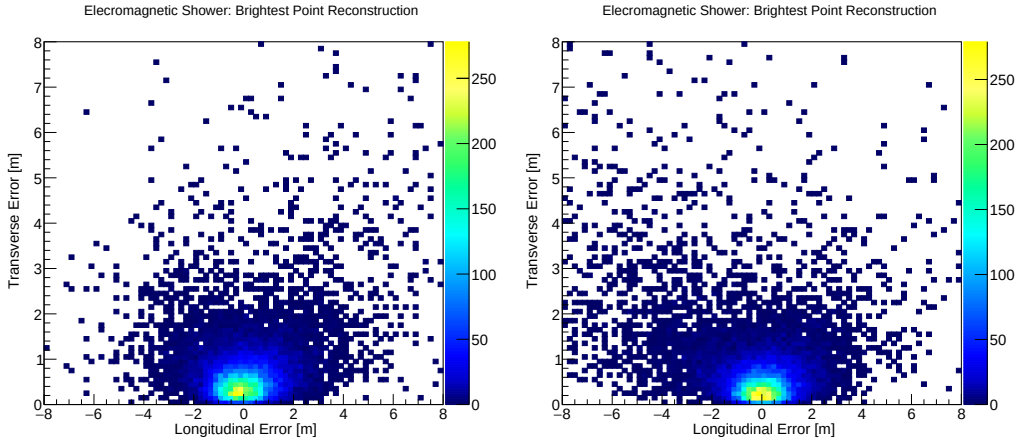

(a) Std Reconstruction (b) My Reconstruction

Figure 5.11: Reconstructed events distribution as function of the longitudinal and transverse reconstruction errors with respect to the MC EM brightest points.

the PMT is defined in the coordinate system in which the shower developes along the z-axis and the PMT is located in the x-z plane.
Hence, the PDF does not explicitly depend on the EM shower energy. But, as we have seen in Fig. 5.4 (a) the number of hits from an EM shower grows linearly with the shower energy, hence we can simply multiply the PDF by the assumed shower energy in our reconstruction. This has the advantage of removing one dimension in the PDF and consequently speeding the fit.
Fig. 5.13 shows the PDF projection on (D, $\cos\theta_0$) for the 4 PMT directions (north, south, werst, ovest) as seen in Fig. 5.12. As we can see, the best direction is the one pointing on the shower, i.e. the west. And in fact in this case the Cherenkov peak at ~ 0.73 is well visible. Even if the PDF is energy independent, we can at least plot it in such a way to take into account the different longitudinal light distribution of the shower which depends on the energy, as we have seen in Fig. 5.2. This is why in Fig. 5.13 there is the energy information (taken into account only for the longitudinal shape of the shower and not for the z axis of the plot).
We should however expect that the longitudinal emission is important only for PMTs "near" to the shower. The further away we go, the more shower will be seen as a point like source. This is shown in Fig. 5.14, where we can see in (a) the PDF projection for a PMT pointing in the west direction located at 10 m from the neutrino interaction vertex. In this case it was considered a shower of 5, 20, 70 GeV. The y axis does not take into account the

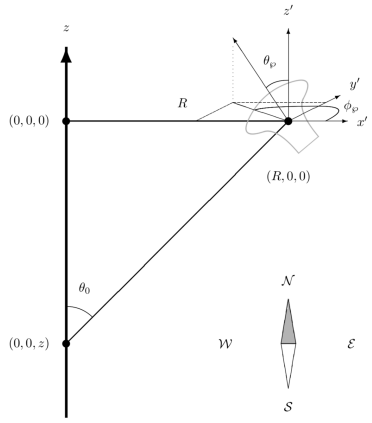

Figure 5.12: Reference system of the PDF used in the shower reconstruction.

shower energy, it was considered only for the shower longitudinal elongation that influences the emission profile. And we can see from the plot that there is actually a shift of the Cherenkov peak due to the different length of the showers. Instead, in Fig. 5.14 (b) we see the same quantity but for a PMT at 50 m from the vertex. In this case we do not have differences due to the shower elongation, because it is seen as a point, as expected.
Once we have the shower hypotheses and the PDF we can start the reconstruction procedure: the likelihood is evaluated at a grid of directions and energies around the starting points. These starting hypotheses are finally sorted and the best 20 are considered as starting points for the fit. The results of the fit are sorted by their likelihood value and saved in the output file.
It has to be told that typically, if we use a pure EM PDF, the energy fit will not be optimal because part of the hits that the detector sees come also from the hadronic particles, hence we lose the linearity given by multiplying the PDF by the energy. Hence, as a result, the reconstructed energy is typically corrected. In my case the correction is made from a linear fit to the reconstruction error in function of the energy. In the standard reconstruction instead, there are 2 consecutive energy corrections. The first one is a simple linear correction (as in my case), which will be referred as **not corrected**. The second one instead is more complex and precise and takes into account also the reconstructed Bjorken Y [68], this will be referred as **corrected** energy. Hence, in the next plots, to have a fair comparison, my reconstruction performances should be compared with the **not corrected** energy. But I put also plots with the corrected one to see the improvement it gives.

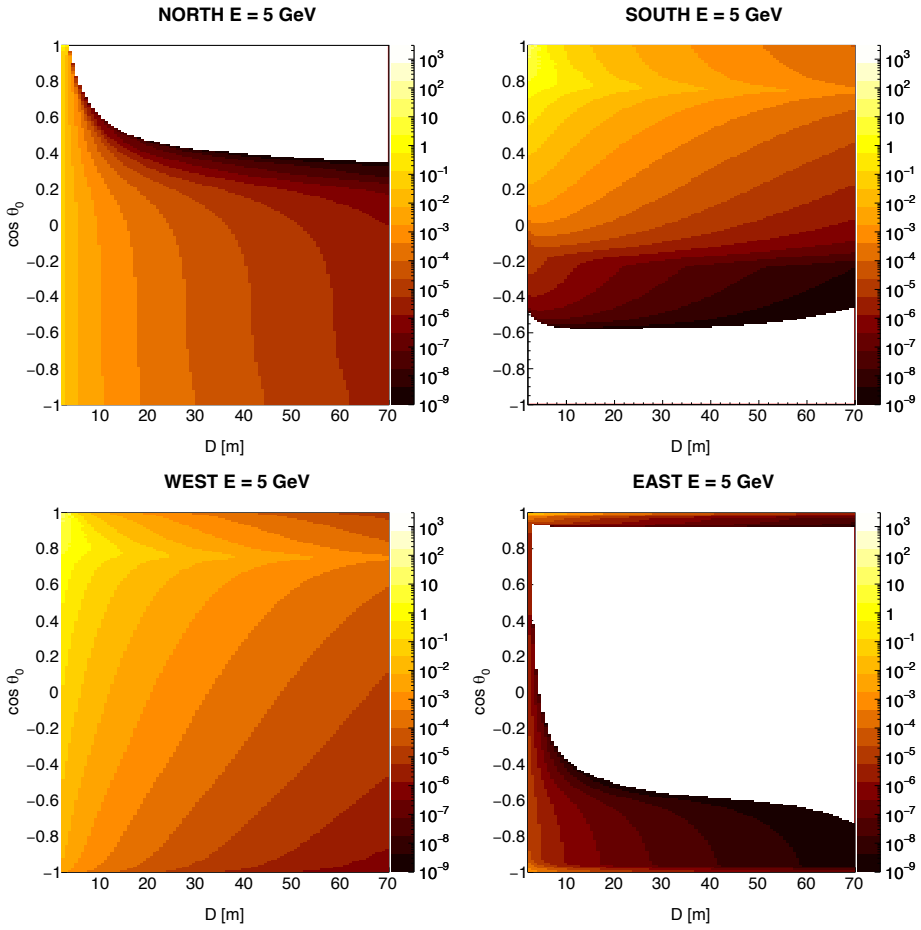

Figure 5.13: PDF Projection of a 5 GeV EM shower along distance and cosine of the emission angle for a PMT pointing in the 4 directions.

Direction and Energy Reconstruction Performances

Fig. 5.15 shows the median direction reconstruction error with respect to the neutrino direction.
It also shows the performances of the standard reconstruction to have a comparison of the two. From it we can clearly see that at lower neutrino energies the error increases. The reasons are:

1. The kinematics: at lower neutrino energies, the angle between the neutrino and the primary electron is bigger (see blue line of Fig. 5.15). Hence this represents a physical limit for the reconstruction.

2. At lower neutrino energies we have less hits, hence the reconstruction error is bigger.

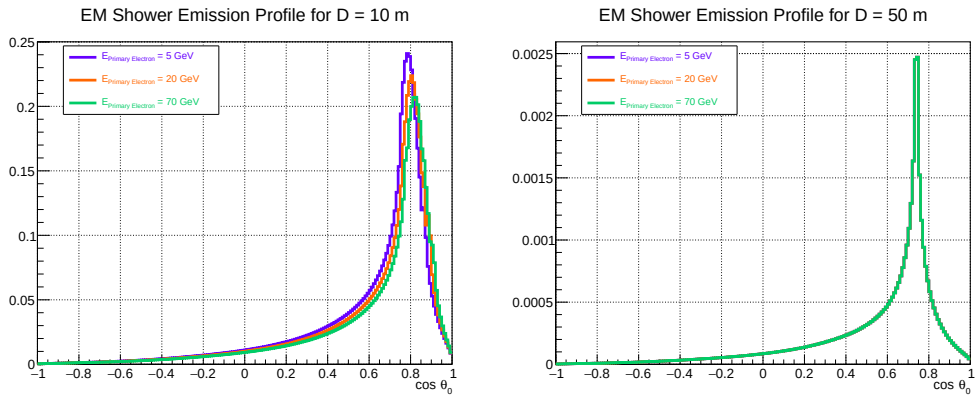

Figure 5.14: Em shower emission profiles.

From the comparison with the standard reconstruction we can conclude that they perform similarly for the direction reconstruction.
Fig. 5.16 shows the energy reconstruction performances for (a) standard reconstruction (at the DOM level) - with corrected energy, and (b) my reconstruction - with not corrected energy.
To better compare the two reconstructions, in Fig. 5.17 is shown the mean fractional energy error for my reconstruction and the standard one for both the corrected and the not corrected case. From it we can see that my reconstruction seems to perform better at lower energies (up to 10 GeV if we compare it with Std-Not corrected). But at higher energies, the Std reconstruction has a better behavior. Clearly, a corrected reconstruction of the Bjorken Y is useful to improve the energy reconstruction performances and this will be discussed in the final paragraph.
Fig. 5.18 and 5.19 show the energy error distribution for events with reconstructed energy between 3-5 and 8-10 GeV. From them we can deduce that for very low energies my reconstruction seems to perform better but at higher energies the peak of the distribution is not centered at 0, which means that the linear correction I have made is not optimal, and I have a bit more populated tails.
The shower reconstruction has to loop over **ALL** PMTs inside a certain distance from the shower vertex and evaluate the probability of hit/not-hit PMTs. If we consider FULL ORCA, in which we have a total of 115 DUs $\times$ 18 DOMs $\times$ 31 PMTs = 64170 PMTs, it would mean that for **each minimization step**, it has to loop over a very large number of PMTs, even if we consider the ones inside a certain distance from the shower vertex. This of course is a limitation since it slows quite a lot the code. Then the choice

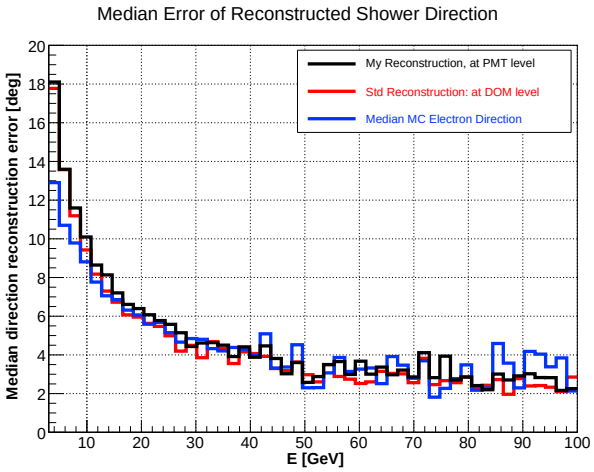

Figure 5.15: Median reconstructed direction error with respect to the MC neutrino direction. The blue line shows the median MC primary electron direction with respect to the neutrino. This way we can have an idea of the effect of kinematics in the low energy region and in the reconstruction error.

of the maximum distance for the loop is quite important in terms of reconstruction speed. We can start thinking about the absorption and scattering length in water, for which considering a distance > 80 m would be quite useless since we do not expect signal hits above it. At the same time, considering small distances, even if it could speed the code, it would make us lose part of the information. We need a tuning between distance and speed. All the plots shown above are made with $D_{max} = 80$ m, and in this case, **the reconstruction procedure takes ~ 12 seconds per event**. The standard reconstruction instead, since it is performed at the DOM level, is faster: it takes ~ 5 seconds per event.
The comparison of the shower parameters obtained with my reconstruction code with respect to the standard one shows that some differences persist. The difference is negligible in the reconstructed direction and within 5% in the energy reconstruction. Though not so relevant, there is still space for a further improvements.
In particular, regarding the optimization of the computational time/event I performed some tests by changing the D_{max} parameter.

Distance Investigations

Fig. 5.20 shows the reconstruction performances for different D_{max} values. From them we can conclude that both the error in the reconstructed direction

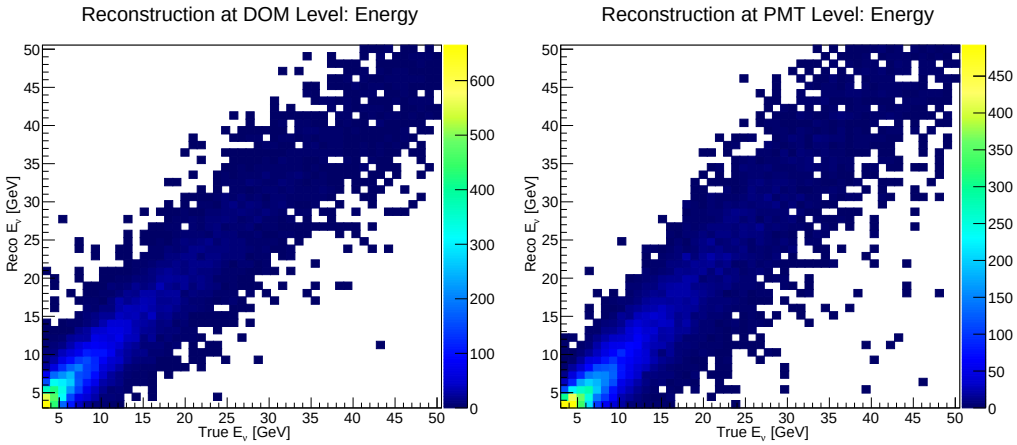

(a) (b)

Figure 5.16: Energy Reconstruction Performances: (a) the Standard Reconstruction at the DOM level, (b) my reconstruction "JShowerFit" at the PMT level.

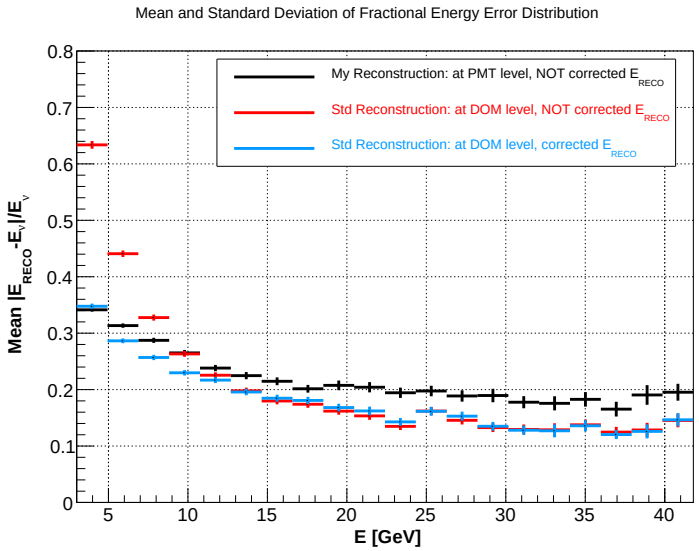

Figure 5.17: Mean fractional energy error.

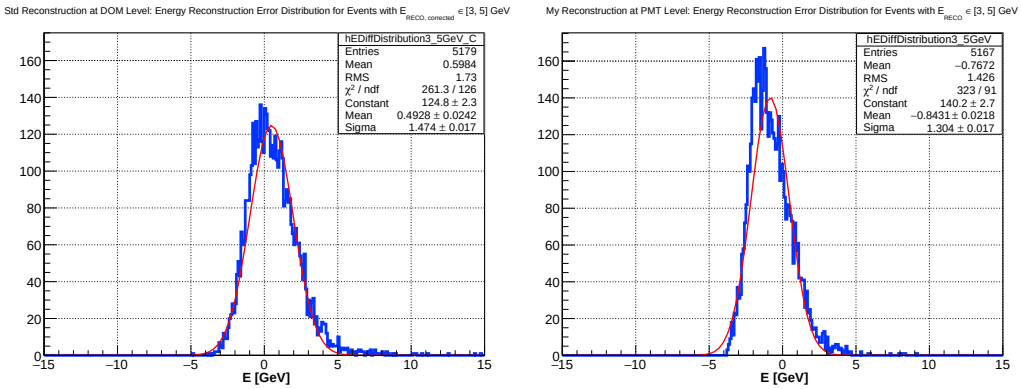

(a) (b)

Figure 5.18: Energy error distribution for events with reconstructed energy between 3-5 GeV, (a) for the standard reconstruction, (b) for my reconstruction.

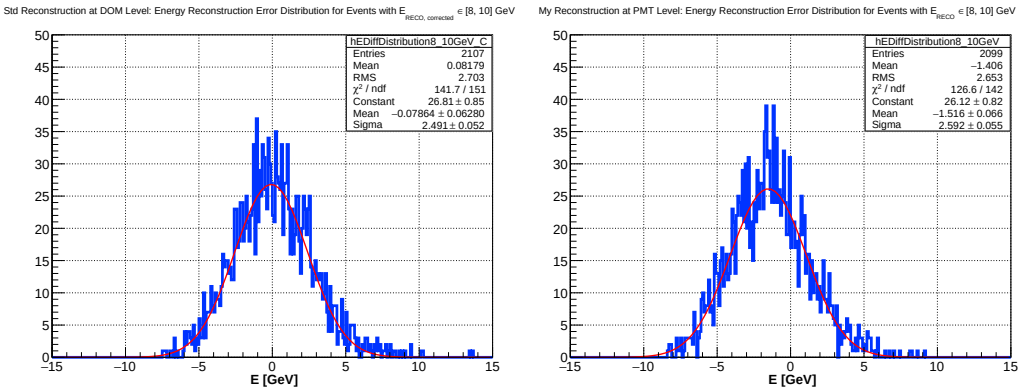

(a) (b)

Figure 5.19: Energy error distribution for events with reconstructed energy between 8-10 GeV, (a) for the standard reconstructio, (b) for my reconstruction.

and energy have a slight dependence on the parameter D_{max} for $D_{max} > 50$ m. To this extent the choice $D_{max} = 60$ m seems a good compromise. For this value the reconstruction time decreases down to 8 seconds per event, which is an acceptable value.

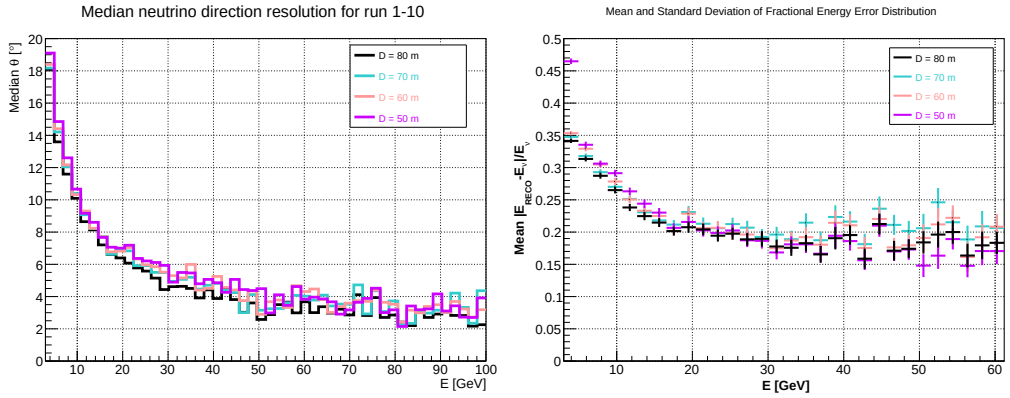

(a) (b)

Figure 5.20: Reconstruction performances for different distances: these distances are referred with respect to the reconstructed shower vertex and are important because the reconstruction loops over **all** PMTs inside the defined distance.

5.4.5 Bjorken Y Reconstruction

The Bjorken Y 3.5 is a useful variable to reconstruct because it allows to account for the different light yields of hadronic and EM showers which otherwise will intrinsically deteriorate the energy resolution [68] as shown in Fig. 5.4.

Fig. 5.21 (a) shows the Bjorken Y distribution in function of neutrino energy. Fig 5.21 (b) shows the projection of (a) along Bjorken Y for events with energy between 3-5 and 8-10 GeV. From (a) we can see that at low energies $E_\nu < 10$ GeV there is a structure due to the different neutrino interaction modes (DIS, quasi elastic scattering) [68]. We can also see that at lower energies there is a preference for lower values of Y, this instead is less visible at higher energies.

Fig. 5.22 (a) shows the angle between the primary electron and the hadronic shower, α, in function of the Bjorken Y. From it we can see that the angle tends to be lower for $Y_{Bj} \sim 0.5$, i.e. in the intermediate region. Fig. 5.22 (b) shows the Bjorken Y distribution (z axis) with respect to neutrino en-

ergy and α. First of all we can see that α decreases with increasing energy, and this is expected since, for 4-momentum conservation, at higher energies the primary lepton and the hadronic shower tend to be more collimated, in addition, if we look at the z axis, we can see, as expected from Fig. 5.22 (a) that low/high values of Y_{Bj} are responsible for bigger angles.

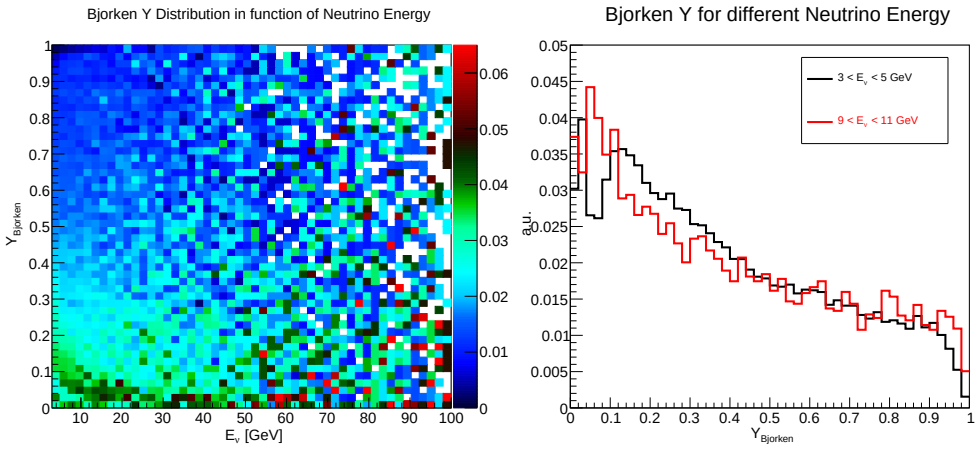

(a) (b)

Figure 5.21: Bjorken Y distribution.

With an ORCA-like detector it seems impossible to distinguish a shower induced by a single electron from a shower induced by a single hadron, since both resulting Cherenkov light cones are of similar intensity for the same particle energy [68]. Hence we should not expect high reconstruction performances in this case.
In the standard reconstruction [68], each event is fitted with 9 different **fixed** inelasticity Y assumptions ($Y = [0-0.1, 0.1-0.2, ..., 0.7-0.8, 0.8-1]$ where the last interval is bigger as the MC statistics decreases for $Y \to 1$) [68]. The case with the best likelihood value is then selected. This way we have a set of discrete Bjorken Y values.
To reconstruct the Bjorken Y I have tried a completely new approach. Very different from the standard reconstruction. With the assumption that each event the detector sees is composed by a pure EM shower + an hadronic shower, weighted with the Byorken Y value, we can assume that the probability of having a hit PMT is:

$$P = E_\nu \left((1 - \mathbf{Y})\mathrm{P}_{EM} + \mathbf{Y}\mathrm{P}_H\right) \tag{5.15}$$

Where $\mathrm{P}_{EM/H}$ are 2 separate 4 dimensonal PDF:

$$\mathrm{P}_{EM/H} = \mathrm{P}(D, \delta_C, \theta_{PMT}, \phi_{PMT}) \tag{5.16}$$

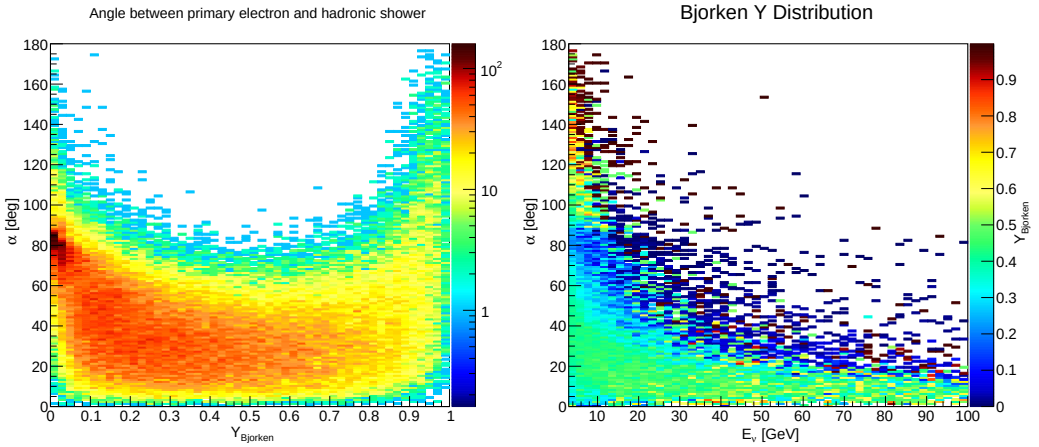

(a) (b)

Figure 5.22: Bjorken Y, neutrino energy and angle α between the primary electron and the hadronic shower distributions.

respectively for a pure EM shower and for hadronic shower. The pure EM PDF is exactly the same as in 5.4.4. The hadronic PDF has been built from Monte Carlo (see next section).
Hence, the Bjorken Y reconstruction works by taking the position, direction and energy information from the previous steps, then the shower position and direction are kept **fixed** during the fit, instead, the minimiser is allowed to move **simultaneously** in energy and Bjorken Y space.
As in the previous steps we need to give a starting point to the minimiser. For the energy it simply takes the reconstructed energy from the previous step. For the Bjorken Y instead, for each event I create an histogram of the Cherenkov emission of the hits with respect to the reconstructed shower direction. The reason for this choice is shown in Fig. 5.23: it is evident that the distribution of more hadronic-like events (i.e. with higher Bjorken Y values) is slightly different than the one of more em-like events. Once the histogram, is built for each event by taking triggered hits, I estimate the Bjorken Y as the ratio of the area above $\cos\theta_C > 0.4$ and the area of the remaining region. Once the PDF and the starting points are defined, the -Log likelihood minimisation can start. Again it is performed with JSimplex. After a focus on the hadronic PDF used, I will show the reconstruction performances.

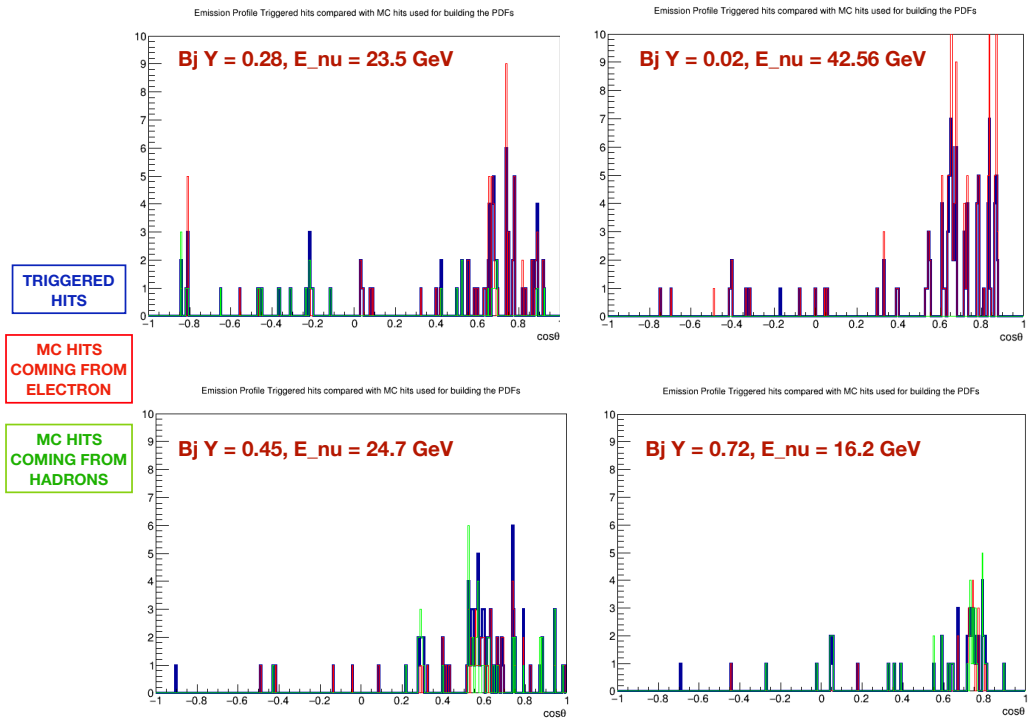

Figure 5.23: Cherenkov emission profile of the triggered hits (blue), compared with Monte Carlo hits coming from the pure EM shower (red) and the hadronic shower (green) for events with different Bjorken Y values.

Hadronic PDF

Differently from EM showers, hadronic showers present big fluctuations due to different hadronizations that occur event by event. Hence, building an hadronic shower PDF is not as precise as for EM showers. Furthermore, the hadronic fluctuations are also energy dependent, instead, in the 4D PDFs I am using, I am evaluating an "average" profile of the hadronic shower . We have seen that, for EM showers this is a good approximation since the number of hits grows linearly with the primary electron energy and we do not have so many fluctuations, instead in this case this has to be intended as an approximation.
The PDF has been built from MC files, and for each event, all the hits coming from all the hadronic particles have been taken. The shower direction is intended as the mean average of all the hadronic particles.
Fig. 5.24 shows the hadronic PDF projection in the same coordinate system of Fig. 5.12. It can be compared with Fig. 5.13. By looking at the WEST PMT we can still notice the Cherenkov peak at $\cos\theta_0 \sim 0.73$, even if less

pronounced with respect to the pure EM shower. We can also notice more fluctuations.
Instead, if we look at the emission profile in Fig. 5.25 we clearly see that we have a lower probability of a hit PMT from the hadronic shower, and in particular, if we look at the Integrals of the EM and hadronic profiles (I_{EM}, I_H) we obtain in this case $I_H/I_{EM} \sim 0.68$, which is consistent with what we expect from Fig. 5.4.

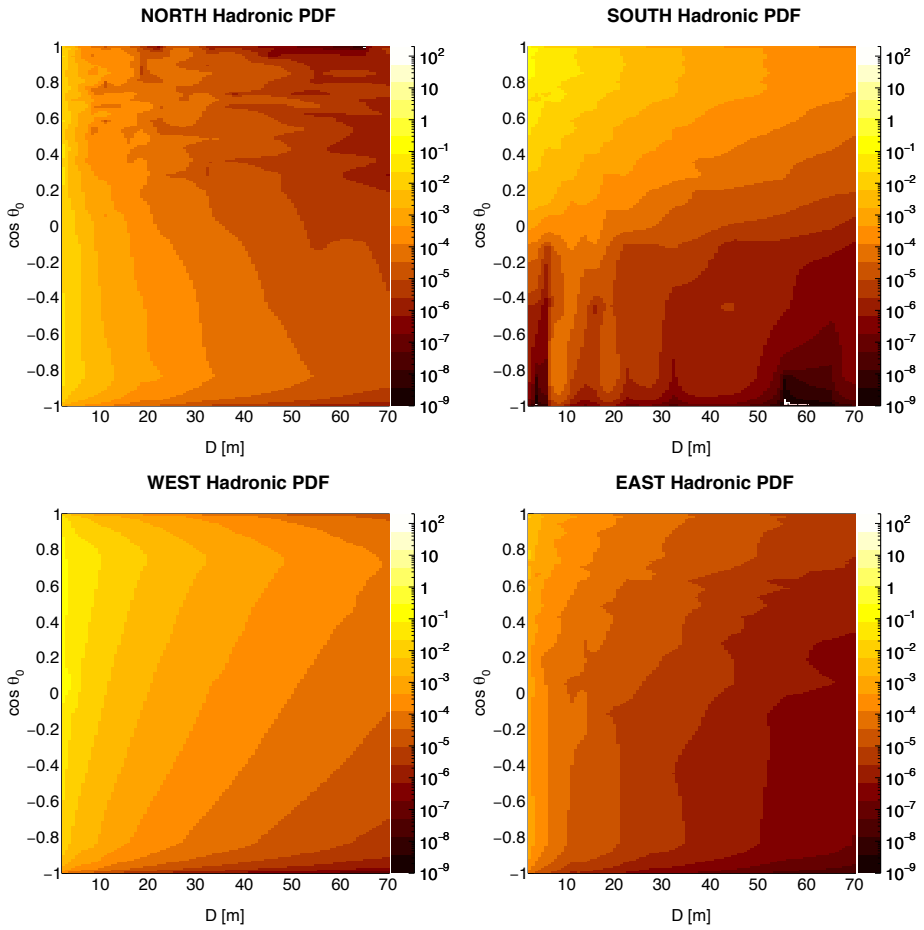

Figure 5.24: PDF projection of an hadronic shower along distance and cosine of the emission angle for a PMT pointing in the 4 directions.

Bjorken Y Reconstruction Performances

From the above discussion, the reader **should not expect a complete Bjorken Y reconstruction**, but mainly a more qualitative estimation.

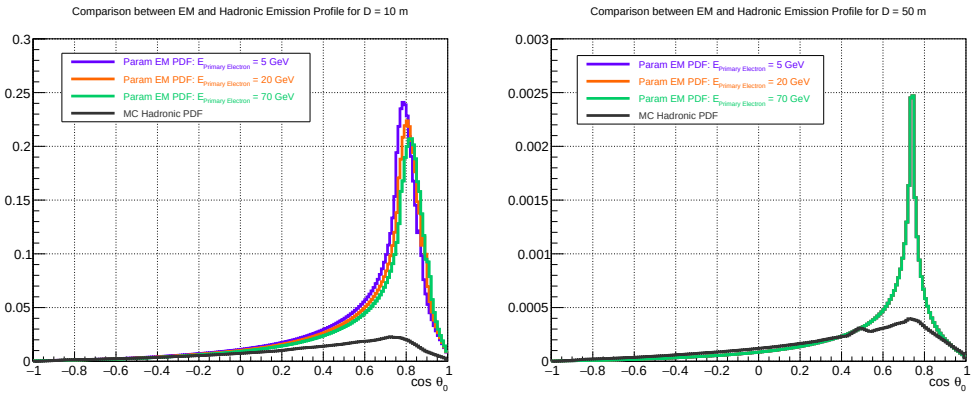

(a) (b)

Figure 5.25: EM and hadronic showers emission profiles. For (b) the integral of the EM profile is $I_{EM} = 0.041$, the integral for the hadronic profile is $I_H = 0.028$, leading to $I_H/I_{EM} \sim 0.68$ which is consistent with what we expect from Fig. 5.4.

This is shown in Fig. 5.26 and 5.27 both for the standard reconstruction (left) and for my reconstruction (right). In particular, Fig. 5.26 is made by selecting events with reconstructed energy between 3-5 GeV; in Fig. 5.27 instead, events with reconstructed energy between 8-10 GeV have been selected: both reconstructions do not perform as we have seen for example with the energy estimation and we can see the difference between the standard reconstruction which uses fixed, discrete values of Y and my reconstruction which instead uses continuous and free values of Y. From these plots we can conclude that my reconstruction performs better at lower energies, where there is correspondence between low Bjorken Y values; instead, at higher energies, the Y is a bit underestimated.
This can be also seen in Fig. 5.28 where the median Bjorken Y reconstruction error is shown for both reconstructions: the conclusion is that my reconstruction has a lower error for lower neutrino energies, which is the interesting region for the Neutrino Mass Ordering (NMO) analysis, that is the ORCA main goal.
Finally, as stated above, since in my reconstruction I simultaneously fit the energy and Bjorken Y, I show in Fig. 5.29 and Fig. 5.30 (that has to be compared with Fig. 5.18 (b)) that this procedure **naturally improves the reconstructed energy, especially in the low energy region, important for NMO analysis**. Beware that this improvement **is not due to an energy correction as it is done in the Standard Reconstruction,**

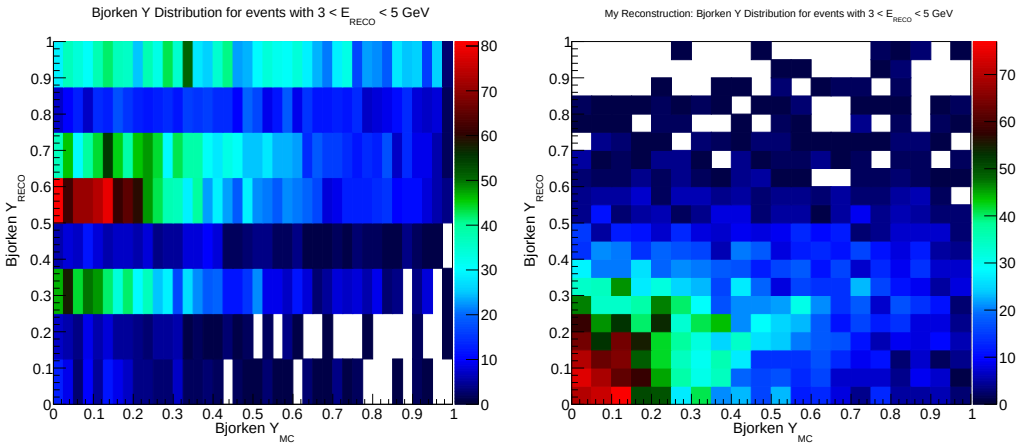

(a) Std Reconstruction (b) My Reconstruction

Figure 5.26: Reconstructed vs Monte Carlo Bjorken Y for events with reconstructed energy between 3-5 GeV, both for the standard and my reconstruction.

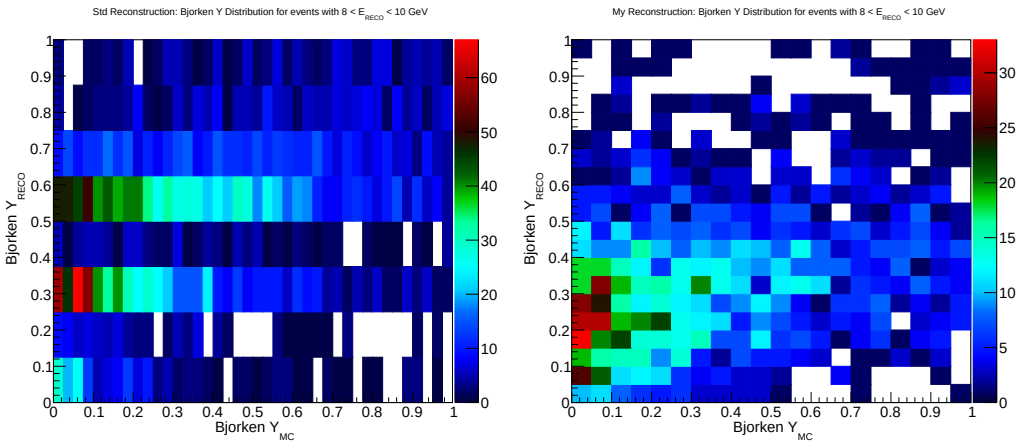

(a) Std Reconstruction (b) My Reconstruction

Figure 5.27: Reconstructed vs Monte Carlo Bjorken Y for events with reconstructed energy between 8-10 GeV, both for the standard and my reconstruction.

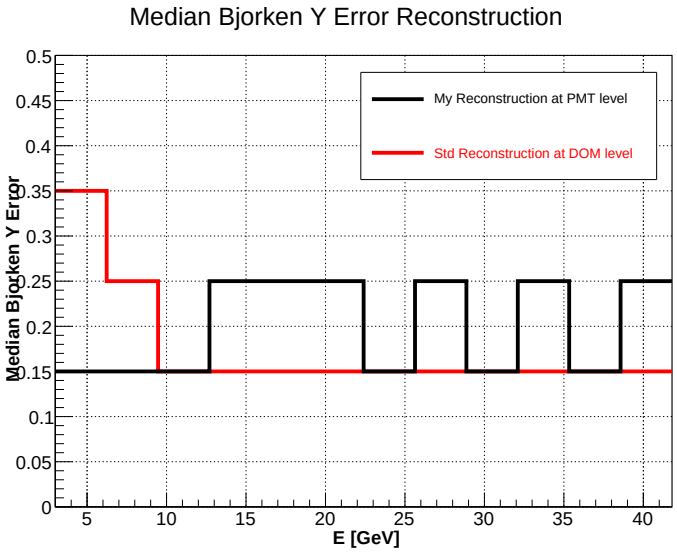

Figure 5.28: Median Bjorken Y reconstruction error.

but it arises naturally from the fit. Actually, **now that I have a reasonable Bjorken Y information, I could also apply the same energy correction used in the Standard Reconstruction**. This is something that has to be done in the future.
Finally, this step is extremely fast: it takes ~ 0.08 seconds for event since the minimiser moves in a lower number of dimensions and the considered D_{max} is set to 50 m.

5.5 Conclusions

As a conclusion, the shower reconstruction algorithm I developed for the ORCA detector, by using a completely new approach, demonstrates to have a good potential, especially for the energy and Bjorken Y variables for which it seems to behave better than the Standard Reconstruction in the energy range crucial for ORCA to make the Neutrino Mass Ordering Analysis, which is its main goal. Moreover, I plan to make further tests and studies about this in the near future, hence it is possible that the current performances could be improved.

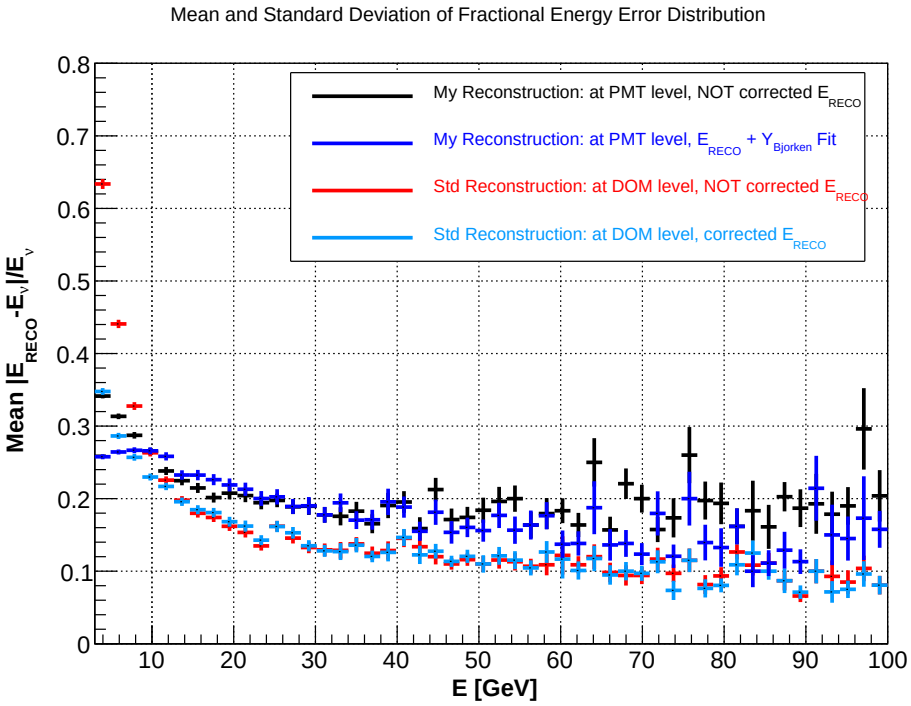

Figure 5.29: Mean fractional energy error. This plot is the same as Fig. 5.17 but it now includes my reconstructed energy after the Bjorken Y fit (blue points).

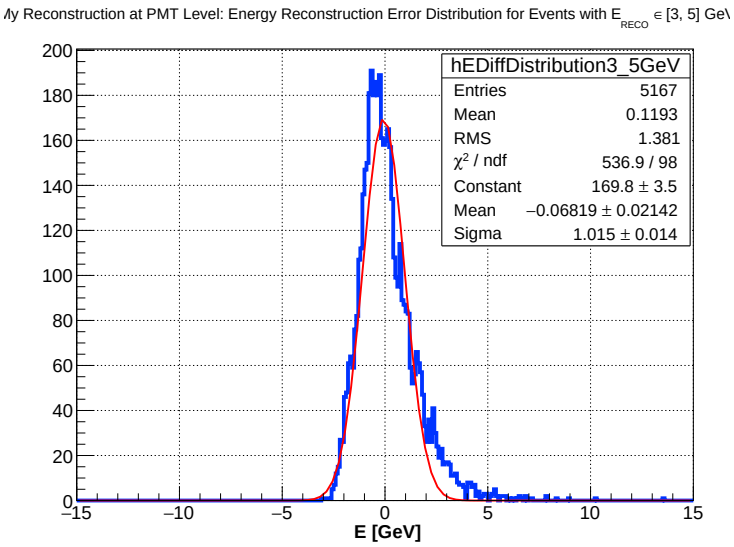

Figure 5.30: Energy error distribution, after the Bjorken Y fit, for events with reconstructed energy between 3-5 GeV, to be compared with Fig. 5.18.

Chapter 6

Sterile Neutrino Analysis with KM3NeT/ORCA and ANTARES

In this chapter I will describe the sterile neutrino analysis I have performed with ANTARES and KM3NeT/ORCA. Initially, my thesis was only focused on ORCA and the ANTARES analysis had already been started by another PhD student who left the collaboration before completing it, hence I took over it. This is to clarify that the first part of the ANTARES analysis, i.e. the one regarding Monte Carlo, has not been performed by me, but here I will briefly introduce it to clarify the final analysis made with real data for which I have contributed. This work is part of the paper JHEP06(2019)113, published this year.
In the case of ORCA, instead, since we do not yet have the full detector completed, I performed the analysis only with Monte Carlo, i.e. it is a sensitivity study. A paper about this analysis for ORCA is being prepared.
Since while I was doing the sterile analysis I was developing in parallel the shower reconstruction algorithm described in the previous Chapter and the latest full ORCA Monte Carlo simulation with 23 m horizontal spacing (which is the one I used in my analysis) is from the beginning of 2018 and in that period my reconstruction was not yet ready, the shower reconstruction used in this analysis is the standard one, known as *Dusj* [68].
Here I will firstly introduce the ANTARES analysis, then I will focus on the ORCA one.

6.1 ANTARES

The ANTARES neutrino telescope has an energy threshold of $\sim$ 20 GeV. This allows to look for the existence of a light sterile neutrino, as for the anomalies cases described in Chapter 1.

6.1.1 Data and Monte Carlo Samples

ANTARES data collected from 2007 to 2016 have been considered in the analysis for a total of 2830 days of live time. The aim of the MC production is to reproduce in the most realistic way the events expected at the detector, as well as the response of the apparatus when recording these events. In order to account for changes of the environmental conditions, as well as for the different operational status of the detector and its components over time, a run-by- run MC approach is applied [75]. A typical run lasts few hours. Several time dependent conditions are taken from real data and applied to the run-by-run MC. First, temporarily or permanently non-operational OMs are masked in the simulation. Secondly, background light conditions, which might vary due to bioluminescence, are measured every 104 ms for each individual OM. These samples are directly used as input for the background light simulation. Thirdly, individual OM efficiencies are considered, as calculated on an approximately weekly basis from ^{40}K coincidence rates [62]. Finally, the acoustics based position calibration, performed every few minutes, is applied. All these detailed inputs assure an authentic description of the detector response for each individual run. Remaining uncertainties are small and can be handled as global parameters which are discussed below. They are included in the analysis as systematic uncertainties.
Neutrino interactions of all flavours have been simulated with the GENHEN [76] package, developed inside the ANTARES Collaboration. It allows to reproduce neutrino interactions in the GeV to multi-PeV energy range. MC neutrino events can be weighted to reproduce different physical expectations. For atmospheric neutrinos with $E_\nu \in [20 - 100]$ GeV, a MC sample almost three hundreds times larger than the data sample is available. The model by Honda et al. [77] for the Frejus site is used in this work.
Even though the sub-marine location of ANTARES provides a good shielding against atmospheric muons, still a large amount of them will reach the detector. The event generator used in ANTARES to simulate atmospheric muons is MUPAGE [85]; the energy and angular distributions, as well as the multiplicity of muons propagating in sea water are parameterised. The contribution from this background is also evaluated from the data itself.

Particle propagation and Cherenkov light production are simulated using a GEANT based [78] package [76], which takes into account all relevant physics processes and computes the probability that photons emitted by a particle reach the OM surface, producing a hit. Finally the detector response is simulated, including the digitisation and filtering of hits. At this stage a realistic optical noise is added on each OM for each data acquisition run of the detector, and the time evolution of the detector configuration is accounted for as described above.

6.1.2 Event Reconstruction

The event reconstruction and selection used in the analysis have been optimised to select track-like events. Showers are instead considered as an additional source of background for this study.
Events have been reconstructed using two different algorithms, described in detail in ([79],[80]). In the following discussion these algorithms will be referred to as method A and method B, respectively. Both are optimised for events induced by GeV-scale ν_μ CC interactions. In method A a hit selection, based on time and spatial coincidences of hits, is applied and a χ^2-fit is performed in order to find the best track. Events can have a single-line topology (SL), if all the selected hits have been recorded in the same detector line, or a multi-line topology (ML), when hits belong to OMs of different lines. Method B consists of a chain of fits, aimed to improve at each step the track estimation. Starting from a hit selection, a first prefit, based on a directional scan with a large number of isotropically distributed directions, is performed. The best 9 directions are used as starting points for the final likelihood (log L) fit.
Once the muon track has been reconstructed, its length, L_μ, is computed. This is done, for ML events, by projecting back to the track the first and last selected hit. For SL events, since a vertex estimation is not possible due to the lack of azimuth information, the track length is estimated from the z-coordinates of the uppermost and lowermost storey which have recorded the selected hits and taking into account the reconstructed zenith angle.
The muon energy estimation is based on the fact that muons in the few-GeV energy range can be treated as minimum ionising particles, and their energy can be estimated from their track length L_μ:

$$E_{reco} = L_\mu \times 0.24 \text{ GeV/m} \tag{6.1}$$

where the factor 0.24GeV/m represents the energy loss of muons in sea water in the energy range of 10–100 GeV [2]. This quantity is used in the following

as estimator for the neutrino energy. The energy resolution of fully contained muons is dominated by the spacing of the detector elements and is found to be around 5 GeV. For muons leaving the detector only a lower limit for their energy can be derived, corresponding to their visible length inside the instrumented volume.

6.1.3 Analysis

To achieve the best sensitivity to the measurement of the oscillation parameters, a set of quality criteria has been applied. The selection of ν_μ CC events has been optimised by performing a preliminary Monte Carlo (MC) sensitivity study, before applying the whole analysis chain to data.
The main parameter on which the selection is based is the reduced χ^2 for method A and the log Likelihood [81] for method B. Events reconstructed by method A and passing the corresponding event selection are kept. The events discarded by this procedure are further reconstructed by method B; they are kept in the analysed sample if the corresponding selection criteria are passed. Only events which are reconstructed as up-going are used in the following. A minimum number of five storeys with selected hits is required, in order to minimise the background induced by atmospheric muons.
Fig. 6.1 shows the distribution of the reduced χ^2_{SL} for method A (SL) events where data are compared to simulated atmospheric neutrinos and background atmospheric muons. While the MC reproduces quite well the data in the signal region dominated by the neutrino signal, a disagreement between the MC expectation and data is visible for larger χ^2_{SL}. Both data and MC follow an exponential law in this region, but with different slopes. For this reason, the number of background atmospheric muons in the signal region has been determined from data itself.
The distribution in Fig. 6.1 has been parameterised in the region dominated by atmospheric muons ($\chi^2_{SL} > 0.8$) with four different exponential fits by varying the fit range. Each fit has been extrapolated into the signal region, and its corresponding integral has been computed. The mean of these integrals has been used to estimate the number of atmospheric muon background, and its uncertainty has been computed from the errors on the fitted function parameters. Summing up the results of this method for events that have been reconstructed by method A (SL and ML) and method B, and combining the corresponding errors in quadrature, a total background of 740 ± 120 atmospheric muons has been determined. This value is subsequently used as a Gaussian prior mean value and uncertainty in the minimisation procedure. The energy and direction distribution of the atmospheric muon background has been, instead, estimated directly from MC.

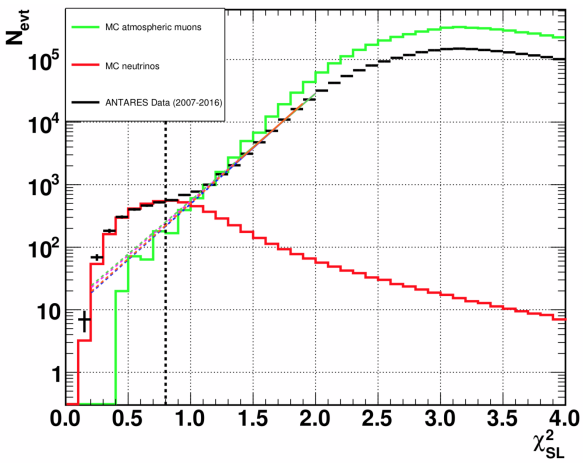

Figure 6.1: Distribution of reduced χ^2_{SL} values for events which have been reconstructed by method A (SL). Data (black crosses) with error bars indicating the statistical uncertainty are shown together with MC neutrino events (red line) and MC atmospheric muons (green line). The dashed black line at $\chi^2_{SL} = 0.8$ indicates the value of the applied cut on this parameter. The fitted functions used to estimate the background of atmospheric muons are shown as well (solid coloured lines), together with their extrapolation into the signal region left to the cut value (dashed coloured lines, see text for details)

After applying the event selection criteria described above on the data sample, a total of 7710 events have been selected, 1950 from method A (SL), 3682 from method A (ML) and 2078 from method B. In Fig. 6.2 the event distribution as a function of the logarithm of the reconstructed energy, $\log_{10}(\mathrm{E}_{reco}/\mathrm{GeV})$, and the cosine of the reconstructed zenith angle, $\cos\theta_{reco}$, is shown. The distribution of the MC expectation assuming no neutrino oscillation (left panel) is compared to what is observed in data (right panel). The final fit has been performed on the 2-dimensional histograms shown in Fig. 6.2. The fit follows a log-likelihood approach, by minimising the function:

$$-2\log L = 2\sum_{i,j}\left[N^{MC}_{i,j}(\bar{p},\bar{\eta}) - N^{data}_{i,j}\cdot N^{MC}_{i,j}(\bar{p},\bar{\eta})\right] + \sum_{k}\frac{(\eta_k - \langle\eta_k\rangle)^2}{\sigma^2_{\eta_k}} \quad (6.2)$$

where the first sum runs over the histogram bins of $\log_{10}(\mathrm{E}_{reco}/\mathrm{GeV})$ and $\cos\theta_{reco}$, $N^{data}_{i,j}$ the number of events in bin (i,j) and $N^{MC}_{i,j}(\bar{p},\bar{\eta})$ the corresponding number of expected MC events in the same bin. This number depends on the set of oscillation parameters, $\bar{p}$, that are under investigation,

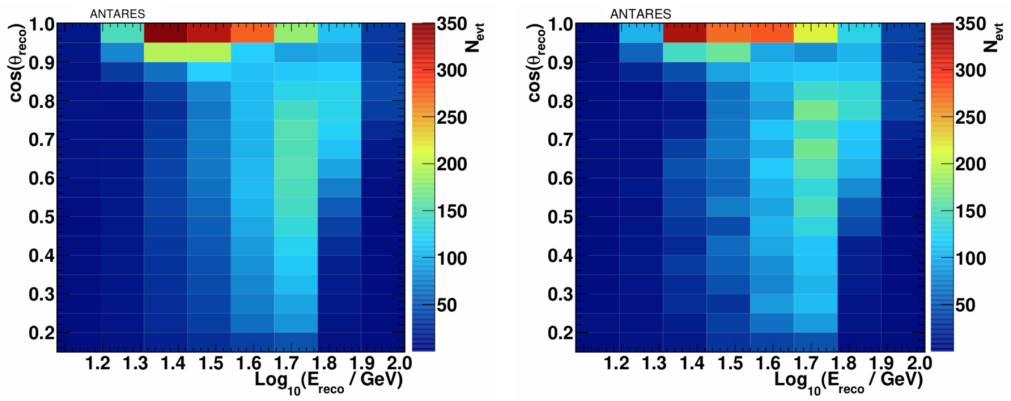

Figure 6.2: Number of selected MC events assuming no oscillation (left panel) and selected data (right panel), binned according to the logarithm of the reconstructed energy, $\log_{10}(\mathrm{E}_{reco}/\mathrm{GeV})$, and the reconstructed cosine of zenith, $\cos\theta_{reco}$. The first energy bin contains all events with $\log_{10}(\mathrm{E}_{reco}/\mathrm{GeV}) < 1.2$.

as well as on the set of parameters related to systematic uncertainties, $\bar{\eta}$, as described in the next subsections. The dependency on oscillation parameters is taken into acount for CC interactions of all neutrino flavours which contribute to the final event sample. The second sum runs over the number of nuisance parameters taken into account, $\langle\eta_k\rangle$ being the assumed prior of the parameter k, and σ_{η_k} its uncertainty. The log-likelihood function converges to the standard χ^2 for bins with high statistics. For bins with a small number of entries the log-likelihood is more adequate.

6.1.4 Systematics

The list of systematics used in this analysis is shown in Tab. 6.1. Three systematics are related to the atmospheric neutrino flux. A global neutrino normalisation factor, n_ν, which is left unconstrained during the fit, accounts for uncertainties on the total number of expected events. A variation $\Delta\gamma$ in the nominal neutrino flux spectral index has been used as additional nuisance parameter. Uncertainties on the neutrino/anti-neutrino flux ratio, $\nu/\bar{\nu}$, and on the flux asymmetry between up-going and horizontal neutrinos, ν_{up}/ν_{hor}, have also been taken into account. These uncertainties [49] have been parametrised by the IceCube Collaboration [86]. Such parameterisations compute a correction on the number of expected events as a function of the neutrino energy, flavour, chirality, direction and the value of the uncertainty on the flux ratio. The two ratios considered in this analysis have been found to be strongly correlated, thus a unique nuisance parameter is

Parameter	Prior	Fit NO	Fit IO
θ_{24} [°]	none	$1.5^{+2.0}_{-5.0}$	$1.5^{+2.0}_{-5.0}$
θ_{34} [°]	none	$25.9^{+5.1}_{-4.2}$	$25.9^{+5.1}_{-4.2}$
δ_{24} [°]	none	180 ± 71	0 ± 72
n_ν	none	$0.84^{+0.10}_{-0.09}$	$0.84^{+0.10}_{-0.09}$
$\nu/\bar{\nu}$ [σ]	0.0 ± 1.0	$1.07^{+0.63}_{-0.55}$	$1.07^{+0.63}_{-0.55}$
$\Delta\gamma$	0.00 ± 0.05	-0.011 ± 0.036	-0.011 ± 0.036
Δm^2_{23} [$10^{-3}\,\mathrm{eV}^2$]	none	$3.0^{+0.8}_{-0.6}$	$3.0^{+0.8}_{-0.6}$
θ_{23} [°]	none	52 ± 8	52 ± 8
θ_{13} [°]	8.41 ± 0.28	8.41 ± 0.28	8.41 ± 0.28
M_A [σ]	0.0 ± 1.0	$0.11^{+0.93}_{-0.97}$	$0.11^{+0.93}_{-0.97}$

Table 6.1: Set of priors used for the ANTARES sterile neutrino analysis. The two columns on the right show the result of the fitted values in the case of normal ordering (NO) and inverted ordering (IO).

considered in the fit.
An additional source of systematic uncertainty is the limited knowledge of the neutrino interaction model. At the energy of interest for this study, the cross section is dominated by deep inelastic scattering (DIS), with a smaller contribution from quasi elastic (QE) and resonant (RES) scattering. Uncertainties in the DIS cross section can be incorporated in the global flux normalisation factor n_ν, as well as in the correction to the spectral index $\Delta\gamma$.
For what concerns the QE and RES processes, dedicated studies have been performed with gSeaGen [83], which uses GENIE [82] to model neutrino interactions. The dominant systematic is found to be related to the axial mass for CC resonance neutrino production, M_A. Its default value is 1.12 ± 0.22 GeV [82]. By varying this parameter by $\pm 1\sigma$, the correction with respect to the expected number of events has been computed as a function of the true neutrino energy and this parameterisation is used in the final fit.
Since the effect of a sterile neutrino would modify the oscillation pattern in a similar way as Δm^2_{23} and θ_{23} do, these parameters are considered to be one of the sources of systematic uncertainty for this analysis. Both Δm^2_{23} and θ_{23} are left unconstrained as recommended in [87]. θ_{13} is left free in the fit but treated with a Gaussian prior at $\theta_{13} = (8.41 \pm 0.28)°$, which is taken from a

global fit [88] as well as the values of the solar neutrino parameters, which are kept fixed: $\Delta m^2_{12} = 7.37 \times 10^{-5}$ eV^2 and $\sin^2\theta_{12} = 0.297$. Different values of δ_{CP} have been tested at the stage of the MC sensitivity study and found to have no impact on the final result. Therefore δ_{CP} is fixed at zero.
The number of atmospheric muons, N_μ, contaminating the neutrino sample, is treated as an additional nuisance parameter. Its value and uncertainty, determined with the data-driven technique, are used as a prior.
Finally, detector and sea water related systematics have been studied as well. Dedicated MC simulations have been generated with modified OM photon detection efficiencies and a modified water absorption length, assuming a variation of $\pm 10\%$ from the nominal value, but keeping the same wavelength dependence. The overall OM efficiency can be easily adjusted to the measured coincidence rates from ^{40}K decays [62] which makes the chosen 10% variations a conservative benchmark value, in line with early studies performed on ANTARES OMs [89]. The water absorption length had been measured several times at the ANTARES site [90]. The different measurements, taken at two different wavelengths, vary within about 10%.
As discussed in section 2.4, the addition of a sterile neutrino in the model implies six new mixing parameters to be accounted for. The mixing angle θ_{14} and its associated phase δ_{14} have been fixed at zero, since they mainly affect the ν_e channel. The fast oscillations due to $\Delta m^2_{14} \geq 0.5$ eV^2 are unobservable due to the limited energy resolution of the detector, making Δm^2_{14} not measurable. It has been kept fixed at 0.5 eV^2. The choice of the neutrino mass hierarchy (NMH) as well as δ_{24} are expected to impact the result. Therefore both normal and inverted ordering (NO/IO) and various values of δ_{24} have been tested during the fit. Furthermore, to ensure the stability of the fit procedure, the atmospheric muon contamination has been fixed at the value found by the standard oscillation analysis. It has been verified that this choice does not lead to better constraints with respect to the case of a free muon contamination.

6.1.5 Result on θ_{24} and θ_{34}

In table 6.1 the complete list of all the fitted parameters for the sterile oscillation analysis for NO and IO is shown, together with their best-fit values and their priors. While θ_{24} is found to be compatible with zero, the best fit for θ_{34} is found at a non-zero value. This can be understood if we look at Fig. 6.3. In shows the distribution of the ratio between the reconstructed energy and the cosine of the reconstructed zenith. This ratio is affected by the oscillation phenomenon as can be seen for the lowest values of $E_{reco}/\cos\theta_{reco}$. For comparison, also the distribution of MC assuming no neutrino oscillation, as

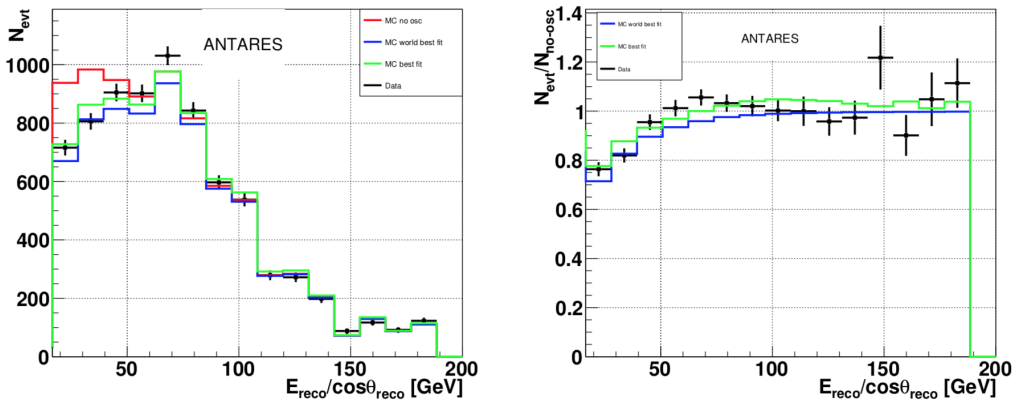

Figure 6.3: $E_{reco}/\cos\theta_{reco}$ distribution for data (black), MC without oscillation (red), MC assuming the world best-fit values (blue) [38] and MC assuming best-fit values of this analysis (green). The left plot shows event numbers while the right plot illustrates the event ratio with respect to the MC without oscillations.

well as the one assuming the world best-fit values [91] are shown. The latter two are calculated with all nuisance parameters at their nominal values. Such a 1D distribution does not carry the full information exploited in the fit, which is performed on the 2D distribution shown in Fig. 6.2. **While compatible with world data, ANTARES results seem to prefer a somewhat shallower (or energy shifted) oscillation minimum.** This shallower oscillation dip can be easily provided by a non- zero value of $\sin\theta_{34}$. The non-sterile hypothesis is found at $-2\Delta\log L = 4.4$ which corresponds to a 2-parameter p-value of 11%. The complex phase δ_{24} is found at 180°. For IO instead the fit prefers $\delta_{24} = 0°$, with otherwise identical results, as expected from the degeneracy between NMO and δ_{24}. The best-fit value is found for Δm^2_{23} at $(2.0 + 0.4) \times 10^{-3}$ eV^2, which is compatible with the current world best-fit value [91]. The mixing angle θ_{23} is found to be compatible with maximal mixing within its error. The global normalisation factor for neutrinos, n_ν, is found to be 18% lower. This value is within the atmospheric neutrino flux uncertainties and it is compatible with what was reported by other analyses [49]. A non-negligible pull is found on $\nu/\bar{\nu}$. This parameter seems to compensate for the low value of n_ν: this has been derived from an alternative fit, for which all nuisance parameters but n_ν have been fixed, to allow a more direct comparison with the result reported in [92]. Under these conditions $n_\nu = 1.04 \pm 0.02$ is found. Concerning the spectral index correction, $\Delta\gamma$, no significant distortion from the nominal value is observed.

Exclusion contours are built by applying Wilks' theorem [81]. In figure 6.4 the resulting 90% and 99% CL exclusion limits have been computed on a 2D grid in the plane of the two matrix elements, namely $|U_{\mu 4}|^2 = \sin^2\theta_{24}$ and $|U_{\tau 4}|^2 = \sin^2\theta_{34}\cos^2\theta_{24}$. In section 2.4 we have seen that there is a degeneracy between δ_{24} and the neutrino mass ordering. This degeneracy is broken for $E_\nu < 10$ GeV due to matter effects but it remains valid above 10 GeV, which is quite belo the ANTARES energy threshold. Hence, the exclusion limit for unconstrained δ_{24}, which corresponds to both [NO,$\delta_{24} = 180°$] or [IO,$\delta_{24} = 0°$], can be directly compared to the IceCube/DeepCore [15] (IO) limit. Also shown are limits for NO and $\delta_{CP} = 0°$ which allow a direct comparison with the results from IceCube/DeepCore [15] (NO) and Super-Kamiokande [93]. All three experiments find the best fit for $|U_{\tau 4}|^2$ to differ from zero. Our results exclude regions of the parameter space not yet excluded by other experiments.
The IceCube/DeepCore analysis [15] is limited to events with reconstructed energy lower than 56 GeV, while the distortion on the oscillation pattern possibly produced by the presence of a sterile neutrino would be evident also at higher reconstructed energies. The present analysis includes events with reconstructed energy up to 100 GeV. It has been verified that the ANTARES limits degrade when restricting the analysis to events with Ereco < 56 GeV. In this work both of the standard atmospheric oscillation parameters Δn^2_{23} and $\sin^2(2\theta_{23})$ are left unconstrained in line with the IceCube/DeepCore analysis [15].
After profiling over the other variable, the following limits on the two matrix elements can be derived:

$$|U_{\mu 4}|^2 < 0.007\,(0.13) \text{ at } 90\%\,(99\%)\text{ CL}, \tag{6.3}$$
$$|U_{\tau 4}|^2 < 0.40\,(0.68) \text{ at } 90\%\,(99\%)\text{ CL}. \tag{6.4}$$

As a conclusion, ANTARES data exclude values of the parameter space not yet excluded by other experiments.

6.2 KM3NeT/ORCA

It is possible to perform the same analysis also with ORCA. However, since we do not have yet the full detector, we can only make a sensitivity study by using Monte Carlo. Hence, before describing the analysis and the results, the ORCA MC chain will be briefly introduced.

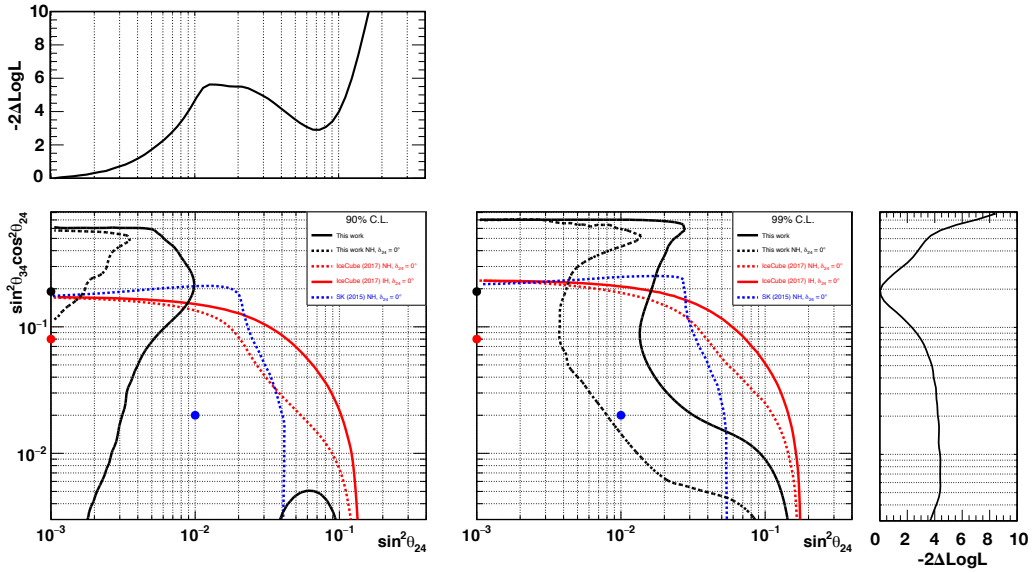

Figure 6.4: 90% (left) and 99% (right) CL limits for the 3+1 neutrino model in the parameter plane of θ_{24} and θ_{34} obtained in this work (black lines), and compared to the ones published by IceCube/DeepCore [15] (red) and Super-Kamiokande [93] (blue). The dashed lines are obtained for NO and $\delta_{24} = 0°$ while the solid lines are for an unconstrained δ_{24} (this work) or for IO and $\delta_{24} = 0°$ (IceCube/Deepcore) respectively. The colored markers indicate the best-fit values for each experiment. The 1D projections after profiling over the other variable are also shown for the result of this work.

6.2.1 KM3NeT/ORCA Simulation Chain

The ORCA simulation chain is shown in Fig. 6.5.
The first step of the Monte Carlo simulation is neutrino propagation and interaction. In particular, neutrino and antineutrino induced interactions in sea water in the energy range from 1 to 100GeV have been generated with a software package, called gSeaGen based on the widely used GENIE neutrino event generator. In this step of the simulation chain, a volume surrounding the instrumented volume, called "can", is defined. The can volume is a cylinder with height and radius exceeding the instrumented volume by about 3 absorption lengths (where the absorption length is 70 m) but bounded by the sea bed from which the light can not emerge.
All particles emerging from a neutrino interaction vertex are propagated with KM3SIM, a full photon tracking simulation, based on Geant4, originally part of the HOURS package [84]. KM3SIM generates Cherenkov light from primary and secondary particles and simulates the detection of photons (hits)

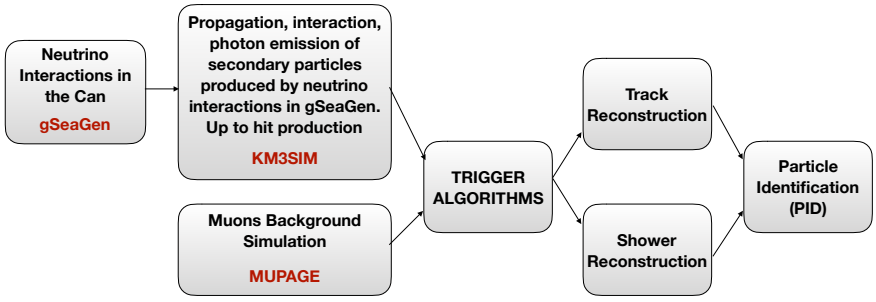

Figure 6.5: Representation of the ORCA simulation chain.

while taking into account the light absorption and scattering in water as well as the DOM and PMT characteristics. The background due to down-going atmospheric muons is generated with MUPAGE [85]. The second type of background to be taken into account are the randomly distributed PMT hits due to the Cherenkov light from electrons induced by decays of ^{40}K. In this case, single photo-electron hits can be added to the hits induced by charged particles inside a chosen time window. Also the hits in coincidence due to ^{40}K between two PMTs inside the same DOM are taken into account. An uncorrelated hit rate of 10 kHz per PMT was added.
Due to the amount of background it is not possible to save all the data taken by the telescope, therefore trigger algorithms are applied and only the data passing the triggers are saved to disk. Here, reconstruction algorithms are run on the data and the output information from the reconstruction are used to distinguish between the 2 event typologies observed in neutrino telescopes: tracks, those that are induced by CC muon neutrino interactions, having the signature of a straight track passing through or nearby the instrumented volume, and showers, those coming from all other neutrino interaction channels and flavours: all NC interactions and the CC interactions of electron and tau neutrinos.
The reconstructions information is given to the ORCA particle identification (PID), which uses the random decision forest (RDF) technique. In the forest a set of random decision trees is trained on a randomly drawn fraction of all training variables. The output score then reflects the fraction of trees that voted for the predicted class. In ORCA, only binary decision forests are used, which have to decide between two classes. In this way, a tunable output parameter is obtained, which can be used to cut on in the analysis.

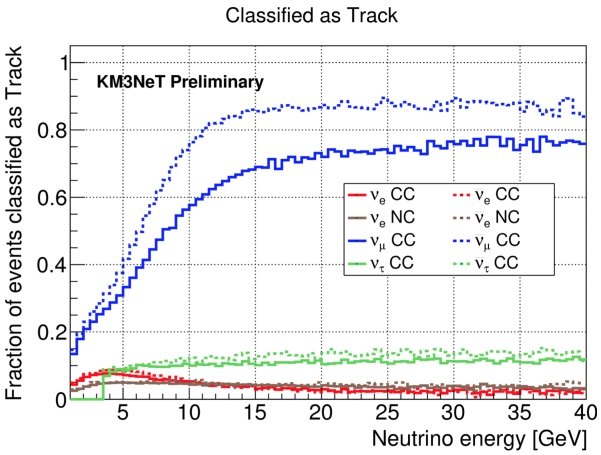

Figure 6.6: PID performances for ORCA.

The output tuples all contain 3 different types of classifiers: two to deselect background

1. atmospheric muon vs. neutrino decision: to reject atmospheric muons,

2. pure noise vs. neutrino event decision: to deselect events that appear very noise-like in the detector,

one for physics

1. track vs. shower decision: to split the sample in 2 or more classes, tracks and showers.

Fig. 6.6 shows the performances of the PID for ORCA as a function of the neutrino energy E_ν.
For low E_ν the primary lepton produced by the CC interaction takes the majority of neutrino energy but since it is small, the track induced by a low energy muon is more difficult to distinguish from a shower, this is why the PID performances drop for low energies. For higher neutrino energies instead, the hadronic shower produced in each interaction starts to take a bigger fraction of E_ν with respect to the primary lepton, which, in the case of a muon, creates a track that in a fraction of the cases is not long enough to be well distinguished from the hadronic shower. This is why the classification efficiency is not exactly 1.
The simulated ORCA detector used in the analysis presented here corresponds to one building block of 115 detection units with 18 DOMs each.

6.2.2 Modeling the Detector Response

All the MC information described in the previous section are put together to build the ORCA multidimensional response matrix.
If we denote as x the ensemble of true characteristics for a neutrino event (e.g. its true energy and direction), and x' the measured characteristics (reconstruction, classification), if we build an histogram of the measured events, the predicted event count in a bin of the variables x' is obtained as [95]:

$$n_{reco}(x') = \sum_{x} R(x, x') \times n_{int}(x) \tag{6.5}$$

where $R(x, x')$ represents the conditional probability for an event occurring in true bin x to be detected, successfully reconstructed, selected and classified in the bin of measured characteristics x'. This way, R incorporates the totality of the effects related both to the detector and to the experimenter's methodology [95].
After all the MC has been performed, an event is selected if it satisfies at least one of the "good track" or "good shower" conditions, that means it satisfies the quality cuts, needed to reject both atmospheric muons and pure noise events, and it is reconstructed as upgoing by the reconstruction algorithms, needed to reject atmospheric muons.
As seen in the previous section, PID classifiers provide two anti-background classification scores $p_{bkg,noise}$ and $p_{bkg,\mu}$ as well as one track/shower classification score p_{track} for each event. In the standard analysis strategy, the definition of event classes proceeds by cutting first on $p_{bkg,noise}$ and $p_{bkg,\mu}$ so as to reject background and then forming two event classes out of the remaining events: 'track-like' and 'shower-like', defined by a single cut p_{cut} on the track/shower score:

- Events classified as track if $p_{track} > p_{cut}$
- Events classified as shower if $p_{track} \leq p_{cut}$

Different values of p_{cut} have been tried to optimize the sterile neutrino analysis and $p_{cut} = 0.6$ has been finally selected.
Once the events have been selected, we can finally define the multidimensional detector response matrix:

$$R^{[\nu_x \to i]}(E, \theta, y, E', \theta', y') = \frac{N_{sel}^{MC}[\nu_x \to i](E, \theta, y, E', \theta', y')}{N_{gen}^{MC}[\nu_x](E, \theta, y)} \tag{6.6}$$

where ν_x is the interaction channel, i represents the classification, N_{sel}^{MC} is the number of selected events (i.e. after reconstruction, PID and cuts), and

N_{gen}^{MC} is the number of generated true events.
However, due to the limited MC statistics available in some channels, the response matrix entries can show bin-to-bin fluctuations which do not stem from any physical effect but are instead purely due to statistical fluctuations in the Monte Carlo sampling [95]. Using such sparsely sampled response matrix can result in drastic overestimations of sensitivity [96], an effect we will refer to as the 'sparse Monte Carlo effect'.
One way to get rid of the MC sparseness is the **uncorrelated smearing** [96], i.e. the use of sets of *smearing histograms*, which typically separate (decorrelate) the response of the detector for each measured variable. In particular, in the ORCA analyses the uncorrelated smearing model removes correlations between reconstructed variables, but the dependence of the smearing functions on all true variables are kept [95].

6.2.3 Events and Signed χ^2 Distributions

Once all the information from the previous steps has been put together, the sensitivity to sterile neutrinos can be studied through the distribution of events and χ^2 values as a function of energy and zenith angle for different sterile parameter values. For illustration purposes, we define a signed-χ^2 variable, where:

$$\text{signed-}\chi^2 = \frac{(HP_{Sterile} - HP_{Standard})|HP_{Sterile} - HP_{Standard}|}{\sqrt{HP_{Standard}}} \tag{6.7}$$

being HP the hypothesis taken into account, as a function of reconstructed neutrino energy and cosine zenith for track-like and cascade-like events. With this definiton, the signed-χ^2 is conceptually related to the number of events, in the sense that positive (negative) values of χ^2 correspond to excess (defect) of events, but with a different weight. To give an idea, in Fig. 6.7 I show both the signed-χ^2 and the event distributions for tracks and showers in the case of a sterile neutrino with $\Delta m^2_{14} = 1$ eV^2 and $|U_{e4}| = 0.05$, $|U_{\mu 4}| = 0$, $|U_{\tau 4}| = 0$, Normal Ordering (NO). From it we can see that there is a net deficit of events both in tracks and in showers, and from the total χ^2 value we can see that in the case of only U_{e4} mixing, the shower channel is the most sensitive.
In Fig. 6.8 I show the signed χ^2 distribution assuming 3 years of ORCA data taking, $\Delta m^2_{14} = 1$ eV^2 and $|U_{e4}| = 0$, $|U_{\mu 4}| = 0.03$, $|U_{\tau 4}| = 0.1$. The overall χ^2 is also reported in top of the plots. From its value we can see that, in this scenario, the leading channel is track-like (Fig. 6.8 (a)), and that there is a significant excess of events expected at $E \sim 20 - 30$ GeV for upgoing neutrinos, and an overall deficit of events in other regions. This plot

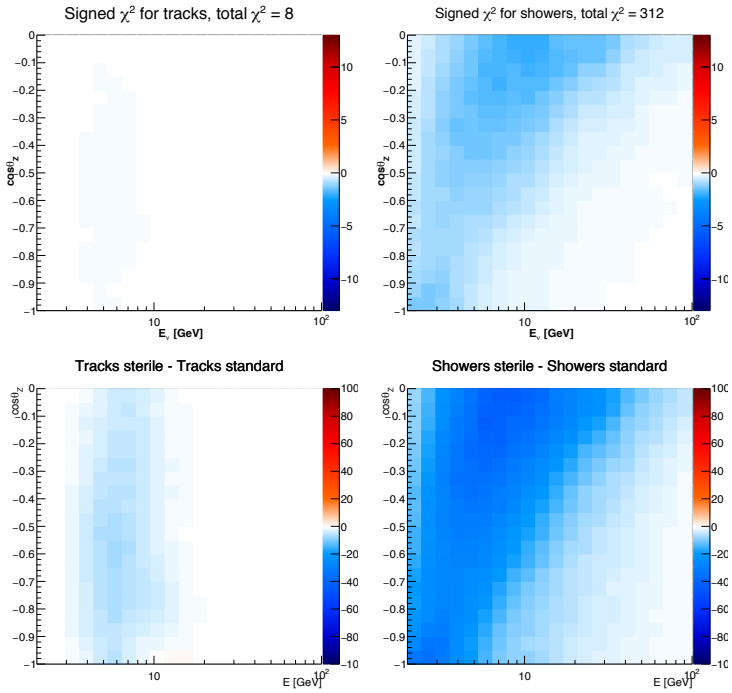

Figure 6.7: Signed χ^2 and events distributions for 3 years of full ORCA as a function of reconstructed energy and zenith angle for tracks (a) and showers (b) for $\Delta m^2_{14} = 1$ eV^2 and $|U_{e4}| = 0.05$, $|U_{\mu 4}| = 0$, $|U_{\tau 4}| = 0$, NO. The total χ^2 value is also reported for each plot.

is important for the sterile analysis of $|U_{\mu 4}|^2$ vs $|U_{\tau 4}|^2$ with fixed Δm^2_{14}. Fig. 6.9 instead, shows the same χ^2 distribution as Fig. 6.8 but assuming $\Delta m^2_{14} = 10^{-4}$ eV^2. Comparing them we can conclude that, for the low sterile mass case:

1. a much larger deficit of events is expected around 10 GeV,

2. the cascade channel importance is comparable with the track one,

3. the total χ^2 values are larger, i.e. ORCA is more sensitive to lower Δm^2_{14} values.

It is possible to make plots like this for all the other cases such as low sterile mass vs $|U_{e4}|$ or $|U_{\tau 4}|$ to see what we should expect for the ORCA sensitivity. These plots have also been crosschecked with 2D probability oscillograms since we should expect a similar result apart of some net effects due to detector resolution, binning and smearing.

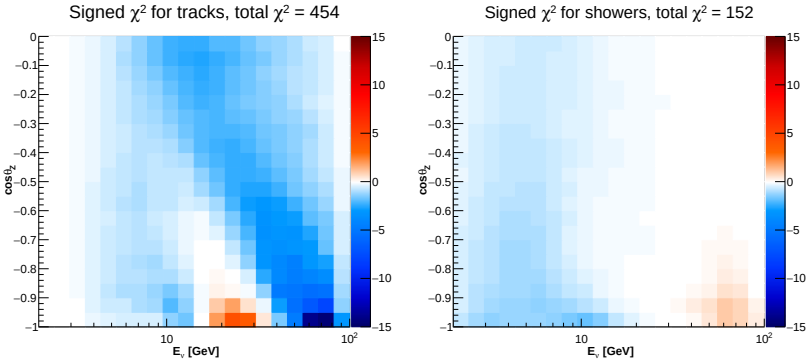

(a) (b)

Figure 6.8: Signed χ^2 for 3 years of full ORCA as a function of reconstructed energy and zenith angle for tracks (a) and showers (b) for $\Delta m^2_{14} = 1$ eV^2 and $|U_{e4}| = 0$, $|U_{\mu 4}| = 0.03$, $|U_{\tau 4}| = 0.1$. The total χ^2 value is also reported for each plot.

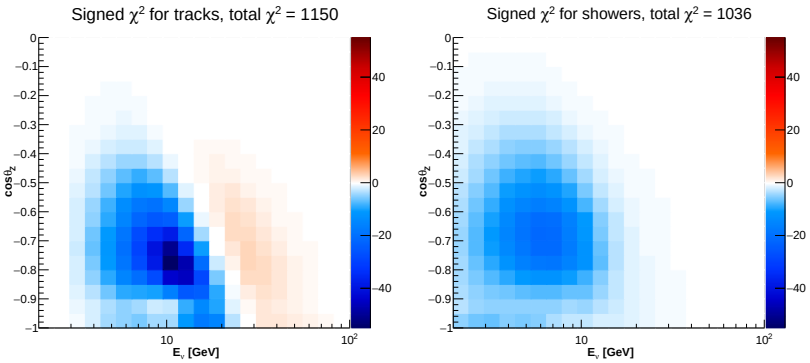

(a) (b)

Figure 6.9: Signed χ^2 for 3 years of full ORCA as a function of reconstructed energy and zenith angle for tracks (a) and showers (b) for $\Delta m^2_{14} = 10^{-4}$ eV^2 and $|U_{e4}| = 0$, $|U_{\mu 4}| = 0.03$, $|U_{\tau 4}| = 0.1$. The total χ^2 value is also reported for each plot.

Parameter	Prior
θ_{13} [°]	8.54 ± 0.15
Flux Norm	1 ± 0.10
NC Scale	1 ± 0.05
ν_μ/ν_e Skew	0 ± 0.05
$\nu/\bar{\nu}$ Skew	0 ± 0.10
Energy Slope	0 ± 0.05
Energy Scale	1 ± 0.03

Table 6.2: Set of priors used for the ORCA sterile neutrino analysis.

6.2.4 Systematics

Tab. 6.2 shows the set of systematics used for the ORCA sterile analysis, both for the "standard analysis", i.e. $|U_{\mu 4}|^2$ vs $|U_{\tau 4}|^2$ with fixed Δm^2_{14} and also for the low Δm^2_{14} analysis. All the oscillation parameters are set to NuFit v.3 values [94]. Initially I have also tried to put a lose prior on Δm^2_{13} of 2.49 ± 0.5 $[10^{-3}]$ eV^2. The motivation of this prior mainly comes from the degeneracy that appears when $\Delta m^2_{14} \sim \Delta m^2_{13}$ [16], hence I thought it would be helpful for the low sterile mass analysis I describe in Sec. 6.3. However, I found it to have a very small impact in the final result, so I decided to remove it.

6.2.5 Systematics on Earth Model

We have seen in Sec. 2.3 the different potentials that neutrinos feel while traveling through the Earth. In particular, Eq. 2.36 shows that with the ordinary matter whose Earth is composed only the electron and neutron densities, N_e and N_n, play a net role in neutrino interactions. They can be written, in terms of the matter density ρ and the Z/A value, as:

$$N_e \propto \rho Z/A \tag{6.8}$$
$$N_n \propto \rho(1 - Z/A) \tag{6.9}$$

Hence we need to know both ρ and Z/A for the different Earth layers traversed by neutrinos. For this, the ORCA sterile analysis uses the PREM model [41] to model the Earth parameters ρ and Z/A. Fig. 6.10 (a) shows the exact PREM model used in the analysis: it shows the assumed matter density ρ in function of the distance from the Earth Centre.
During the analysis it was possible to free the value of Z/A for the Earth

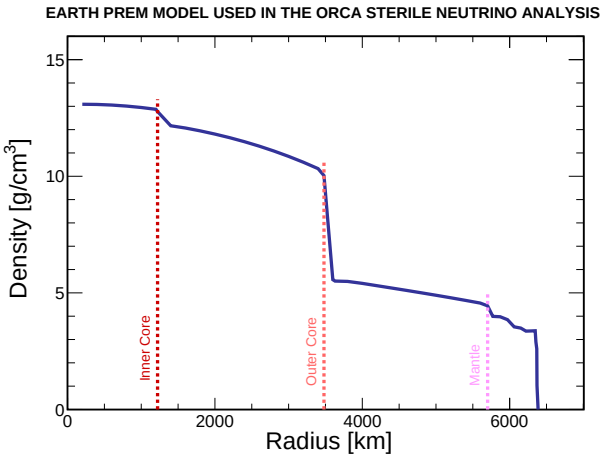

Figure 6.10: Earth model (PREM [41]) used in the ORCA sterile neutrino analysis.

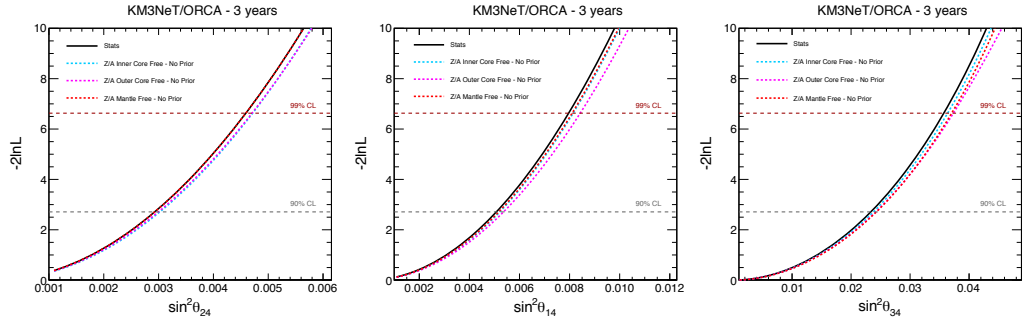

Figure 6.11: Impact of the uncertainties on the Earth Z/A values separately for inner core, outer core and mantle.

inner core, outer core and mantle. And this would mean to have 3 free more parameters in the analysis, which is already time consuming. Hence, I decided to **fix** the values of Z/A in the analysis. However I made some studies of the impact of freeing Z/A: to assess the impact of uncertainties on the inner Earth density or chemical composition, I let the Z/A value vary in the fit, independently for each of the three innermost chemical layers (lower mantle, outer core and inner core). I did not put any prior because I wanted to assess the worst scenario. The individual impact of each modeled systematic effect are considered separately. This approach is motivated by the observation that when systematics and priors are added incrementally to the set of nuisance parameters, their apparent impact is very much dependent on the order of addition, so that the evaluation of their relative effects is difficult [95].

The Z/A uncertainties are found to have a modest impact. Note that here only uniform variations of Z/A in a layer were applied, while the overall radius and density profile of each chemical layer was kept fixed.
Fig. 6.11 shows the impact of freeing separately Z/A of inner core, outer core and mantle, without constraints for the case of a fixed $\Delta m^2_{14} = 0.3$ eV^2 for each of the three sterile-active mixing angles; when a mixing angle is considered, the other 2 sterile mixing angles are fixed to 0. The Earth uncertainties appear to have a quite negligible impact in the sterile analysis, especially for θ_{24}. In particular, we can see that the outer core is the more impactive region. This fact can be understood if we look at Fig. 6.8: it appears that for $\Delta m^2_{14} > 0.1$ eV^2 the main contribution is given from events with $\cos\theta_{ZENITH} \in -[0.8, 1]$. This is exactly the core region, in fact, the inner core $\in -[0.981, 1]$ and the outer core $\in -[0.837, 0.981]$ [95]. Hence we should expect that a systematic on the core is more impactive than a systematic on the mantle in this case. The reason why the inner core impact is negligible with respect to the outer core is that ORCA has a negligible sensitivity to the inner core density, as it is expected considering that the corresponding solid angle is at the limit of the ORCA resolution.

6.2.6 Impact of a Sterile Neutrino on NC Events

Differently from the mass ordering analysis ([95],[97]), for which the $V_{matter,CC}$ of neutrinos with electrons gives the leading contribution, in the sterile analysis case also the $V_{matter,NC}$ to be important. In this sense we can look at only the NC events we expect to see with ORCA. Intuitively, if there is mixing into a sterile neutrino, less events will participate to the NC interactions and this means that we should expect **less** NC events with respect to the standard 3 neutrinos scenario.
Fig. 6.12 shows the difference between tracks (a) and showers (b) between the standard 3 neutrinos hypothesis and the one assuming a sterile neutrino. From both (a) and (b) we see that $Events_{NC,3\nu} - Events_{NC,4\nu} > 0$ which confirms our expectations. Hence we can conclude that, differently from the mass ordering analysis, in the sterile neutrino analysis also NC events contribute to the final sensitivity estimation.

6.2.7 The Asimov Approach

In general, when we want to characterize the sensitivity of an experiment by reporting the expected (e.g., mean or median) significance for a specific data set we typically make use of Monte Carlo calculations that are computationally expensive. There are however approximate methods by which one can

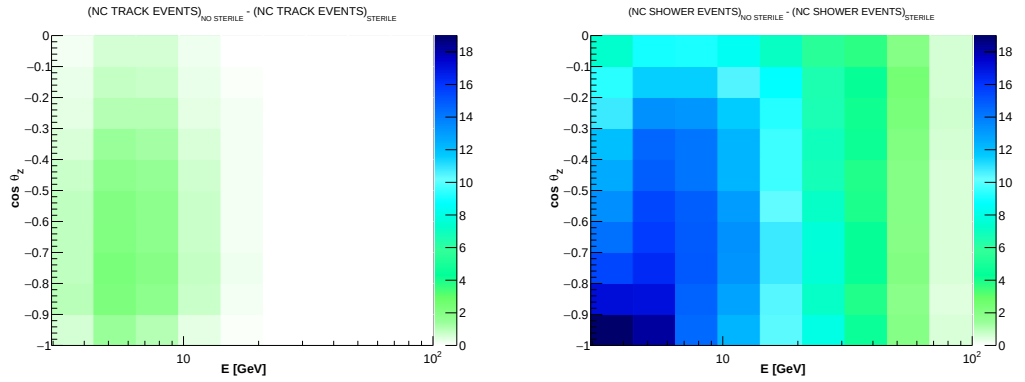

(a) (b)

Figure 6.12: Difference in Neutral Current (NC) events reconstructed as tracks (a) and showers (b) between the standard case (3-ν scenario) and the case with one neutrino with $\Delta m^2_{14} = 0.3$ eV^2, $|U_{e4}|^2 = 0$, $|U_{\mu 4}|^2 = 0.02$, $|U_{\tau 4}|^2 = 0.05$, 3 years of assumed data taking with ORCA.

obtain both the significance for given data as well as the full sampling distribution of the significance under the hypothesis of different signal models, all without recourse to Monte Carlo [98]. In this way one can find, for example, the median significance and also a measure of how much one would expect this to vary as a result of statistical fluctuations in the data. This is done by the Asimov dataset approach, which is the method I used for the ORCA sterile neutrino analysis.

A useful element of the method involves estimation of the median significance by replacing the ensemble of simulated data sets by a single representative one, referred to here as the "Asimov" data set. It is interesting to know that the name Asimov data set is inspired by the short story Franchise, by Isaac Asimov, in which elections are held by selecting the single most representative voter to replace the entire electorate [98].

For purposes of discovering a new signal process, one defines the null hypothesis, H0, as describing only known processes, here designated as background. This is to be tested against the alternative H1, which includes both background as well as the signal. When setting limits, the model with signal plus background plays the role of H0, which is tested against the background-only hypothesis, H1.

To summarize the outcome of such a search one quantifies the level of agreement of the observed data with a given hypothesis H by computing a p-value, i.e., a probability, under assumption of H, of finding data of equal or greater incompatibility with the predictions of H. The measure of incompatibility can

be based, for example, on the number of events found in designated regions of certain distributions or on the corresponding likelihood ratio for signal and background. One can regard the hypothesis as excluded if its p-value is observed below a specified threshold.
Then the p-value can be converted into an equivalent significance, Z. It is often useful to quantify the sensitivity of an experiment by reporting the expected significance one would obtain with a given measurement under the assumption of various hypotheses. A widely used procedure to establish discovery (or exclusion) in particle physics is based on a frequentist significance test using a likelihood ratio as a test statistic. In addition to parameters of interest such as the rate (cross section) of the signal process, the signal and background models will contain in general nuisance parameters whose values are not taken as known a priori but rather must be fitted from the data. The additional flexibility introduced to parametrize systematic effects results, as it should, in a loss in sensitivity [98].
To illustrate the use of the profile likelihood ratio, consider an experiment where for each selected event one measures the values of certain variables (e.g. energy and direction), and thus the resulting data can be represented as one or more histograms. Suppose for each event in the signal sample one measures a variable x and uses these values to construct a histogram $\mathbf{n} = (\mathrm{n}_1, \ldots, \mathrm{n}_N)$. The expectation value of n_i can be written [98]:

$$E[n_i] = \mu s_i + b_i \tag{6.10}$$

where the mean number of entries in the i-th bin from signal and background are

$$s_i = s_{tot} \int_{bini} f_s(x;\theta_s)dx, \tag{6.11}$$

$$b_i = b_{tot} \int_{bini} f_b(x;\theta_b)dx. \tag{6.12}$$

Here the parameter μ determines the strength of the signal process, with $\mu = 0$ corresponding to the background-only hypothesis and $\mu = 1$ being the nominal signal hypothesis. The functions $f_s(x;\theta_s)$ and $f_b(x;\theta_b)$ are the probability density functions (pdfs) of the variable x for signal and background events, and θ_s and θ_b represent parameters that characterize the shapes of pdfs. The quantities s_{tot} and b_{tot} are the total mean numbers of signal and background events, and the integrals in 6.11 and 6.12 represent the probabilities for an event to be found in bin i. Below we will use $\theta = (\theta_s, \theta_s, b_{tot})$ to denote all of the nuisance parameters.
In addition to the measured histogram n one often makes further subsidiary measurements that help constrain the nuisance parameters. For example, one

may select a control sample where one expects mainly background events and from them construct a histogram of some chosen kinematic variable. This then gives a set of values $m = (m_1, ..., m_M)$ for the number of entries in each of the M bins. The expectation value of m_i can be written

$$E[m_i] = u_i(\theta) \tag{6.13}$$

The likelihood function is the product of Poisson probabilities for all bins:

$$L(\mu, \theta) = \prod_{j=1}^{N} \frac{(\mu s_j + b_j)_j^n}{n_j!} e^{-(\mu s_j + b_j)} \prod_{k=1}^{M} \frac{u_k^{m_k}}{m_k!} e^{-u_k} \tag{6.14}$$

To test a hypothesized value of μ we consider the profile likelihood ratio

$$\lambda(\mu) = \frac{L(\mu, \hat{\hat{\theta}})}{L(\hat{\mu}, \hat{\theta})} \tag{6.15}$$

where $\hat{\hat{\theta}}$ in the numerator denotes the value of θ that maximizes L for the specified μ, i.e. it is the maximum likelihood (ML) estimator of θ (and thus is a function of μ). $\hat{\mu}$ is assumed to follow a Gaussian distribution with a mean of μ'.The denominator is the maximized (unconditional) likelihood function, i.e., $\hat{\mu}$ and $\hat{\theta}$ are their ML estimators. The presence of the nuisance parameters broadens the profile likelihood as a function of μ relative to what one would have if their values were fixed. This reflects the loss of information about μ due to the systematic uncertainties.
From the definition of $\lambda(\mu)$, one can see that $0 \leq \lambda \leq 1$, with λ near 1 implying good agreement between the data and the hypothesized value of μ. Equivalently it is useful to use the test statistic:

$$t_\mu = -2 \ln \lambda(\mu) \tag{6.16}$$

as the basis of a statistical test. Higher values of t_μ thus correspond to increasing incompatibility between the data and μ. This is the test statistic used in the Sterile Neutrino Analysis of my thesis.
Now, to avoid to simulate pseudo-experiments and hence to save computational time, we can introduce the Asimov data set, that is defined such as when one uses it to evaluate the estimators for all parameters, one obtains the true parameter values. In particular, if the Asimov data, $n_{i,A}$ and $m_{i,A}$, are defined such as they are equal to the expectation values of:

$$n_{i,A} = E[n_i] = \nu_i = \mu' s_i(\theta) + b_i(\theta), \tag{6.17}$$

$$m_{i,A} = E[m_i] = u_i(\theta) \tag{6.18}$$

which are the quantities used to define the likelihood in Eq. 6.14. Hence, these quantities are used instead of the same ones obtained from pseudo-experiments. This way, if we consider the likelihood function for the generic analysis given by Eq. 6.14, and to simplify the notation we define

$$\nu_i = \mu' s_i + b_i \tag{6.19}$$

Then, the ML estimators for the parameters can be found by setting the derivatives of $\ln L$ with respect to all of the parameters equal to zero [98]:

$$\frac{\partial \ln L}{\partial \theta_j} = \sum_{i=1}^{N} \left(\frac{n_i}{\nu_i} - 1 \right) \frac{\partial \nu_i}{\partial \theta_j} + \sum_{i=1}^{M} \left(\frac{m_i}{u_i} - 1 \right) \frac{\partial u_i}{\partial \theta_j} = 0 \tag{6.20}$$

and the Asimov data set the likelihood ratio becomes:

$$\lambda(\mu) = \frac{L(\mu, \hat{\hat{\theta}})}{L(\hat{\mu}, \hat{\theta})} = \frac{L_A(\mu, \hat{\hat{\theta}})}{L_A(\mu', \hat{\theta})} \tag{6.21}$$

With this in mind, we can explicitly define the test used for the ORCA sterile analysis as:

$$-2 \log L = \sum_{i=1}^{N_E} \sum_{j=1}^{N_{\cos\theta}} 2 \left[\left(N_{ij}^{model} - N_{ij}^{obs} \right) + N_{ij}^{obs} \log \left(\frac{\mathrm{N_{ij}^{model}}}{\mathrm{N_{ij}^{obs}}} \right) \right] + \sum_{k=1}^{N_{Syst}} \left(\frac{\eta_k^{test} - \eta_k^{nominal}}{\sigma_{\eta_k}} \right)^2 \tag{6.22}$$

where the parameters definition follows the same method as in Eq. 6.2, i.e. in the ANTARES analysis. The two formulas are almost identical, except for a constant shift in the likelihood definition.

6.2.8 Sensitivity to θ_{24} and θ_{34}

Fig. 6.13 (a) and (b) show the ORCA sensitivity to the mixing angles θ_{24} and θ_{34}, given $\Delta m^2_{41} > 0.1$ eV^2, for 3 years of data taking at 90% and 99% confidence level. At these values of sterile neutrino mass, fast oscillations driven by Δm^2_{41} are not resolved and the analysis becomes independent of its exact size. The sensitivity is compared to the upper limits obtained from other experiments. Dashed lines are the result of the analysis keeping the additional CP phase δ_{24} fixed at zero and assuming normal ordering. Continuous lines instead represent the analysis with δ_{24} free. Due to an approximate degeneracy between the sign of $\cos\delta_{24}$ and the mass ordering,

the most conservative contours between normal and inverted orderings for fixed δ_{24} is a good approximation of the result of letting this parameter float. In this way, our free δ_{24} results can be more directly compared with the IceCube analysis with inverted ordering (IO). Both figures show that ORCA is competitive in constraining the mixing elements $|U_{\mu 4}|$ and $|U_{\tau 4}|$, and is expected to improve the sensitivity to $|U_{\tau 4}|$ by almost a factor 2 with respect to current limits.

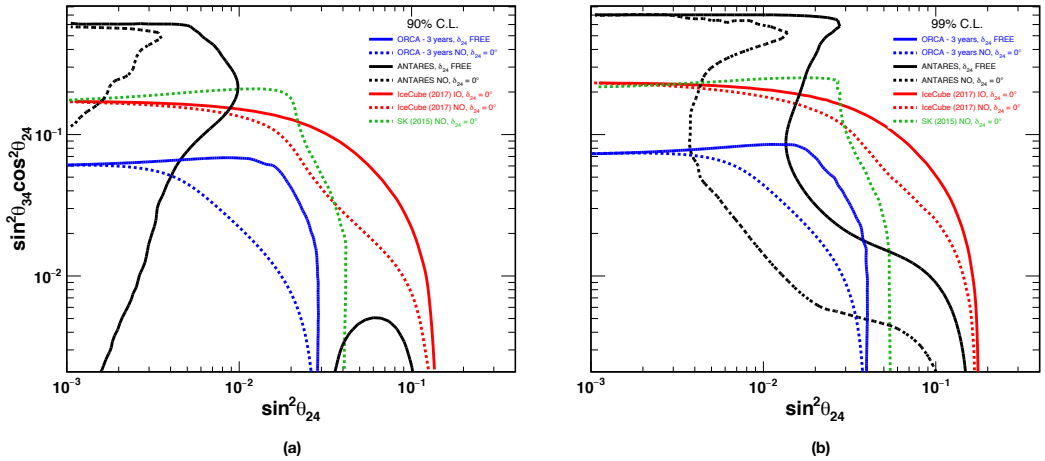

Figure 6.13: ORCA sensitivity for $\Delta m^2_{41} > 0.1$ eV^2, with 3 years of data taking, on the sterile mixing angles at 90% C.L. (a) and 99% C.L. (b) compared with the upper limits from other neutrino telescopes. Dashed lines correspond to analyses made by fixing δ_{24}. Continuous lines for ORCA and ANTARES correspond to an analysis with δ_{24} free. Since there is a degeneracy between δ_{24} and mass ordering, upper limits from IceCube including IO are also shown which can be compared with the continuous lines from ORCA and ANTARES.

6.3 Sterile Mass Dependent Analysis with ORCA and ANTARES

For higher values of Δm^2_{41} the oscillation frequency is too high to be resolved in the energy range up to 100 GeV. In this case we need a detector for higher energies such as KM3NeT/ARCA to probe oscillation effects driven by Δm^2_{41}. However, ANTARES and ORCA are sensitive to effects at lower sterile masses. At $\Delta m^2_{41} < 0.1$ eV^2, the current best limits on the $|U_{\mu 4}|$ sterile mixing element come from the MINOS/MINOS+ experiment [16]. For their

analysis a vacuum approximation is used since matter effects are expected to be negligible at a baseline of 735 km. With ANTARES and ORCA instead, longer baselines (up to the Earth diameter) are available to exploit matter effects. However, since the ANTARES energy threshold is ~ 20 GeV and, as shown in Fig. 2.9, the effects of lower sterile masses are more evident for energies below 20 GeV, we do not expect a competitive result from ANTARES.

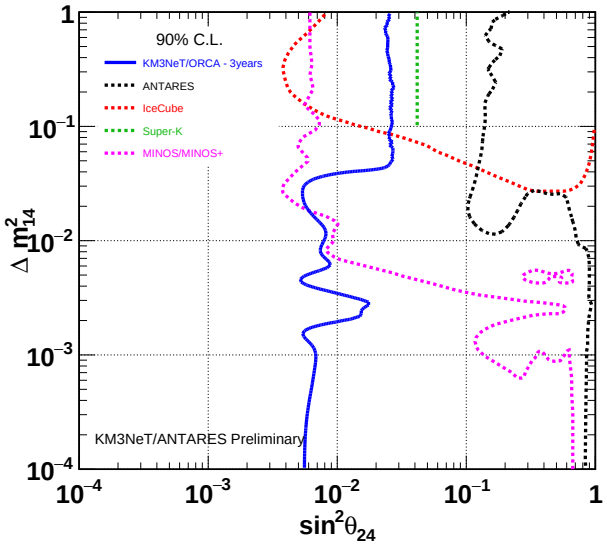

Figure 6.14: ORCA sensitivity (blue line) and ANTARES upper limits (dashed black line), at 90% C.L. on Δm^2_{14} and θ_{24}. The ORCA sensitivity is evaluated for 3 years of data taking. The ANTARES upper limits are evaluated with the same data sample of Ref. [**?**], i.e. for the period 2007-2016. Upper limits from other experiments are also reported for comparison.

The low Δm^2_{14} analysis for ANTARES is made with the same dataset used to constrain the sterile-active mixing angles and for ORCA, with the same parameters and systematics of the analysis of previously defined.
Fig. 6.14 shows the sensitivity of ORCA and the upper limits of ANTARES for θ_{24} and Δm^2_{14} compared with the upper limits from the other experiments. From the plot it is evident that ORCA sensitivity is very leading to constrain low sterile masses and it improves the current MINOS/MINOS+ limits of about 2 orders of magnitude for $\Delta m^2_{41} < 10^{-3}$ eV^2. As already stated and expected from Fig. 6.8 and Fig. 6.9, ORCA sensitivity appears to be better for low Δm^2_{14} values. This is a result of multiple and longer baselines combined with matter effects that can break degeneracies with the atmospheric mass splitting. The ANTARES upper limits, instead, are not

competitive with the other experiments, as expected already from Fig. 2.9. Fig. 6.15 shows the ORCA sensitivity for θ_{14} and Δm^2_{14} compared with the upper limits from Daya Bay [100] and the DUNE [101] sensitivity. The Daya Bay upper limits come from an analysis of $\sim$ 520 days. My analysis shows that ORCA can still be competitive even to constrain θ_{14}. However, it performs better with θ_{24}.

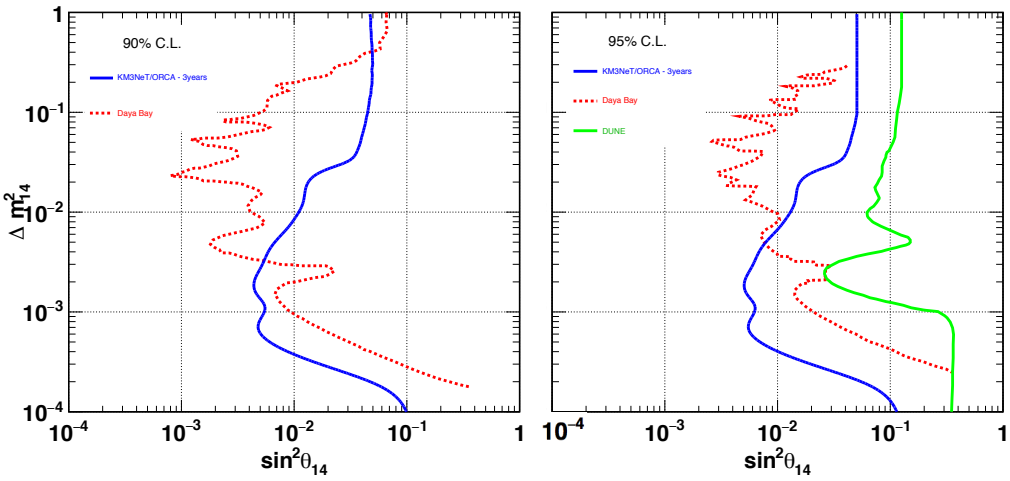

Figure 6.15: ORCA sensitivity (blue line) at 90% C.L. (a) and 95% C.L. on Δm^2_{14} and θ_{14}. The ORCA sensitivity is evaluated for 3 years of data taking. Upper limits from Daya Bay [100] and sensitivity from DUNE [101] are also reported for comparison.

6.4 Conclusions

In this chapter I described the sterile neutrino analyses made with two neutrino telescopes: ANTARES, operating since 2007, and KM3NeT/ORCA, under construction in the Mediterranean Sea. The analyses show how good neutrino telescopes perform in this kind of research, in particular, ANTARES has been able to reject part of the sterile parameter space not yet probed by other experiments. ORCA shows a very high potential in constraining sterile neutrino parameters, it appears to be leading both for constraining the sterile-active mixing angles and expecially for low sterile masses, for which it improves of about 2 orders of magnitude the best upper limits we have to date, which come from MINOS/MINOS+ [16]. A paper on the ANTARES sterile analysis has already been published (JHEP06(2019)113) and another one on the ORCA analysis is being prepared.

Summary

In a scenario in which the standard three-flavor framework of neutrino oscillations is well established, a number of oscillation experiments present anomalies that can be explained if we consider the existence of a fourth, massive and light neutrino. If it exists, it can not participate to weak interactions. This is why it is called **sterile neutrino**, it can only have gravitational interactions due to its non-zero mass.
However, the data collected to date present an incomplete, perhaps even contradictory picture, where 2-3 σ agreement in favor of and in contradiction to the existence of sterile neutrinos is present. Therefore, there is the need to clarify this scenario.
In this context, the work of my thesis is focused on the search of sterile neutrinos with deep water neutrino telescopes, using both the real data from ANTARES and the expected performances of the larger KM3NeT/ORCA detector. For this purpose I analysed $\sim$ 10 years of ANTARES data (from 2007 to 2016) showing its capability of constraining the sterile-active mixing angles. In particular, no sterile neutrino has been observed with ANTARES and regions of the parameter space not yet reached by other experiments have been excluded by the ANTARES analysis.
To perform the ORCA sterile neutrino analysis I used Monte Carlo data and the results obtained show that ORCA will be a leading experiment in the aterile neutrino searches. In particular, ORCA is expected to improve the sensitivity to the neutrino mixing parameter $|U_{\tau 4}|^2$ by almost a factor 2 with respect to current limits. At the same time it is able to constrain the sterile mixing angles for low sterile masses ($\Delta m^2_{14} < 0.1$ eV^2) and to improve the current best world upper limits on $|U_{\mu 4}|^2$ up to two orders of magnitude.
The main goal of ORCA is to measure the neutrino mass ordering, which is one of the remaining outstanding questions in neutrino physics. Monte Carlo simulations have shown that for this analysis the shower-like events channel is the leading one. This requires to have a good event classification. To this purpose, we need a good shower reconstruction. Hence, in parallel to the sterile neutrino analysis I have developed a shower reconstruction al-

gorithm with a method that have not been tried before. My reconstruction shows similar results to the standard shower reconstruction previously used in ORCA. It has started to be used by the collaboration and works on improving its performances are ongoing.
Finally, to be able to better understand how ORCA works, I have been involved in real data analysis. In particular I developed an online analysis tool to monitor the data coming from KM3NeT (ORCA and ARCA) which is already running with the first detection units.

Bibliography

[1] *Physics Reports (Physics Letters C) 427 257* (2006)

[2] *Particle Data Group.*

[3] J. Lesgourgues, S. Pastor, *Massive neutrinos and cosmology.* arXiv:astro-ph/0603494v2

[4] A.D. Dolgov, *Neutrinos and Big Bang Nucleosynthesis* Nuovo Cim.B117:1081-1088,2003

[5] S. Gariazzo, *Light Sterile Neutrinos in Cosmology.* arXiv:1601.01475v1

[6] J. Hamann et al., *Sterile neutrinos with eV masses in cosmology*, Journal of Physics: Conference Series 375 (2012) 032003

[7] M. Pettini, *Introduction to Cosmology.*

[8] S. H. Suyu et al., *H0LiCOW I. H0 Lenses in COSMOGRAIL's Wellspring: Program Overview.* arXiv:1607.00017v2

[9] A. G. Riess et al., *Large Magellanic Cloud Cepheid Standards Provide a 1% Foundation for the Determination of the Hubble Constant and Stronger Evidence for Physics Beyond ΛCDM.* arXiv:1903.07603v2

[10] A. Aguilar at al., *Phys. Rev. D64:112007* (2001)

[11] Aguilar-Arevalo AA, et al., *Phys. Rev. Lett. 98:231801* (2007)

[12] The KARMEN Collaboration, *Nucl.Instrum.Meth. A289, 490 (1990).*

[13] E. Church, K. Eitel, G. B. Mills, and M. Steidl, *Phys.Rev. D66, 013001 (2002)*, arXiv:hep- ex/0203023 [hep-ex].

[14] The Ice Cube Collaboration, *Searches for Sterile Neutrinos with the IceCube Detector*, Phys. Rev. Lett. 117, 071801 (2016)

[15] The Ice Cube Collaboration, *Search for sterile neutrino mixing using three years of IceCube DeepCore data*. Phys. Rev. D 95 (2017) 112002

[16] The MINOS Collaboration, *Search for sterile neutrinos in MINOS and MINOS+ using a two-detector fit. Phys. Rev. Lett. 122, 091803* (2019)

[17] Gollapinni S., arXiv:1510.04412 (2015)

[18] The MiniBooNE Collaboration, *Phys.Rev.Lett. 103, 061802 (2009)*, arXiv:0903.2465 [hep-ex].

[19] C. Giunti, M. Laveder *Statistical Significance of the Gallium Anomaly*, Phys.Rev.C83:065504,2011

[20] Kaether F, et al., *Phys. Lett. B685:47* (2010)

[21] Abdurashitov JN, et al., *Phys. Rev. C73:045805* (2006)

[22] Mueller et al, arXiv:1101.2663

[23] Mueller et al., *Phys. Rev. C83:054615 (2011).*

[24] Ko Y, et al., *Phys.Rev.Lett. 118:121802* (2017)

[25] Alekseev I, et al., *Phys.Lett. B787:56* (2018)

[26] M. Archidiacono et al. *JCAP 1608, 067* (2016)

[27] Carlo Giunti and Thierry Lasserre., *eV-scale Sterile Neutrinos.* arXiv:1901.08330

[28] M. Dentler et al, *Updated global analysis of neutrino oscillations in the presence of eV-scale sterile neutrinos*, DOI: 10.1007/JHEP08(2018)010

[29] Carlo Giunti and Chung W. Kim., *Fundamentals of Neutrino Physics and Astrophysics.* OXFORD University Press

[30] Fukuda Y, et al., *Phys. Rev. Lett. 81:1562* (1998)

[31] Jonathan M. Link et al., *Light Sterile Neutrinos: A White Paper.* arXiv:1204.5379v1

[32] S. L. Glashow, Nucl Phys 22 (1961) 579

[33] S. Weinberg, Phys Rev Lett 19 (1967) 1264

[34] A. Salam, Proc 8-th Nobel Symp, ed N Svartholm (Almqmst and Wlksell, Stockholm, 1968) p. 367

[35] A. Strumia, F. Vissani, *Neutrino masses and mixings and...* arXiv:hep-ph/0606054v3

[36] B. Pontecorvo, *Neutrino Experiments and the Problem of Conservation of Leptonic Charge*. Sov. Phys. JETP 26 (1968). [Zh. Eksp. Teor. Fiz.53,1717(1967)], p. 984–988.

[37] L. Wolfenstein, *Neutrino Oscillations in Matter*. Phys. Rev. D17 (1978), pp. 2369–2374. doi: 10.1103/PhysRevD.17.2369

[38] S. P. Mikheev and A. Yu. Smirnov, *Resonance Amplification of Oscillations in Matter and Spectroscopy of Solar Neutrinos*. Sov. J. Nucl. Phys. 42 (1985). [Yad. Fiz.42,1441(1985)], pp. 913–917.

[39] J. Linder, *Neutrino matter potentials induced by Earth* arXiv:hep-ph/0504264v4

[40] J.A.B. Coelho, *OscProb neutrino oscillation calculator*. https://github.com/joaoabcoelho/OscProb.

[41] A. M. Dziewonski and D. L. Anderson, *Preliminary reference Earth model*. Physics of the Earth and Planetary Interiors, 25(4):297-356, 1981.

[42] M.A. Markov et al, *On high-energy neutrino physics*. University of Rochester. p. 578. (1960)

[43] F. Halzen et al,

[44] . DOI:10.1063/1.2930733

[45] I. A. Belolaptikov, *Results from the Baikal Underwater Telescope*. Nuclear Physics B: Proceedings Supplements. 43 (1–3): 241–244. (1995)

[46] The Baikal-GVD Collaboration, https://baikalgvd.jinr.ru

[47] M. Spurio, *Particles and Astrophysics: A Multi-Messenger Approach*. Springer

[48] Miller, T., Barwick, S. W., Bouchta, A., Carius, S., Coulthard, A., Engel, K., *AMANDA: Measurement of South Pole Ice Transparency at 800 meter Depth*, 23rd International Cosmic Ray Conference, Vol. 4, held 19-30 July, 1993

[49] T.K. Gaisser, *Atmospheric Neutrino Flux: A Review of Calculations*

[50] G.D. Barr, S. Robbins, *Uncertainties in Atmospheric Neutrino Fluxes*

[51] J. Evans, D. G. Gamez, S. D. Porzio, S. Soldner-Rembold, S. Wren, *Uncertainties in Atmospheric Muon-Neutrino Fluxes Arising from Cosmic-Ray Primaries*. Phys. Rev. D 95, 023012 (2017)

[52] A. G. Rosso et al., *Introduction to neutrino astronomy*

[53] Paolo Lipari, Maurizio Lusignoli, Francesca Sartogo, *The Neutrino cross-section and upward going muons*. Phys.Rev.Lett. 74 (1995) 4384-4387 10.1103/PhysRevLett.74.4384 hep-ph/9411341

[54] Joseph A. Formaggio, *From eV to EeV: Neutrino Cross-Sections Across Energy Scales*, arXiv:1305.7513v1

[55] Kevin McFarland, *Neutrino Interactions*, arXiv:0804.3899v1

[56] J.V. Jelley, *Cerenkov Radiation and Its Applications*. Br. J. Appl. Phys. 6, 277, (1955).

[57] S. O Flyckt, C. Marmonier, *PHOTOMULTIPLIER TUBES principles and applications*

[58] The ANTARES Collaboration, *ANTARES: the first undersea neutrino telescope*. Nucl. Instrum. Meth. A 656 (2011) 11.

[59] The KM3NeT Collaboration, *Letter of Intent for KM3NeT 2.0*. Journal of Physics G: Nuclear and Particle Physics, 43 (8), 084001, 2016.

[60] The KM3NeT Collaboration, *Characterisation of the Hamamatsu photomultipliers for the KM3NeT Neutrino Telescope*. 2018, JINST 13 P05035

[61] The ANTARES Collaboration, *The ANTARES detector: background sources and effects on detector performance*.

[62] The ANTARES Collaboration, *Long-term monitoring of the ANTARES optical module efficiencies using ^{40}K decays in sea water*. Eur. Phys. J. C (2018) 78: 669

[63] T. Chiarusi, E. Giorgio for the KM3NeT Collaboration, *The Software Defined Networking in KM3NeT*, EPJ Web of Conferences 207, 06009 (2019), DOI: https://doi.org/10.1051/epjconf/201920706009

[64] C. Bozza for the KM3NeT Collaboration, *KM3NeT Acquisition Control*, EPJ Web of Conferences 207, 06008 (2019), DOI: https://doi.org/10.1051/epjconf/201920706008

[65] R. Bruijn for the KM3NeT Collaboration, *KM3NeT Readout and Triggering*, EPJ Web of Conferences 207, 06007 (2019), DOI: https://doi.org/10.1051/epjconf/201920706007

[66] T. Gal for the KM3NeT Collaboration, *Live monitoring and quasi-online event reconstruction for KM3NeT*, EPJ Web of Conferences 116, 05003 (2016), DOI: https://doi.org/10.1051/epjconf/201611605003

[67] Ronald Bruijn, Tommaso Chiarusi for the KM3NeT Collaboration, *KM3NeT Data Acquisition and and Trigger System*, PoS(ICRC2019)1177

[68] J. Hofestädt, *Measuring the neutrino mass hierarchy with the future KM3NeT/ORCA detector*. PhD Thesis.

[69] C. Kopper, *A software framework for KM3NeT*. Nucl. Instrum. Meth. A602, 107 (2009).

[70] M. De Jong, *Multi-dimensional interpolations in C++*, arXiv:1907.02597 (2019)

[71] C. Kopper, *Performance Studies for the KM3NeT Neutrino Telescope*. PhD Thesis.

[72] Press et al., *Numerical Recipes in C*.

[73] R. Wigmans, *Calorimetry*. Scientifica Acta 2, No. 1, 18 – 55 (2008).

[74] The KM3NeT Collaboration, *Intrinsic limits on resolutions in muon- and electron-neutrino charged-current events in the KM3NeT/ORCA detector*. arXiv:1612.05621v2

[75] The ANTARES collaboration, *The Run-by-Run Monte Carlo simulation for the ANTARES experiment*. EPJ Web Conf. 116 (2016) 02002.

[76] D. Bailey, *Monte Carlo tools and analysis methods for understanding the ANTARES experiment and predicting its sensitivity to dark matter*. PhD Thesis.

[77] M. Honda et al., *Atmospheric neutrino flux calculation using the NRLMSISE-00 atmospheric model*. Phys. Rev., D92(2):023004, 2015.

[78] The Application Software Group collaboration, *GEANT 3: a detector description and simulation tool*. CERN Program Library Long Writeup W5013 (1995).

[79] The ANTARES collaboration, *A fast algorithm for muon track reconstruction and its application to the ANTARES neutrino telescope*. Astropart. Phys. 34 (2011) 652.

[80] E. Visser, *Neutrinos from the Milky Way*. PhD Thesis.

[81] G. Cowan, *Statistical Data Analysis*.

[82] C. Andreopoulos et All., *The GENIE Neutrino Monte Carlo Generator*. Published in Nucl.Instrum.Meth.A614 (2010) 87-104.

[83] C. Distefano for the ANTARES and KM3NeT Collaborations, *gSeaGen: a GENIE-based code for neutrino telescopes* arXiv:1602.00501v1.

[84] A. G. Tsirigotis, G. Bourlis, A. Leisos, S. E. Tzamarias, *Hellenic Open University Reconstruction and Simulation (HOURS) software package: User Guide and short reference of Event Generation, Cherenkov photon production and Optical Module simulation.* arXiv:1702.00945v1.

[85] Y. Becherini et al., *A parameterisation of single and multiple muons in the deep water or ice.* Astropart. Phys. 25, 1 (2006).

[86] The Ice Cube Collaboration, *Measurement of atmospheric neutrino oscillations at 6–56 GeV with IceCube DeepCore*. Phys. Rev. Lett. 120 (2018) 071801 [arXiv:1707.07081].

[87] S.K. Agarwalla, S.S. Chatterjee and A. Palazzo, *Signatures of a light sterile neutrino in T2HK*. JHEP 04 (2018) 091 [arXiv:1801.04855].

[88] F. Capozzi, E. Lisi, A. Marrone, D. Montanino and A. Palazzo, *Neutrino masses and mixings: status of known and unknown 3ν parameters*. Nucl. Phys. B 908 (2016) 218 [arXiv:1601.07777].

[89] The ANTARES Collaboration, *The ANTARES optical module*. Nucl. Instrum. Meth. A 484 (2002) 369 [astro-ph/0112172]

[90] The ANTARES Collaboration, *Transmission of light in deep sea water at the site of the ANTARES neutrino telescope*. Astropart. Phys. 23 (2005) 131 [astro-ph/0412126].

[91] P.F. de Salas, D.V. Forero, C.A. Ternes, M. Tortola and J.W.F., *Status of neutrino oscillations 2018: 3σ hint for normal mass ordering and improved CP sensitivity.* Phys. Lett. B 782 (2018) 633 [arXiv:1708.01186].

[92] The ANTARES Collaboration, *Measurement of atmospheric neutrino oscillations with the ANTARES neutrino telescope.* Phys. Lett. B 714 (2012) 224 [arXiv:1206.0645].

[93] The Super-Kamiokande collaboration, *Limits on sterile neutrino mixing using atmospheric neutrinos in Super-Kamiokande.* Phys. Rev. D 91 (2015) 052019 [arXiv:1410.2008].

[94] I. Esteban, M. C. Gonzalez-Garcia, M. Maltoni, I. Martinez-Soler, T. Schwetz, *Updated fit to three neutrino mixing: exploring the accelerator-reactor complementarity.* JHEP 01 (2017) 087.

[95] S. Bourret *Neutrino oscillations and Earth tomography with KM3NeT-ORCA*. PhD Thesis.

[96] S. Bourret, *Monte Carlo sparseness and sensitivity overestimation.*

[97] L. Quinn *Determining the Neutrino Mass Hierarchy with KM3NeT/ORCA*. PhD Thesis.

[98] G. Cowant et al, *Asymptotic formulae for likelihood-based tests of new physics.* arXiv:1007.1727v3

[99] The ANTARES Collaboration, *Measuring the atmospheric,neutrino oscillation parameters and constraining the 3+1 neutrino,model with ten years of ANTARES data.* J. High Energ. Phys. (2019) 2019: 113.

[100] The Daya Bay Collaboration, *Improved Search for a Light Sterile Neutrino with the Full Configuration of the Daya Bay Experiment.* Phys. Rev. Lett. 117, 151802.

[101] Jeffrey M. Berryman, Andre de Gouvea, Kevin J. Kelly, Andrew Kobach, *A Sterile Neutrino at DUNE*, Phys. Rev. D 92, 073012 (2015)